Random-matrix theory and stroboscopic models of topological insulators and superconductors

Proefschrift

ter verkrijging van
de graad van Doctor aan de Universiteit Leiden,
op gezag van de Rector Magnificus
prof. mr P. F. van der Heijden,
volgens besluit van het College voor Promoties
te verdedigen op woensdag 21 november 2012
klokke 10.00 uur

door

Jan Patrick Dahlhaus

geboren te Essen, Duitsland in 1982

Promotiecommissie

Promotor:	Prof. dr. C. W. J. Beenakker
Overige leden:	Prof. dr. E. R. Eliel
	Prof. dr. ir. L. P. Kouwenhoven (Technische Universiteit Delft)
	Prof. dr. H. Schomerus (Lancaster University)
	Prof. dr. J. Zaanen

Casimir PhD Series, Delft-Leiden, 2012-29
ISBN 978-90-8593-137-9

Dit werk maakt deel uit van het onderzoekprogramma van de Stichting voor Fundamenteel Onderzoek der Materie (FOM), die deel uit maakt van de Nederlandse Organisatie voor Wetenschappelijk Onderzoek (NWO).

This work is part of the research programme of the Foundation for Fundamental Research on Matter (FOM), which is part of the Netherlands Organisation for Scientific Research (NWO).

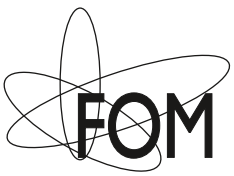

Cover: *Topological invariant of a nodal Rashba superconductor in contact with a metal, as a function of interface orientation and momentum. Compare with the left panel of Fig. 5.4.*

To Nina and my parents.

Contents

Chapter 1

Introduction

1.1 Preface

Considering what we know about Nature, it is quite fascinating how well it can be described by complex mathematical concepts. Among the most impressive examples might well be General Relativity and Quantum Mechanics. In the former the ideas of differential geometry form the heart of what we call curved space-time, while in the latter the world is described by states and operators in a Hilbert space.

Another intriguing area of mathematics - topology - is by now understood to govern the nature of gapped electronic systems like band insulators or superconductors [1–5]. And it has profound impact on their properties. Most importantly, the boundary between electronic systems with different topology supports protected surface states – robust against disorder and other imperfections. From Majorana bound states at the ends of superconducting wires to the unique metallic surface of three dimensional topological insulators a variety of different boundary states arise in this way – depending on the dimensionality and the symmetries of the system.

The consequences of band topology have by now been observed in several systems, foremost in the form of the quantum Hall and quantum spin Hall effects in two dimensions and the topological insulator in three dimensions. Furthermore, the first signatures of topological superconductivity have been found in nanowire setups.

The primary methods of identification of these phases are their unique transport properties: in the quantum Hall effect, perfectly transmitting

edge channels lead to a quantized Hall conductance, the quantum spin Hall effect shows quantized two- and four-terminal conductances and Majorana bound states show up as a zero bias peak in the Andreev conductance. Only three-dimensional topological insulators are, up to now, identified by spectroscopy rather than by electronic transport, because of the complication of a non-zero bulk conductance.

This work is dedicated to the interplay of topology and imperfections in insulators and superconductors. On the one hand a realistic understanding of the transport signatures of topological phases in the presence of disorder is vital to explain experimental data. On the other hand the interplay of topology and imperfections leads to interesting new phenomena such as delocalization at topological phase transitions and geodesic scattering. We study the thermal and Andreev conductances of chaotic superconducting quantum dots, the effect of disorder on the electrical conductance of normal-superconductor junctions, and the influence of surface roughness on the conductance of a topological insulator. Furthermore we investigate the localization properties at a topological phase transition, estimating the universal critical exponent that describes the observed delocalization for both the quantum Hall and the quantum spin Hall effect.

1.2 Concept of topology in insulating systems

What is a topological phase? I will try to give an intuitive approach to the topic, using examples and concentrating on topics that will be of interest later on in this thesis. From the band theory of solids we know that the electronic excitations of condensed matter systems appear in the form of energy bands $E(\boldsymbol{k})$ with corresponding Bloch states $\psi(\boldsymbol{k})$, $\boldsymbol{k}$ being a wave vector in the first Brillouin zone. In an insulating system, the Fermi energy lies in an excitation gap between such bands. Now, a topological property is by definition something that is preserved under continuous deformations, in this case of the Hamiltonian. A simple example is most suitable to illustrate how this concept applies to band structures.

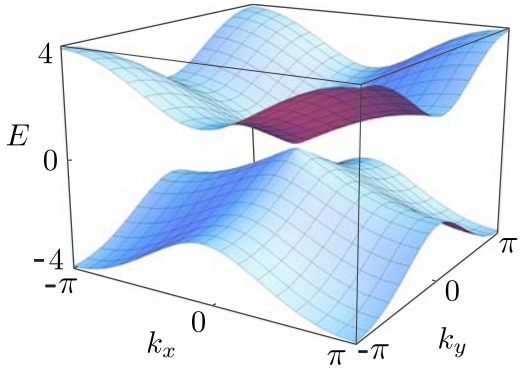

Figure 1.1. Band structure for $\mu = 1.9$. At the center of the Brillouin zone a Dirac cone emerges, which will be fully formed when the gap closes at $\mu = 2$.

1.2.1 Example: winding number

Consider the Hamiltonian

$$H(\boldsymbol{k}) = \boldsymbol{u}(\boldsymbol{k}) \cdot \boldsymbol{\sigma} = \begin{pmatrix} \sin k_x \\ \sin k_y \\ \cos k_x + \cos k_y - \mu \end{pmatrix} \cdot \begin{pmatrix} \sigma_x \\ \sigma_y \\ \sigma_z \end{pmatrix}, \tag{1.1}$$

with the Pauli matrices σ_i and momenta $k_x, k_y \in [-\pi, \pi)$ in the first Brillouin zone of a two-dimensional system. The two bands of the model, $E_\pm(\boldsymbol{k}) = \pm|\boldsymbol{u}(\boldsymbol{k})|$, are plotted in Fig. 1.1 for $\mu = 1.9$.

In this example, the notion of topology manifests itself in the spin structure of the wave functions. The spin quantization axis for given $\boldsymbol{k}$ is $\hat{\boldsymbol{u}}(\boldsymbol{k}) = \boldsymbol{u}(\boldsymbol{k})/|\boldsymbol{u}(\boldsymbol{k})|$. In Fig. 1.2 this vector is plotted in the Brillouin zone for two different values of μ. For $\mu = 1$, the vector shows a winding while for $\mu = 3$ it does not. With "winding" we mean the number of complete rotations the vector performs throughout the Brillouin zone. Due to the periodicity of the Brillouin zone it is an integer quantity and can be calculated by

$$\mathcal{I} = -\frac{1}{4\pi} \int_{-\pi}^{\pi} dk_x \int_{-\pi}^{\pi} dk_y \left[\frac{\partial \hat{\boldsymbol{u}}(\boldsymbol{k})}{\partial k_x} \times \frac{\partial \hat{\boldsymbol{u}}(\boldsymbol{k})}{\partial k_y} \right] \cdot \hat{\boldsymbol{u}}(\boldsymbol{k}). \tag{1.2}$$

A winding of a vector of this form is preserved under continuous deformations of the Hamiltonian $H(\boldsymbol{k})$ and is thus a topological property. Since the integer number $\mathcal{I}$ characterizes the topology, it is called topological invariant or in this specific case Skyrmion number. The integrand

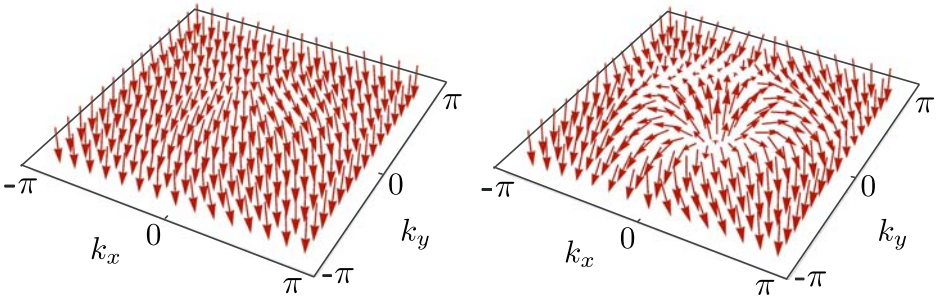

Figure 1.2. Spin quantization axis in the Brillouin zone for a topologically trivial phase, $\mu = 3$ (left panel), and a phase that shows a non-trivial winding, $\mu = 1$ (right panel). The winding can best be seen along the line $k_x = 0$, where the vector makes a complete rotation as it goes from $-\pi$ to π.

of Eq. (1.2) is the so-called Berry flux and the overall integral relates to the Berry phase picked up by a state $\psi(\boldsymbol{k})$ of the lower band when $\boldsymbol{k}$ is transported through the Brillouin zone in a closed loop. In this simple example the topological invariant represents the phase picked up when a spin is rotated once around.

The topological invariant cannot change when we change the Hamiltonian continuously as long as $\boldsymbol{u}(\boldsymbol{k}) \neq (0,0,0)$ for all $\boldsymbol{k}$. Thus the gap between the two bands has to vanish when the topology changes, which happens e.g. for $\mu = 2$ at $(k_x, k_y) = (0,0)$. In overall the model supports the following phases, depending on the value of μ:

$$\mathcal{I}(\mu) = \begin{cases} -\text{sign}\,(\mu) & \text{if } |\mu| < 2, \\ 0 & \text{if } |\mu| > 2. \end{cases} \tag{1.3}$$

The closing of the energy gap is a general feature appearing generically at the transition between two different topological phases.

1.2.2 Boundary states

Maybe the most striking consequence of band topology appears at the boundary of a topological phase. Imagine an interface between a topological region (e.g. $\mathcal{I} = 1$) and a trivial region ($\mathcal{I} = 0$). Interpolation of the Hamiltonian between the two regions requires a change of topology which is accompanied by a closing of the energy gap. Therefore there have to be low-energy electronic states in the region where the energy

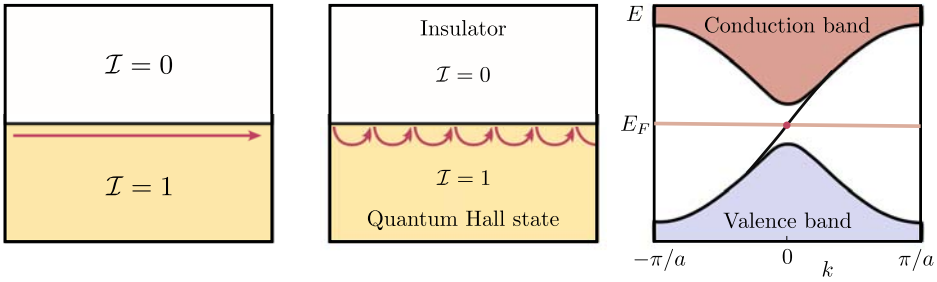

Figure 1.3. Left panel: Topologically protected state propagating along the edge of a region with non-trivial winding number. Middle panel: in the conventional quantum Hall effect, edge states arise in the presence of a strong magnetic field due to the motion electrons perform as their cyclotron orbits bounce repeatedly off the edge of the sample. Right panel: Energy spectrum showing the two bulk bands and the dispersion of the edge state.

gap passes through zero. In other words we find boundary states with energies in the bulk gap.

For the toy model above, these boundary states propagate in one direction along the edge of a sample, see Fig. 1.3. Since there are no states into which they could backscatter, they are insensitive to disorder. A change of sign of the topological invariant reverses the direction of propagation.

The edge states are a feature that our model has in common with the quantum Hall effect, rooted in exactly the same concept of topology. For the quantum Hall effect, there is an intuitive understanding for the existence of edge states: they arise due to the motion electrons perform in a strong magnetic field as their cyclotron orbits bounce repeatedly off the edge of the sample. The presence of the perfectly transmitting edge states leads to a quantized Hall conductance: $G_H = \mathcal{I} G_0$ with the conductance quantum $G_0 = e^2/h$. Unlike the conventional quantum Hall effect the model above (taken from Ref. [6]) does not originate in Landau level quantization – it is called quantum anomalous Hall effect.

1.2.3 Role of symmetries and dimensionality

The example studied so far is in the quantum Hall universality class, which means that it lacks time-reversal symmetry. Indeed symmetries play a crucial role for the existence and the nature of topology in a system [7]. For example the presence of time-reversal symmetry in a

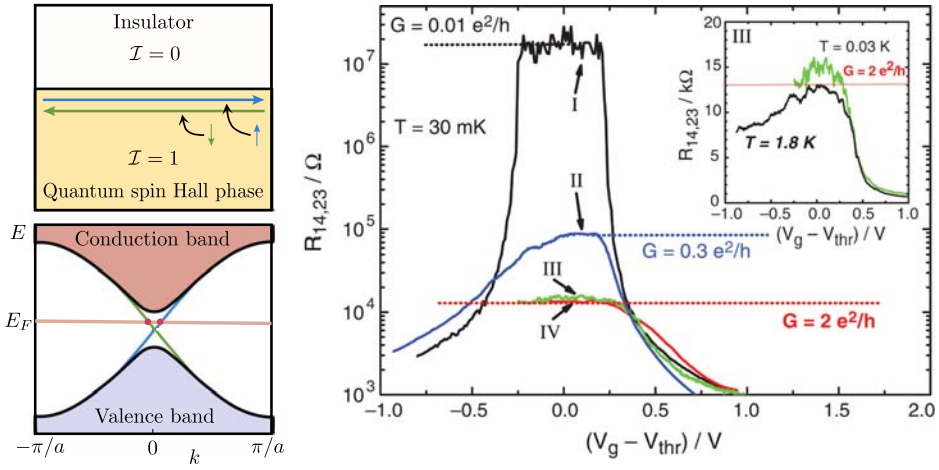

Figure 1.4. Edge states and transport measurements of the quantum spin Hall effect. Upper panel: counter-propagating pair of topologically protected states with opposite spin at the edge of a quantum spin Hall phase. Left lower panel: Energy spectrum showing the two bulk bands and the dispersion of the edge states. Right panel: Experimental data for the conductance of a quantum spin Hall sample, as a function of the gate voltage that tunes the Fermi energy E_F through the bulk gap. Sample I is in the trivial state, showing insulating behavior, while samples III and IV show quantized transport associated with edge states. From Ref. [8]. Reprinted with permission from AAAS.

spinfull system,

$$H(\boldsymbol{k}) = \sigma_y H^*(-\boldsymbol{k})\sigma_y, \tag{1.4}$$

forbids any winding of the type described above in an isolated band. Thus it was long thought that the existence of topology becomes impossible in the presence of time-reversal symmetry. When starting from 2005, theoretical proposals for topology in time-reversal invariant systems were put forward, the research area saw a rapid boost of activity [1–3]. This culminated in the experimental demonstration [8] of the so-called quantum spin Hall effect in 2007, demonstrating that the concept of topology is much more general than and not restricted to the winding numbers introduced above.

The quantum spin Hall effect is a time-reversal invariant version of the quantum Hall effect. Time-reversal symmetry ensures that an edge state always comes hand in hand with its time-reversed partner, a state

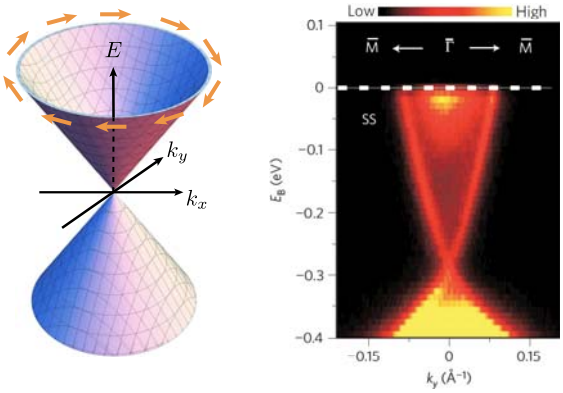

Figure 1.5. Topologically protected states on the surface of a three-dimensional topological insulator. Left panel: Dispersion relation of the metallic surface (Dirac cone). The spin direction is tied perpendicular to the momentum (orange arrows). Right panel: Energy spectrum of the surface states of the topological insulator Bi_2Se_3, measured by angle-resolved photo-emission spectroscopy. From Ref. [10]. Reprinted by permission from Macmillan Publishers Ltd.

with opposite spin, traveling in the reverse direction along the edge (see upper panel of Fig. 1.4).

A fundamental difference between the quantum Hall and the quantum spin Hall effect is that the topological invariant is restricted to the values 0 and 1 in the latter case, meaning either a pair of topologically protected edge states or none at all. The emphasize is here on the topological protection - further edge states may exist but would not be stable. In contrast the quantum Hall effect can realize any integer number of topologically protected edge modes, but they all propagate in the same direction. This ensures the topological protection: if there was a channel in the opposite direction, left and right moving states could scatter into each other and would hybridize, leading to a gap in the spectrum of edge states. In the quantum spin Hall effect this is prevented for a single pair of time reversed modes since the so-called Kramers degeneracy of the crossing point in the Brillouin zone (see lower panel of Fig. 1.4) is protected by time-reversal symmetry.

The two cases mentioned so far are intrinsically two-dimensional. When in 2008 topology was first observed in three dimensions [9], it was a huge step forward on the path to unravel all the possibilities that topology provides. Although conceptually the topology of the three-

dimensional topological insulator is a natural generalization of the quantum spin Hall effect, its properties are exceptional: instead of a pair of edge states, a three-dimensional topological insulator hosts a continuum of surface states, forming a metallic surface of in insulating bulk. Its dispersion has the form of a Dirac cone, see Fig. 1.5, with the spin perpendicular to momentum.

Generally the existence of topology and the allowed values of the topological invariant are determined by the dimensionality of a system and the symmetries present. For insulators, time reversal symmetry plays the primary role in the classification. For superconducting systems which are discussed in the next section, another type of fundamental symmetry arises (particle-hole symmetry) and provides an even larger variety of topological phases.

1.2.4 Anderson localization and topology

The free (ballistic) motion of a particle produces a quadratic spreading of a wave packet in time, $\langle\psi(t)|\hat{x}^2|\psi(t)\rangle \propto t^2$. A disordered potential slows down the spreading, to a linear increase $\langle\psi(t)|\hat{x}^2|\psi(t)\rangle = Dt$. This diffusive spreading, with diffusion constant D, describes a metal. If the disorder is strong enough, the metal becomes an insulator and the spreading stops at a characteristic length ξ,

$$\lim_{t\to\infty}\langle\psi(t)|\hat{x}^2|\psi(t)\rangle \sim \xi^2. \tag{1.5}$$

This so-called Anderson localization [11, 12] originates from destructive interference processes of the wave function and is thus a purely quantum mechanical phenomenon.

Anderson localization happens on shorter length scales in lower dimensional systems. In particular, the localization length grows linearly with the mean free path in one dimension, while it grows exponentially in two dimensions. In three dimensions the localization length is infinite below a critical disorder strength. At the critical disorder strength U_c a quantum phase transition occurs between a localized insulating phase and a diffusive metallic phase. The divergence of the localization length when the disorder strength U approaches U_c is governed by a critical exponent ν,

$$\xi \propto |U - U_c|^{-\nu}. \tag{1.6}$$

The critical exponent is a universal quantity depending only on the fundamental symmetries and the dimensionality, but not on microscopic details.

Anderson localization refers to states in the bulk of a disordered material. States may still be extended along the boundary, without any localization. These extended boundary states are a signature of a topologically nontrivial phase. Figs. 1.3 and 1.4 show examples in the quantum Hall effect and quantum spin Hall effect. The extended boundary states in these two cases carry electrical current along the edge of the system, with a quantized conductance. In a three-dimensional topological insulator, the surface supports extended states, but there is no quantization of conductance in that case.

The appearance and disappearance of extended boundary states is a topological phase transition. Because it is accompanied by a divergence of the localization length in the bulk of the system, it is also associated with a critical exponent, as in Eq. (1.6).

1.3 Topological superconductors

Just like insulators, superconductors have a gapped band structure. In this sense they are insulating as well - but for thermal instead of charge transport. Thus the concept of topology introduced above for insulating systems holds in the same way for superconductors. The presence of another fundamental symmetry (particle-hole symmetry) in a superconductor introduces new features though, as we discuss now.

On mean-field level, superconductors can be described by the Bogoliubov de Gennes Hamiltonian

$$H_{\mathrm{BdG}}(\boldsymbol{k}) = \begin{pmatrix} H_0(\boldsymbol{k}) - E_F & \Delta(\boldsymbol{k}) \\ -\Delta^*(-\boldsymbol{k}) & E_F - H_0^*(-\boldsymbol{k}) \end{pmatrix}, \tag{1.7}$$

with the single particle Hamiltonian $H_0(\boldsymbol{k})$, the Fermi energy E_F and the superconducting pair potential $\Delta(\boldsymbol{k})$. This Hamiltonian acts on two-component wave functions $\psi = (u, v)$ with electron part u and hole part v. With "hole" we mean an empty state in the conduction band, below the Fermi level. This should not be confused with the concept of a hole in a semiconductor, which refers to an empty state in the valence band.

Because electrons and holes in a superconductor refer to the same state, either filled or empty, there is a symmetry relation between elec-

trons and holes,

$$H_{\mathrm{BdG}}(\boldsymbol{k}) = -\tau_x H^*_{\mathrm{BdG}}(-\boldsymbol{k})\tau_x, \tag{1.8}$$

with the Pauli matrix τ_x acting in electron-hole space. The existence of this so-called particle-hole symmetry allows for new topological phases, just like time-reversal symmetry does [7].

Of particular interest are one-dimensional topological superconductors with broken time-reversal and spin-rotation symmetry. They can be realized in semiconductor - superconductor heterostructures (see Fig. 1.6) and their topologically protected end states are Majorana bound states – zero energy eigenstates that are their own electron-hole conjugate partners. These Majorana states are regarded as promising candidates for the realization of a topological quantum memory. In the following section this example is discussed from a transport perspective.

1.3.1 Example: Majorana wire

To illustrate how the concept of topology survives in a disordered system, I will now introduce the scattering approach to topology in a superconducting wire. To this end the wire is contacted by a metallic lead, just as in the experimental situation shown in Fig. 1.6.

When an electron moving inside the lead hits the superconductor, it is reflected back since transmission through the superconductor is suppressed by the superconducting gap. A unitary reflection matrix r relates incoming electronic states ψ_{in} to outgoing electronic states ψ_{out} at the interface (see Fig. 1.6):

$$\psi_{\mathrm{out}} = r\psi_{\mathrm{in}} = \begin{pmatrix} r_{ee} & r_{eh} \\ r_{he} & r_{hh} \end{pmatrix} \psi_{\mathrm{in}}. \tag{1.9}$$

The block r_{he} (r_{eh}) describes the process of Andreev reflection, where an electron (hole) hitting the superconductor is reflected as a hole (electron) while a Cooper pair is added to (removed from) the superconductor. This process is associated with a charge transfer of $2e$, leading to an electrical conductance of

$$G_{\mathrm{NS}} = G_0 \mathrm{Tr}\, r^\dagger_{\mathrm{he}} r_{\mathrm{he}}, \tag{1.10}$$

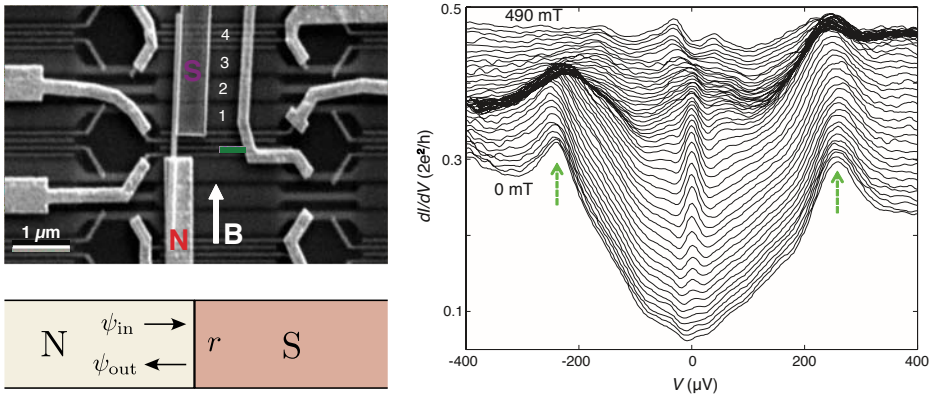

Figure 1.6. Upper panel: Scanning electron microscope image of a device designed to realize a one-dimensional topological superconductor: an InSb nanowire in proximity to a superconductor (S) is contacted by a normal metal lead (N). In the presence of a magnetic field, the wire is expected to make a transition into a topological state. Right panel: Differential conductance measurements for the setup on the left, as a function of bias voltage and magnetic field. For a range of magnetic field strengths a clear zero bias signature is observed in between the two superconducting gap peaks (green arrows), signaling the existence of Majorana bound states. Both from Ref. [13]. Reprinted with permission from AAAS. Lower panel: Schematic of the transport situation.

at zero bias voltage. Here, conductance was measured in units of the superconducting conductance quantum $G_0 = 2e^2/h$.

At the Fermi level (zero excitation energy), particle-hole symmetry requires $r_{hh} = r_{ee}^*$ and $r_{eh} = r_{he}^*$. Therefore the determinant of r has to be real. Since unitarity on the other hand forces the determinant to be of magnitude one, the number

$$Q = \det r \tag{1.11}$$

is a well defined integer, restricted to the two values $+1$ and -1. Because Q cannot change by any small perturbation of the Hamiltonian, it is a topological invariant. To change the value of this number, transmission through the superconductor has to become possible, breaking the unitarity of the reflection matrix. In this sense, the topology of the system is protected by the the superconducting gap.

We can straightforwardly use this definition of topology in a disordered system to show the delocalization at the topological phase tran-

sition: when the invariant Q changes, $\det r$ has to change sign and becomes zero at the transition point. This means that $r^\dagger r$ has a zero eigenvalue and thus one perfectly transmitting channel opens through the wire.

1.4 Random-matrix theory

Multiple scattering by impurities or boundaries introduces an element of randomness in mesoscopic systems that calls for a statistical description. An ensemble of nominally identical systems, differing only in the configuration of impurities or the precise shape of a boundary, corresponds to an ensemble of random Hamiltonians or random scattering matrices. Random-matrix theory tries to make statistical predictions by choosing the ensemble of matrices as generic as possible, constrained only by fundamental symmetries. A variety of applications of random-matrix theory to mesoscopic transport problems are known, summarized in detail in the books and reviews available [14–17]. In the following we will focus on the aspects directly relevant to this thesis.

1.4.1 Symmetry classes

We have already encountered two fundamental symmetries: time-reversal and particle-hole symmetry. They both come in different forms, depending, for example, on the presence or absence of spin-rotation symmetry. In particular, both the time-reversal operator $\mathcal{T}$ and the particle-hole conversion operator $\mathcal{C}$ are anti-unitary operators that square to either unity or minus unity. The time-reversal symmetry in Eq. (1.4) is, for example, given by the operator $\mathcal{T} = \mathcal{K}\sigma_y$ ($\mathcal{T}^2 = -1$) and the particle-hole symmetry in Eq. (1.8) by $\mathcal{C} = \mathcal{K}\tau_x$ ($\mathcal{C}^2 = 1$), with $\mathcal{K}$ denoting complex conjugation.

Time-reversal and particle-hole symmetry can be written in the form

$$H = \mathcal{T}H\mathcal{T}^{-1}, \tag{1.12}$$

$$H = -\mathcal{C}H\mathcal{C}^{-1}, \tag{1.13}$$

using the time-reversal and particle-hole conversion operators. One generally classifies systems regarding the presence or absence of these symmetries and and whether their operators square to $+1$ or -1. This leads

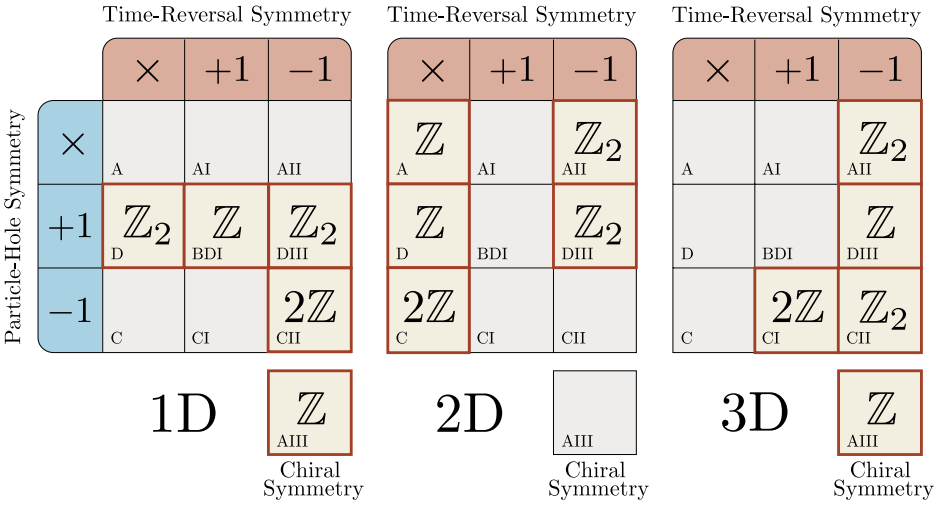

Figure 1.7. Classification of topological insulators and superconductors in one, two and three dimensions. For each dimension, the five symmetry classes in which topology is possible are indicated and the relevant types of invariants ($\mathbb{Z}$, $\mathbb{Z}_2$ or $2\mathbb{Z}$) are given. The symmetry classes are ordered depending on their time-reversal and particle-hole symmetry behavior: squaring to $+1$, -1 or absent ($\times$). The case of exclusive chiral symmetry is listed separately (symmetry class AIII). In the lower left corner of each box the name of the symmetry class is given. Design adapted from Ref. [18].

to nine different symmetry classes. A tenth symmetry class arises when we also consider the case where only chiral symmetry, $H = -\mathcal{T}\mathcal{C}H\mathcal{C}^{-1}\mathcal{T}^{-1}$, is present.

Each of these symmetry classes may or may not allow for topological invariants, depending on the dimensionality of the system [7]. An overview is given in Fig. 1.7, listing all the different symmetry classes and their formal names, which stem from Cartan's classification of symmetric spaces. The type of topological invariant if possible is given by the symbols $\mathbb{Z}$ (all integers), $\mathbb{Z}_2$ (0 or 1), and $2\mathbb{Z}$ (only even integers).

The examples of topological phases we discussed so far fit into this scheme as follows: in the quantum Hall effect (2D), no symmetries are present. Thus the relevant symmetry class is class A and topology is given by a $\mathbb{Z}$ topological winding number like in Sec.
refsec:WindingNumber. In the quantum spin Hall effect (2D) and the topological insulator (3D), time-reversal symmetry squares to -1 and

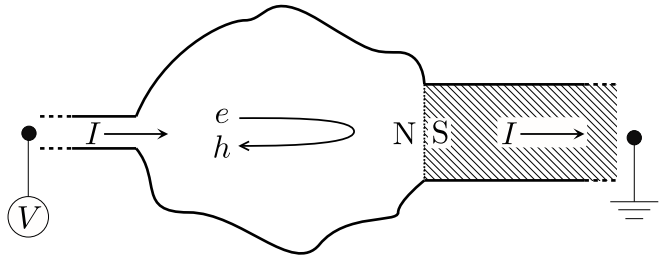

Figure 1.8. Chaotic scattering region with an interface between a normal metal (N) and a superconductor (S, shaded region). Andreev reflection at the NS interface converts a normal current (carried by electron and hole excitations e and h) into a supercurrent (carried by Cooper pairs). A normal metal electrode is connected to the dot via an N-mode point contact (narrow opening at the left). In this example the chaos is induced by the irregular shape of the dot region. Alternatively disorder in the scattering region does have a similar effect. The quantum transport phenomena in the setup can be characterized by a circular ensemble if the dwell time τ_D in the scattering region is much larger than the ergodic time $\tau_{\rm ergodic}$, the time scale on which a classical particle explores the whole phase space.

we are in class AII, with the $\mathbb{Z}_2$ topological invariants mentioned in Sec. refsec:othertopologicalphases. Finally, the Majorana wire (1D) of Sec. 1.3.1 obeys no time-reversal symmetry but a particle hole symmetry that squares to unity, placing it in symmetry class D with a Z_2 topological invariant.

1.4.2 Circular ensembles

The ensemble of scattering matrices used in random-matrix theory is called circular, because for a single scattering channel it would correspond to a uniform distribution of the phase shift on the unit circle. For N scattering channels the ensemble corresponds to a uniform distribution of the scattering matrix in the group of $N \times N$ unitary matrices, suitably restricted by the fundamental symmetries. Chaotic scattering by impurities or boundaries is known to be well described by a circular ensemble. An example relevant for this thesis is the chaotic normal-superconductor junction of Fig. 1.8. It is described by a unitary reflection matrix r and the electrical conductance is given by Eq. (1.10).

If no symmetry constraints are imposed on the unitary matrices, we call the ensemble of scattering matrices the circular unitary ensemble.

The presence or absence of time-reversal and/or particle-hole symmetry restricts the relevant matrix space to a smaller subset of unitary matrices, giving rise to several distinct circular ensembles.

1.5 Stroboscopic models

There is, up to now, still no rigorous analytical theory describing disorder-induced localization-delocalization transitions, including those that occur generically at a topological phase transition. Thus computer simulations are needed to calculate the scaling law and critical exponent associated with the diverging localization length at the transition.

Because the localization properties are universal, independent of microscopic details, we are free to choose a computationally efficient model even if it does not correspond to any particular physical realization. Stroboscopic models [19–22] are very well suited for this purpose since the propagation of wave functions is computationally very efficient for them, especially in higher dimensions. Although stroboscopic models do not correspond to a physical system in condensed matter, they can be realized experimentally with atomic matter waves in 1D optical lattices.

1.5.1 The quantum kicked rotator

A model is called stroboscopic when an otherwise freely propagating particle with kinetic energy $T(\boldsymbol{p})$ is subject to a driving potential $V(\boldsymbol{x})$ that is repeatedly turned on for an instant of time,

$$H = T(\boldsymbol{p}) + V(\boldsymbol{x}) \sum_n \delta(t - n\tau). \tag{1.14}$$

The period of the driving field is denoted τ. The prototypical example for a stroboscopic model is the so-called quantum kicked rotator [19–22], describing a particle with kinetic energy $T(p) = p^2/2m$ that is moving on a circle, $\theta \in [0, 2\pi)$, subject to the driving field $V(\theta) = K\cos(\theta)$. Consider such a particle, initially in a momentum eigenstate, $|\psi_0\rangle = \delta(p - p_0)$. The propagation of the wave function over one period of the driving field is given by a time evolution operator of the form

$$\mathcal{F} = e^{-iV(\theta)/\hbar} e^{-iT(p)/\hbar}, \qquad |\psi(t)\rangle = \mathcal{F}^t |\psi_0\rangle, \tag{1.15}$$

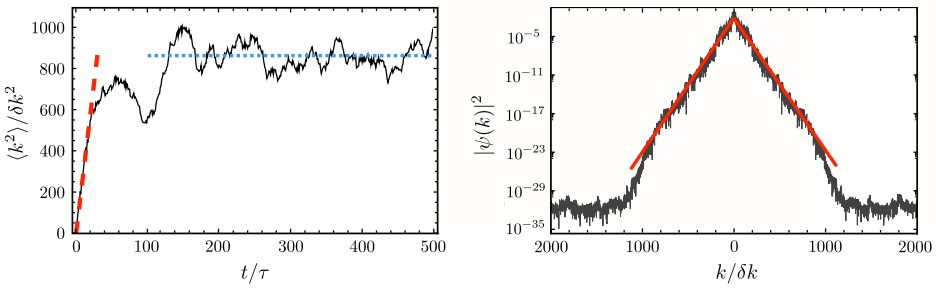

Figure 1.9. Particle in a quantum kicked rotator, initially in a momentum eigenstate $|\psi_0\rangle = \delta(p)$, is propagated in time. Left panel: Time dependence of the width of the wave function in momentum space. For a small number of kicks, the wave function spreads diffusively, $\langle k^2 \rangle \propto t$ (red dashed line). At larger times, interference effects become important and the wave function localizes, leading to a saturation of the spread (blue dotted line). Right panel: The wave function in momentum space after 1000 kicks. The exponentially localized shape is clearly visible (solid red lines, notice the logarithmic scale). Parameters used are $K = 6.66$ and $\hbar = m = 1$. Momentum is discrete with spacing δk due to the periodic real space.

also called Floquet operator. In the corresponding classical model, the particle performs a diffusive motion in momentum space over time, given a sufficiently large K. In the quantum kicked rotator, the particle wave function starts to spread diffusively in momentum space in the beginning but soon interference effects set in and the spreading slows down. For a large number of kicks, the spreading essentially stops and the wave function shows an exponentially localized shape, see Fig. 1.9.

1.5.2 Stroboscopic models in higher dimensions and the Anderson metal-insulator transition

Since the Floquet operator decomposes into two exponentials which are diagonal in real space and momentum space respectively, see Eq. (1.15), the computational cost of wave function propagation essentially reduces to two fast Fourier transforms. This is why stroboscopic models are computationally efficient. Another simplification arises for higher dimensional stroboscopic models since they can be simulated in one-dimension, as we will see in the following.

For example let us consider a three-dimensional stroboscopic model

of the form (1.14) with

$$T(\boldsymbol{p}) = \frac{p_1^2}{2} + \omega_2 p_2 + \omega_3 p_3, \tag{1.16}$$

$$V(\boldsymbol{x}) = K \cos x_1 (1 + \epsilon \cos x_2 \cos x_3), \tag{1.17}$$

and set $\tau = 1$ for brevity. If we choose the initial condition of a wave function as

$$\psi(x_1, x_2, x_3, t = 0) = \psi_1(x_1)\delta(x_2 - \phi_2)\delta(x_3 - \phi_3), \tag{1.18}$$

its propagation can be solved analytically in two of the dimensions:

$$\begin{aligned}\psi(x_1, x_2, x_3, t) &= \mathcal{F}^t \psi(x_1, x_2, x_3, t = 0) \\ &= \psi_1(x_1, t)\delta(x_2 - \phi_2 - \omega_2 t)\delta(x_3 - \phi_3 - \omega_3 t).\end{aligned} \tag{1.19}$$

Here, $\mathcal{F}$ is the Floquet operator of the model which decomposes into two exponentials just as in the example (1.15). The step to step evolution of the remaining dimension is given by a time-dependent Floquet operator

$$\psi_1(x_1, t + 1) = \tilde{\mathcal{F}}(t)\psi_1(x_1, t), \tag{1.20}$$

$$\tilde{\mathcal{F}}(t) = e^{-iV(x_1, \omega_2 t + \phi_2, \omega_3 t + \phi_3)/\hbar} e^{-ip_1^2/2\hbar}. \tag{1.21}$$

This is equivalent to the stepwise propagation of a wave function in a one-dimensional model with a time-dependent kicking potential of the form $V(x_1, \omega_2 t + \phi_2, \omega_3 t + \phi_3)$. The reduction from three to one dimension greatly simplifies the numerical simulation of the model. In the same way d-dimensional stroboscopic models can be reduced to a one-dimensional model, given that the kinetic term is linear in $d - 1$ dimensions.

The model considered here features an Anderson metal-insulator transition in momentum space. This means that when the parameter K is decreased (e.g. at fixed $\epsilon \sim 0.5$), the evolution of the wave functions changes: for large K they spread diffusively while for small K they localize (see phase diagram in Fig. 1.10). The corresponding one-dimensional model for this three-dimensional transition was realized experimentally with atomic matter waves in a cold atoms setup [23]. In the experiment, Cs atoms with kinetic energy $p_1^2/2$ were subjected to a stroboscopic kicking potential, produced by a pulsed standing laser wave. In this way the time evolution of $\psi_1(x_1)$ could be simulated, allowing for measurements

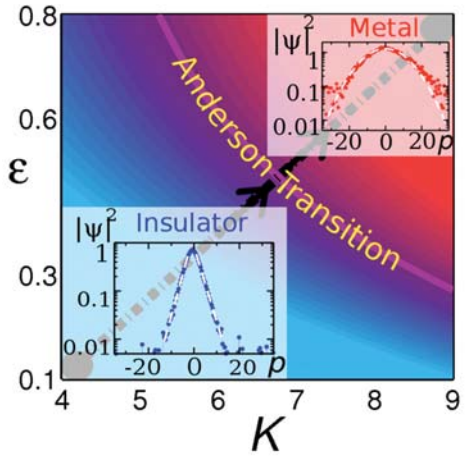

Figure 1.10. Phase diagram of the stroboscopic model in Eq. (1.17), from numerical simulations. The Anderson transition line separates the localized phase (blue) from the diffusive metallic phase (red). In the corresponding atomic matter wave experiment, the parameters were swept along the diagonal dash-dotted line. The insets show the experimentally observed momentum distributions, localized in the blue region and Gaussian in the diffusive (blue) region. From Ref. [23]. Copyright (2008) by the American Physical Society.

of the momentum distribution after some time of propagation. The critical exponent characterizing the divergence of the localization length at the transition could be extracted from these measurements and was found to be in accordance with numerical predictions.

1.6 This thesis

In the following a brief description of each chapter is given.

1.6.1 Chapter 2

When the chaotic superconducting scattering region introduced in Fig. 1.8 is coupled to two leads, also transport from one lead to the other becomes possible, see Fig. 1.11. The scattering matrix

$$S = \begin{pmatrix} r & t' \\ t & r' \end{pmatrix}, \tag{1.22}$$

for this situation is not solely a reflection matrix but also contains transmission blocks t and t'. Since the quasiparticles in a superconducting region are superpositions of electrons and holes they do not carry a definite charge and thus their transmission is not associated with an electrical current. But they have a fixed energy and carry a thermal current, with thermal conductance

$$G_{\text{th}} = G_0^{\text{th}} \operatorname{Tr} t^\dagger t = G_0^{\text{th}} \sum_n T_n, \tag{1.23}$$

at low temperatures T. Here, conductance is measured in units of $G_0^{\text{th}} = \pi^2 k_B^2 T/6h$ and we denoted the eigenvalues of $t^\dagger t$ by T_n.

In chapter two we study the thermal transport statistics of such a chaotic superconducting quantum dot using random-matrix theory. To this end we calculate the probability distribution $P(\{T_n\})$ of independent transmission eigenvalues from which all moments of the thermal conductance at the Fermi level can be extracted. We distinguish between four superconducting symmetry classes which give rise to four circular ensembles of scattering matrices, with distinct probability distributions. In this way we are able to deduce the generic influence of the symmetries on the thermal conductance, in form of weak (anti-)localization corrections. Compared to the statistics of the electrical conductance in non-superconducting ensembles, the most striking differences appear in the single-channel limit, which is not accessible in normal electronic gases. We show how this single-channel limit can be reached using a topological insulator or superconductor, without running into the problem of fermion doubling.

1.6.2 Chapter 3

In the third chapter we determine the influence of topology on the Andreev reflection properties of chaotic normal-metal–superconductor junctions. We already introduced the relevant setup in Fig. 1.8. The electrical conductance of the NS junction can be calculated from

$$G = G_0 \sum_n R_n, \tag{1.24}$$

following Eq. (1.10), but expressed in terms of the eigenvalues R_n of $r_{he}^\dagger r_{he}$, the so-called Andreev reflection eigenvalues.

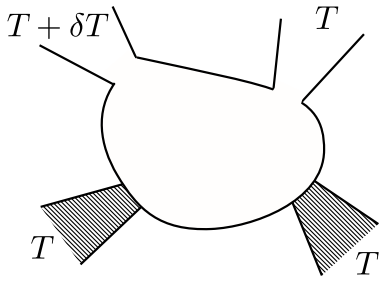

Figure 1.11. Quantum dot in a two-dimensional electron gas, connected to a pair of superconductors (shaded) and to two normal-metal reservoirs. One of the normal reservoirs is at a slightly elevated temperature $T + \delta T$. The second superconductor is needed to ensure the presence of time-reversal symmetry in the symmetry classes DIII and CI.

It is well established that the generic influence of symmetries on the conductance statistics can be determined by random-matrix theory. With the realization that topology constrains the reflection matrix just as symmetries do (e.g. $Q = \det r$ in symmetry class D), it becomes apparent that averaging over all possible reflection matrices of a symmetry class implies averaging over different topological phases. Since we want to disentangle the contributions from distinct topological phases we thus have to subdivide the known superconducting circular ensembles.

By calculating the probability distribution of the Andreev reflection eigenvalues R_n for these subdivisions of ensembles, we investigate the influence of topology on the electrical conductance G. We show that the dependence of G on the topological quantum number Q is non-perturbative in the number N of scattering channels. As a consequence a large-N effect such as weak localization cannot probe the topological quantum number. For small N we calculate the full distribution $P(G)$ of the conductance and find qualitative differences in the topologically trivial and nontrivial phases.

1.6.3 Chapter 4

The fourth chapter of the thesis introduces a setup for the unambiguous detection of topological superconductivity: a quantum point contact attached to a superconducting wire, as depicted in the inset of Fig. 1.12. The main part of the figure is a plot of the conductance G as a function of contact width or Fermi energy, showing plateaus at half-integer

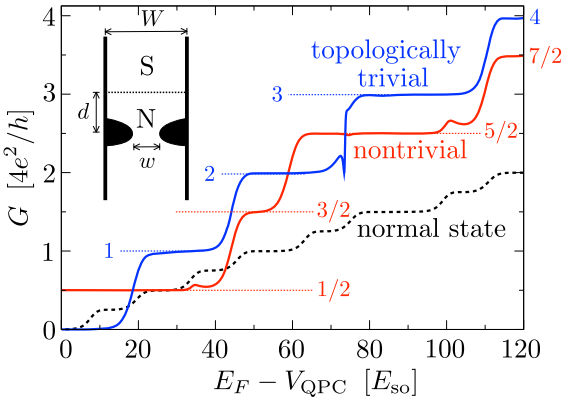

Figure 1.12. Conductance of a ballistic normal-metal–superconductor junction, with the superconductor in a topologically trivial (blue curve) or nontrivial phase (red curve). The black dashed curve is for an entirely normal system. By varying the potential V_{QPC} at constant Fermi energy E_F, the width of a point contact is varied in the setup (see inset).

multiples of $4e^2/h$ if the superconductor is in a topologically nontrivial phase. In contrast, the plateaus are at the usual integer multiples in the topologically trivial phase. Disorder destroys all plateaus except the first, which remains precisely quantized, consistent with previous results for a tunnel contact. The advantage of a ballistic contact over a tunnel contact as a probe of the topological phase is the strongly reduced sensitivity to finite voltage or temperature.

By now, experiments have demonstrated signatures of topology in superconducting wires, with one example summarized in Fig. 1.6. Nevertheless, the quantized nature of the conductance peak height has not been observed so far, presumably due to finite temperatures. The setup we propose here could be a step forward on the quest to detect this quantized peak height.

1.6.4 Chapter 5

In the fifth chapter the focus shifts to time-reversal invariant nodal superconductors. Although they are not topological in the usual sense, a variety of lower dimensional topological invariants can be defined that have strong impact on the transport properties of these systems.

Existing expressions for the topological invariant are based on the

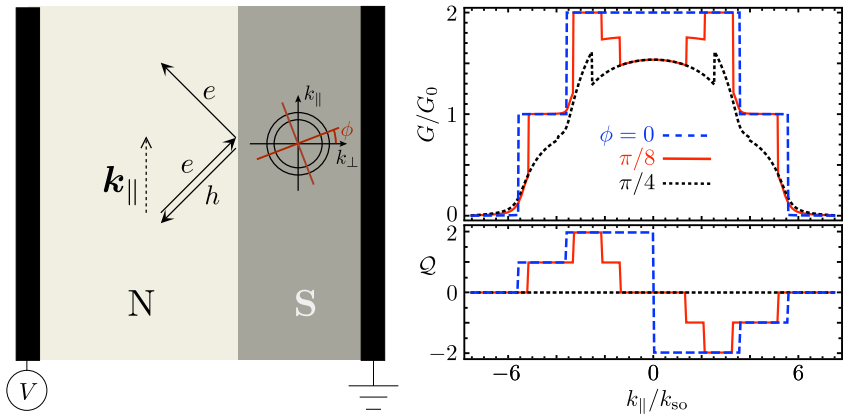

Figure 1.13. Left panel: reflection processes at a planar interface between a normal-metal and a gapless superconductor. The sketch in the superconducting region shows the Fermi surfaces and nodal lines for the specific case of a d-wave superconductor with Rashba spin-orbit coupling. Both the electrical conductance G and $\mathbb{Z}$ topological invariant $\mathcal{Q}$ are plotted for this case in the right panel, shown as a function of momentum $k_\parallel$ along the NS interface and angle ϕ between the interface and the nodal line of the superconductor.

Hamiltonian of an infinite system. We introduce an alternative formulation in terms of the Andreev reflection matrix of a planar normal-metal–superconductor interface (left panel of Fig. 1.13). This allows to relate the topological invariant to the angle-resolved Andreev conductance. We discuss a variety of symmetry classes that may arise depending on additional unitary symmetries of the reflection matrix. The condition for the quantization of the conductance is derived in each symmetry class and is tested on a model for a 2D or 3D superconductor with spin-singlet and spin-triplet pairing, mixed by Rashba spin-orbit interaction. The right panel of Fig. 1.13 shows our results for the case of a two-dimensional d-wave superconductor with spin-singlet pairing.

1.6.5 Chapter 6

In chapter six we introduce the concept of topology into stroboscopic models, explicitly constructing a two-dimensional periodically kicked system with a topological phase transition in the quantum Hall universality class.

Our model is essentially a stroboscopic version of the toy model in

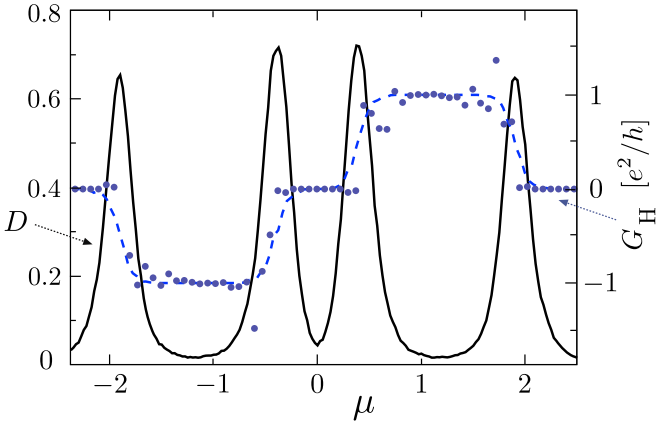

Figure 1.14. Left axis: Time-dependent diffusion coefficient (solid curve) after a sufficiently long time of propagation, showing four localization-delocalization transitions. Right axis: Four-terminal Hall conductance G_{H} (data points) and topological invariant $\mathcal{I}$ (dashed curve), demonstrating that these are *topological* phase transitions.

Sec. 1.2.1, combined with a localizing potential term. As we tune the system through a topological phase transition, the localization length of the system diverges. This can be observed in the time-dependent diffusion constant

$$D(t) = \langle \psi(t)|x^2|\psi(t)\rangle / t, \tag{1.25}$$

which converges to zero with increasing propagation time if the wave function localizes. In contrast it stays finite at the critical point. For our model D is plotted in Fig. 1.14 for a sufficiently large time, showing the presence of four localization-delocalization transitions where the topology of the system changes. We quantitatively investigate this localization-delocalization behavior, determining the critical exponent ν of the transition. Since the critical exponent is a universal property depending only on the symmetries and the dimensionality of the model, our result straightforwardly applies to corresponding solid state systems as well.

In order to obtain our results, we used the dimensional reduction scheme introduced in Sec. 1.5.2 and were thus able to study the quantum Hall transition in a one-dimensional system. Not only is this reduction to 1D computationally very efficient, it also provides a possible

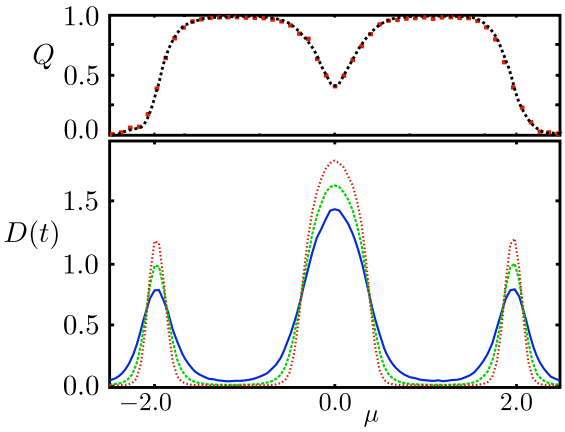

Figure 1.15. *Bottom panel:* Time-dependent diffusion coefficient for times $t = 10^6$ (red), $t = 10^5$ (green) and $t = 10^4$ (blue), showing three metallic regions. The points of intersection of these curves locate the metal-insulator transition. *Top panel:* Topological quantum number used to distinguish the topologically trivial ($Q = 0$) and nontrivial ($Q = 1$) insulators. In the metallic regions Q is not quantized.

route to perform experiments on the 2D quantum Hall effect using cold atoms in a 1D optical lattice. The approach we introduce in this chapter to investigate the quantum Hall transition can readily be generalized to other symmetry classes and dimensions, making it possible to study higher-dimensional systems in one spatial dimension as well.

1.6.6 Chapter 7

Following the methods introduced in chapter six we construct a stroboscopic model that realizes the $\mathbb{Z}_2$ topology of the quantum spin Hall effect. Due to the presence of time-reversal symmetry, the transition from the topological to the trivial phase does not happen directly as in the quantum Hall effect but only via an extended metallic region in parameter space.

This metallic phase is a bit unusual since wave functions spread faster than in a normal diffusion process. Thus the time-dependent diffusion coefficient does not tend to a constant value for large times, in contrast to the situation at the critical point. This is illustrated in Fig. 1.15 for our model. The plotted $\mathbb{Z}_2$ topological invariant was calculated

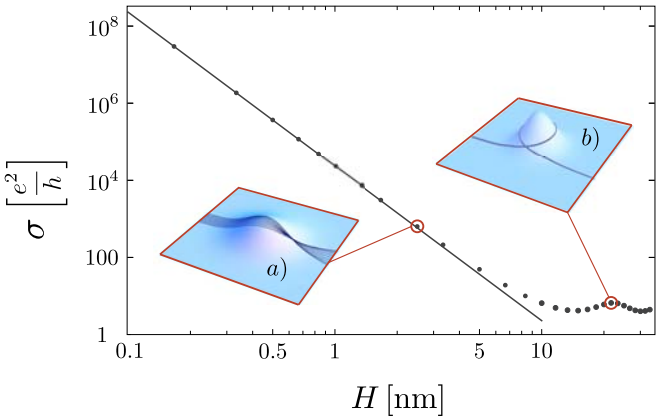

Figure 1.16. Surface conductivity of a topological insulator as a function of the height H of randomly positioned Gaussian surface deformations (width $W = 10\,\text{nm}$). The insets illustrate characteristic scattering situations that arise for different heights of the deformations. Dots represent numerical results whereas the line shows the analytical solution we derived in the shallow deformation limit.

using a scattering formulation that remains valid in the presence of disorder.

Once again we can use the dimensional reduction scheme to find an effective one-dimensional description of the localization behavior of the model. In the same way as in chapter six we study the delocalization at the metal insulator transitions quantitatively, finding that the critical exponent does not depend on the topological invariant, in agreement with earlier independent results from the network model of the quantum spin Hall effect.

1.6.7 Chapter 8

In chapter eight we consider the classical ballistic dynamics of massless electrons on the conducting surface of a three-dimensional topological insulator, influenced by random variations of the surface height. Since electrons traveling on the surface of a topological insulator are constrained to follow its geometry, they essentially move in a curved space. Their free motion is thus described by so-called geodesic lines, solutions of the geodesic equation of motion. In the presence of surface deformations these geodesic lines bend, a process we call geodesic scat-

tering. We solve the geodesic equation and the Boltzmann equation in the limit of shallow deformations to obtain the scattering cross section and the conductivity σ, see Fig. 1.16. At large surface electron densities n this geodesic scattering mechanism (with $\sigma \propto \sqrt{n}$) is more effective at limiting the surface conductivity than electrostatic potential scattering.

Bibliography

[1] M. Z. Hasan and C. L. Kane, Rev. Mod. Phys. **82**, 3045 (2010).

[2] X.-L. Qi and S.-C. Zhang, Rev. Mod. Phys. **83**, 1057 (2011).

[3] C. L. Kane and J. E. Moore, Physics World **24**, 32 (2011).

[4] C. W. J. Beenakker, arXiv:1112.1950, scheduled for vol. 4 of Annual Review of Condensed Matter Physics.

[5] J. Alicea, Rep. Prog. Phys. **75**, 076501 (2012).

[6] X.-L. Qi, Y.-S. Wu, and S.-C. Zhang, Phys. Rev. B **74**, 085308 (2006).

[7] S. Ryu, A. P. Schnyder, A. Furusaki, and A. W. W. Ludwig, New J. Phys. **12**, 065010 (2010).

[8] M. König, S. Wiedmann, C. Brüne, A. Roth, H. Buhmann, L. W. Molenkamp, X. L. Qi, and S. C. Zhang, Science **318**, 766 (2007).

[9] D. Hsieh, D. Qian, L. Wray, Y. Xia, Y. S. Hor, R. J. Cava, and M. Z. Hasan, Nature **452**, 970 (2008).

[10] Y. Xia, D. Qian, D. Hsieh, L. Wray, A. Pal, H. Lin, A. Bansil, D. Grauer, Y. S. Hor, R. J. Cava, and M. Z. Hasan, Nature Physics **5**, 398 (2009).

[11] P. A. Lee and T. V. Ramakrishnan, Rev. Mod. Phys. **57**, 287 (1985).

[12] F. Evers and A. D. Mirlin, Rev. Mod. Phys. **80**, 1355 (2008).

[13] V. Mourik, K. Zuo, S. M. Frolov, S. R. Plissard, E. P. A. M. Bakkers and L. P. Kouwenhoven, Science **336**, 1003 (2012).

[14] *The Oxford Handbook of Random Matrix Theory*, edited by G. Akemann, J. Baik, and P. Di Francesco (Oxford University Press, Oxford, 2011).

[15] P. J. Forrester, *Log-Gases and Random Matrices* (Princeton University Press, Princeton, 2010).

[16] M. L. Mehta, *Random Matrices* (Academic Press, New York, 1991).

[17] C. W. J. Beenakker, Rev. Mod. Phys. **69**, 731 (1997).

[18] T. Kitagawa, M. Rudner, E. Berg, and E. Demler, Phys. Rev. A **82**, 033429 (2010).

[19] G. Casati, B. V. Chirikov, F. M. Izraelev, and J. Ford, Lecture Notes in Physics, **93**, 334 (1979).

[20] F.M. Izrailev, Phys. Rep. **196**, 299 (1990).

[21] H.-J. Stöckmann, *Quantum Chaos: An Introduction* (Cambridge University Press, Cambridge, 1999).

[22] F. Haake, *Quantum Signatures of Chaos* (Springer, Berlin; New York, 3rd edition, 2010).

[23] J. Chabé, G. Lemarié, B. Grémaud, D. Delande, P. Szriftgiser, and J. Garreau, Phys. Rev. Lett. **101**, 255702 (2008).

Chapter 2

Random-matrix theory of thermal conduction in superconducting quantum dots

2.1 Introduction

The Landauer approach to quantum transport [1–3] relates a transport property (such as the electrical or thermal conductance) to the eigenvalues T_n of the transmission matrix product $tt^\dagger$. If transport takes place through a region with chaotic scattering (typically a quantum dot), random-matrix theory (RMT) provides a statistical description [4–6]. While the properties of individual chaotic systems are highly sensitive to the microscopic parameters of the scattering region, such as its geometry or the arrangements of impurities, they obey universal statistical features, independent of these details, on energy scales below the Thouless energy (the inverse of the dwell time). The distribution $P(\{T_n\})$ of the transmission eigenvalues then naturally emerges as the determining quantity for the distribution of the transport properties.

While microscopic details do not influence the statistics, the role of symmetries is essential. According to Dyson [7, 8], there are three symmetry classes in normal (non-superconducting) electronic systems, characterized by a symmetry index β depending on the presence or absence

Ensemble name	**CUE**	**COE**	**CSE**
Symmetry class	A	AI	AII
S-matrix elements	complex	complex	complex
S-matrix space	unitary	unitary symmetric	unitary selfdual
Time-reversal symmetry	$\times$	$S = S^T$	$S = \sigma_2 S^T \sigma_2$
Spin-rotation symmetry	$\times$ or ✓	✓	$\times$
degeneracy d of T_n	1 or 2	2	2
β	2	1	4

Table 2.1. Classification of the Wigner-Dyson scattering matrix ensembles for normal (non-superconducting) systems, with the parameter β in the distribution (2.1) of the electrical conductance. (The parameter $\gamma \equiv 0$ in these ensembles.) The abbreviations C(U,O,S)E signify Circular (Unitary,Orthogonal,Symplectic) Ensemble. The Pauli matrix σ_j acts on the spin degree of freedom.

of time-reversal and spin-rotation symmetry (cf. Table 2.1). The transmission eigenvalue distribution for these three RMT ensembles is known [9, 10]. For a single d-fold degenerate channel at the entrance and exit of the quantum dot this gives the distribution

$$P(g) \propto g^{-1+\beta/2}, \quad 0 < g < 1, \tag{2.1}$$

of the electrical conductance g (in units of de^2/h). The full distribution $P(\{T_n\})$ has found a variety of physical applications [11], and has also been used in a more mathematical context to obtain exact results for electrical conductance and shot noise [12, 13] and to uncover connections between quantum chaos and integrable models [14].

As first shown by Altland and Zirnbauer [15], Dyson's classification scheme becomes insufficient in the presence of superconducting order: The particle-hole symmetry of the Bogoliubov-De Gennes Hamiltonian produces four new symmetry classes [16–18]. Depending again on the presence or absence of time-reversal and spin-rotation symmetry, these classes are characterized by β and a second symmetry index γ (cf. Table 2.2) [19, 20]. As we show in this chapter, the analogous result to Eq. (2.1) is

$$P(g) \propto g^{-1+\beta/2}(1-g)^{\gamma/2}, \quad 0 < g < 1, \tag{2.2}$$

where now g is the *thermal* conductance in units of $d\pi^2 k_B^2 T_0/6h$ (at temperature T_0). We consider thermal transport instead of electrical transport because the Bogoliubov quasiparticles that are transmitted through a superconducting quantum dot carry a definite amount of energy rather

Ensemble name	**CRE**	**T-CRE**	**CQE**	**T-CQE**
Symmetry class	D	DIII	C	CI
S-matrix elements	real	real	quaternion	quaternion
S-matrix space	orthogonal	orthogonal selfdual	symplectic	symplectic symmetric
Particle-hole symmetry	$S = S^*$	$S = S^*$	$S = \tau_2 S^* \tau_2$	$S = \tau_2 S^* \tau_2$
Time-reversal symmetry	$\times$	$S = \sigma_2 S^T \sigma_2$	$\times$	$S = S^T$
Spin-rotation symmetry	$\times$	$\times$	✓	✓
degeneracy d of T_n	1	2	4	4
β	1	2	4	2
γ	-1	-1	2	1

Table 2.2. Classification of the Altland-Zirnbauer scattering matrix ensembles for superconducting systems. For each ensemble the parameters β, γ in the distribution (2.2) of the thermal conductance are indicated. The Pauli matrices σ_j and τ_j act on, respectively the spin and particle-hole degrees of freedom. The abbreviations (T)-C(R,Q)E signify (Time-reversal-symmetric)-Circular (Real,Quaternion) Ensemble.

than a definite amount of charge. (Charge is not conserved upon Andreev reflection at the superconductor, when charge-2e Cooper pairs are absorbed by the superconducting condensate.)

Concerning previous related studies, we note that the electrical conductance has been investigated by Altland and Zirnbauer [15], but not the thermal conductance. Thermal transport in superconductors has been studied in connection with the thermal quantum Hall effect in two dimensions [21–23], and also in connection with one-dimensional localization [24, 25]. The present study complements these works by addressing the zero-dimensional regime in connection with chaotic scattering.

The outline of this chapter is as follows. Sections 2.2 and 2.3 formulate the problem and present $P(\{T_n\})$. In Sec. 2.4 we then apply this to the statistics of the thermal conductance. The probability distribution (2.2) in the single-channel limit is of particular interest (since it is furthest from a Gaussian), but it can only be reached in the Andreev quantum dot in the presence of spin-rotation symmetry. A fermion-doubling problem stands as an obstacle when spin-rotation symmetry is broken. We show how to overcome this obstacle in Sec. 2.5 using topological phases of matter [26–28] (topological superconductors or insulators). We close in Sec. 2.6 with a summary and a proposal to realize the superconducting ensembles in graphene.

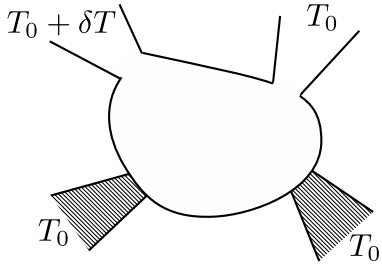

Figure 2.1. Quantum dot in a two-dimensional electron gas, connected to a pair of superconductors (shaded) and to two normal-metal reservoirs. One of the normal reservoirs is at a slightly elevated temperature $T_0 + \delta T$.

2.2 Formulation of the problem

2.2.1 Andreev quantum dot

An Andreev quantum dot, or Andreev billiard, is a confined region in a two-dimensional electron gas connected to superconducting electrodes (see Fig. 2.1). Electronic transport through this system is governed by the interplay of chaotic scattering at the boundaries of the quantum dot and Andreev reflection at the superconductors. (See Ref. 30 for a review.) We assume s-wave superconductors, with an isotropic gap Δ, so for excitation energies $E < \Delta$ there are no modes propagating into the superconductors. In order to enable quasiparticle transport, the cavity has two additional leads connected to it which support N_1, N_2 propagating modes (not counting degeneracies). The leads connect the cavity to normal-metal reservoirs in local thermal equilibrium.

Quasiparticle transmission is possible only if the excitations of the Andreev quantum dot (without the leads) are gapless. This is also necessary for the excitations to explore the phase space of the cavity, an essential requirement for chaotic scattering. Gapless excitations are ensured by taking two superconducting electrodes with the same contact resistance and a phase difference π. This value of the phase difference closes the gap while respecting time-reversal invariance (because phase differences π and $-\pi$ are equivalent). Time-reversal invariance can be broken by application of a magnetic field, perpendicular to the plane of the dot. (A sufficiently strong magnetic field closes the gap, so then the π-phase difference of the superconductors is not needed and a single superconducting electrode is sufficient.) Spin-rotation symmetry can be

broken by spin-orbit coupling. An ensemble of chaotic systems can be generated, for example, by varying the shape of the quantum dot or by a random arrangement of impurities.

In global equilibrium the superconducting and normal-metal contacts are all at the same temperature T_0 and Fermi energy (or chemical potential) E_F. For thermal conduction in the linear response regime we raise the temperature of one of the normal metals by an amount $\delta T \ll T_0$. The thermal conductance G is the heat current between the normal reservoirs divided by δT. (The reservoirs are kept at the same chemical potential, so there is no thermo-electric contribution to the heat current.)

If $k_B T_0$ is small compared to the Thouless energy (the inverse dwell time in the quantum dot), then G is determined by the transmission eigenvalues at the Fermi energy,

$$G = dG_0 \sum_n T_n. \tag{2.3}$$

The sum runs over the $\min(N_1, N_2)$ nonzero transmission eigenvalues T_n, with spin and/or particle-hole degeneracy accounted for by the factor d. The thermal conductance quantum for superconducting systems is $G_0 = \pi^2 k_B^2 T_0/6h$, one-half the normal-state value [2, 29].

2.2.2 Scattering matrix ensembles

The scattering matrix S is a unitary matrix of dimension $(N_1 + N_2) \times (N_1 + N_2)$ that relates the amplitudes of outgoing and incoming modes in the two leads connected to the normal reservoirs. The energy is fixed at the Fermi level ($E = 0$). Four sub-blocks of S define the transmission and reflection matrices,

$$S = \begin{pmatrix} r_{N_1 \times N_1} & t'_{N_1 \times N_2} \\ t_{N_2 \times N_1} & r'_{N_2 \times N_2} \end{pmatrix}. \tag{2.4}$$

(The subscripts refer to the dimension of the blocks.) Table 2.2 lists the Altland-Zirnbauer symmetry classes to which S belongs, and the corresponding RMT ensembles [15–18]. We briefly discuss the various entries in that table.

In the case of systems without spin-rotation symmetry, it is convenient to choose the Majorana basis in which S has real matrix elements.[1]

[1]The basis in which S is real is constructed by taking the combinations $|e\rangle + |h\rangle$,

Without time-reversal symmetry (symmetry class D), the scattering matrix space is thus the orthogonal group. The presence of time-reversal symmetry imposes the additional constraint $S = \sigma_2 S^T \sigma_2$, where σ_j is a Pauli matrix in spin-space, and T indicates the matrix transpose. The scattering matrices in this symmetry class DIII are self-dual orthogonal matrices. (The combination $\sigma_2 A^T \sigma_2$ is the so-called dual of the matrix A.)

If spin-rotation symmetry is preserved, the spin degree of freedom can be omitted if we use the electron-hole basis (rather than the Majorana basis). The electron-hole symmetry relation then reads $S = \tau_2 S^* \tau_2$, where now the Pauli matrices τ_j act on the electron-hole degree of freedom. The matrix elements of S can be written in the quaternion form $a_0\tau_0 + i\sum_{n=1}^{3} a_n \tau_n$, with real coefficients a_n. The scattering matrix space for the symmetry class C without time-reversal symmetry is the symplectic group, additionally restricted to symmetric matrices in the presence of time-reversal symmetry (class CI).

Henceforth we assume that the quantum dot is connected to the leads via ballistic point contacts. The RMT ensembles in this case are defined by S being uniformly distributed with respect to the invariant measure $d\mu(S)$ in the scattering matrix space for each particular symmetry class [15]. (For the distribution in the case that the contacts contain tunnel barriers, see Ref. 31.)

It is convenient to have names for the Altland-Zirnbauer ensembles, analogous to the existing names for the Dyson ensembles. Zirnbauer [18] has stressed that the names D,DIII,C,CI given to the symmetry classes (derived from Cartan's classification of symmetric spaces) should be kept distinct from the ensembles, because a single symmetry class can produce different ensembles. Following Ref. 32, we will refer to the Circular Real Ensemble (CRE) and Circular Quaternion Ensemble (CQE) of uniformly distributed real or quaternion unitary matrices. The presence of time-reversal symmetry is indicated by T-CRE and T-CQE. (The prefix T can also be thought of as referring to the matrix transpose in the restrictions imposed by time-reversal symmetry.)

$i|e\rangle - i|h\rangle$ of the electron and hole states $|e\rangle$, $|h\rangle$ with the same spin and mode quantum numbers. The corresponding creation and annihilation operators are identical, so these basis states represent Majorana fermions.

2.3 Transmission eigenvalue distribution

2.3.1 Joint probability distribution

Because of unitarity, the matrix products $tt^\dagger$ and $t't'^\dagger$ have the same set $T_1, T_2, \ldots T_{N_{\min}}$ of nonzero eigenvalues, with $N_{\min} = \min(N_1, N_2)$. The calculation of the joint probability distribution $P(\{T_n\})$ of these transmission eigenvalues from the invariant measure $d\mu(S)$ is outlined in App. 2.A [38]. (It is equivalent to the calculation of the Jacobian given in Ref. 24.) The result is

$$P(\{T_n\}) \propto \prod_i T_i^{(\beta/2)(N_1-N_2)} T_i^{-1+\beta/2} (1-T_i)^{\gamma/2} \times \prod_{j<k} |T_k - T_j|^\beta. \tag{2.5}$$

The values of the parameters β and γ characterizing the Altland-Zirnbauer symmetry classes are listed in Table 2.2.

The distribution (2.5) differs from the result [4, 9, 10] in the Dyson ensembles by the factor $\prod_i (1-T_i)^{\gamma/2}$. Depending on the sign of γ, this factor produces a repulsion or attraction of the T_i's to perfect *transmission*. In contrast, the factor $\prod_i T_i^{-1+\beta/2}$, which exists also in the Dyson ensembles, repels or attracts the T_i's to perfect *reflection*. The distributions $P(T_1)$ for $N_1 = N_2 = 1$ in the various ensembles are plotted in Fig. 2.2. In view of Eq. (2.3), this is just the distribution (2.2) of the thermal conductance in the single-channel limit announced in the Introduction. (How to actually reach this limit is discussed in following Sections.)

2.3.2 Eigenvalue density

The density $\rho(T)$ of the transmission eigenvalues is defined by

$$\rho(T) = \left\langle \sum_n \delta(T - T_n) \right\rangle, \tag{2.6}$$

where $\langle \cdots \rangle$ denotes an average with distribution (2.5). It can be calculated for $N_1, N_2 \gg 1$ using the general methods of RMT [4].

To leading order in N_1, N_2 the eigenvalue density approaches the β

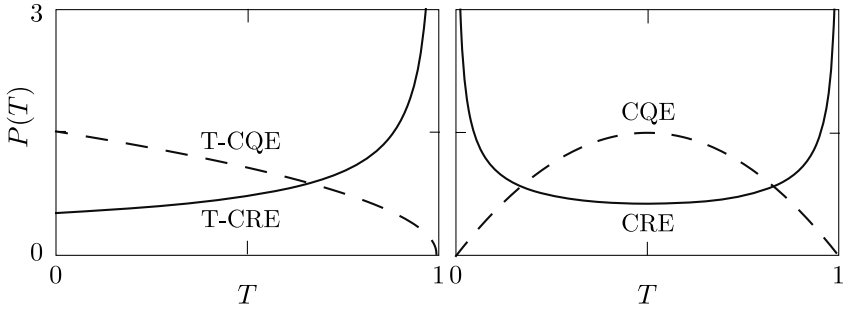

Figure 2.2. Probability distribution (2.5) in the case $N_1 = N_2 = 1$ of a single (d-fold degenerate) transmission eigenvalue T, which then corresponds to the (dimensionless) thermal conductance $g = G/dG_0$. The four curves correspond to the four superconducting ensembles in Table 2.2.

and γ independent limiting form [4, 9, 10]

$$\rho_0(T) = \frac{N_1 + N_2}{2\pi} \left(\frac{T - T_c}{1 - T} \right)^{1/2} \frac{1}{T} \times \Theta(1 - T)\Theta(T - T_c), \tag{2.7}$$

$$T_c = \frac{(N_1 - N_2)^2}{(N_1 + N_2)^2}. \tag{2.8}$$

(The function $\Theta(x)$ is the unit step function, $\Theta(x) = 0$ if $x < 0$ and $\Theta(x) = 1$ if $x > 0$.) The approach to this ensemble-independent density with increasing $N_1 = N_2$ is shown in Fig. 2.3 for one of the ensembles.

The first correction $\delta\rho$ to ρ_0 is of order unity in N_1, N_2, given by

$$\begin{aligned} \delta\rho(T) = {} & \tfrac{1}{4}(1 - 2/\beta)[\delta(1 - T) - \delta(T - T_c)] \\ & - \tfrac{1}{2}(\gamma/\beta)\delta(1 - T) \\ & + \frac{1}{2\pi}(\gamma/\beta)\frac{\Theta(1 - T)\Theta(T - T_c)}{\sqrt{(1 - T)(T - T_c)}}. \end{aligned} \tag{2.9}$$

We will use this expression in Sec. 2.4.2 to calculate the weak localization effect on the thermal conductance.

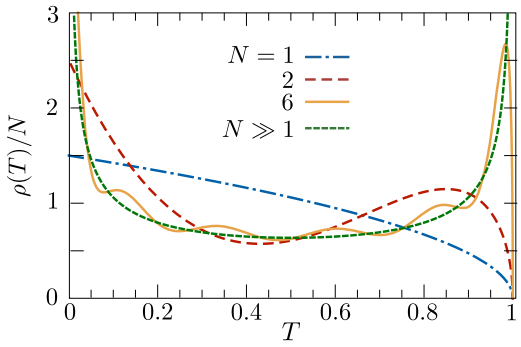

Figure 2.3. Transmission eigenvalue densities in the T-CQE for various numbers $N = N_1 = N_2$ of transmission eigenvalues, calculated from Eq. (2.5). The large-N limit is the same for each ensemble.

2.4 Distribution of the thermal conductance

2.4.1 Minimal channel number

The strikingly different probability distributions (2.1) and (2.2) in the normal and superconducting ensembles apply to transmission between contacts with a single (possibly degenerate) non-vanishing transmission eigenvalue. For the normal ensembles a narrow point contact suffices to reach this single-channel limit. In the superconducting ensembles a narrow point contact is not in general sufficient, because electrons and holes may still contribute independently to the thermal conductance.

Consider the Andreev quantum dot of Fig. 2.1. The minimal number of propagating modes incident on the quantum dot from each of the two leads is $2 \times 2 = 4$: a factor-of-two counts the spin directions, and another factor-of-two the electron-hole degrees of freedom. In the CQE and T-CQE the four transmission eigenvalues are all degenerate, so we have reached the single-channel limit where the distribution (2.2) applies.

The situation is different in the CRE and T-CRE. In the T-CRE two of the four transmission eigenvalues are independent (and a two-fold Kramers degeneracy remains). In the CRE all four transmission eigenvalues are independent, but two of the four can be eliminated by spin-polarizing the leads by means of a sufficiently strong magnetic field. So the case with two independent transmission eigenvalues (with degeneracy factor $d = 2$ for the T-CRE) is minimal in the Andreev quantum dot with broken spin-rotation symmetry.

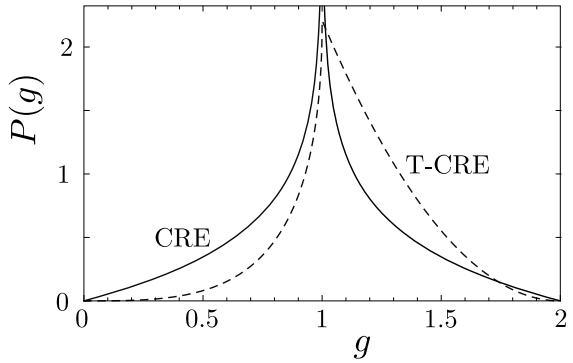

Figure 2.4. Probability distribution of the dimensionless thermal conductance in the two ensembles with broken spin-rotation symmetry, for two independent transmission eigenvalues ($N_1 = N_2 = 2$). This is the minimal channel number in an Andreev quantum dot. To reach the single-channel case in the CRE or T-CRE ($N_1 = N_2 = 1$, plotted in Fig. 2.2) one needs a topological phase of matter, as discussed in Sec. 2.5.

We have calculated the corresponding probability distribution of the (dimensionless) thermal conductance $g = T_1 + T_2$ by integrating over the transmission eigenvalue distribution (2.5). The result, plotted in Fig. 2.4, has a singularity at $g = 1$, in the form of a divergence in the CRE and a cusp in the T-CRE. It is entirely different from the distribution in the single-channel case (see Fig. 2.2). How to reach the single-channel limit in the CRE and T-CRE using topological phases of matter is described in Sec. 2.5.

2.4.2 Large number of channels

In the limit $N_1, N_2 \gg 1$ of a large number of channels the distribution of the thermal conductance is a narrow Gaussian. We consider first the average and then the variance of this distribution.

The average conductance can be calculated by integrating over the eigenvalue density $\rho(T)$ of Sec. 2.3.2. We write the average of the dimensionless thermal conductance $g = G/dG_0$ as $\langle g \rangle = g_0 + \delta g$, where g_0 is the leading order term for large N_1, N_2 and δg is the first correction.

From Eqs. (2.7)–(2.9) we obtain

$$g_0 = \frac{N_1 N_2}{N_1 + N_2}, \tag{2.10}$$

$$\delta g = \frac{1}{\beta}(\beta - 2 - \gamma)\frac{N_1 N_2}{(N_1 + N_2)^2}. \tag{2.11}$$

The result (2.11) for δg in the zero-dimensional regime of a quantum dot has the same dependence on the symmetry indices as in the one-dimensional wire geometry studied by Brouwer et al [24].

Filling in the values of β, γ, and d in the four superconducting ensembles from Table 2.2, we see that (for $N_1 = N_2$)

$$\delta G = \begin{cases} 0 & \text{in the CRE and CQE,} \\ -G_0/2 & \text{in the T-CQE,} \\ G_0/4 & \text{in the T-CRE.} \end{cases} \tag{2.12}$$

This is fully analogous to the weak (anti)localization effect for the electrical conductance (with $G_0 = e^2/h$) in the non-superconducting ensembles [4]. Without time-reversal symmetry (in the CRE, CQE, and CUE) there is no effect ($\delta G = 0$), with both time-reversal and spin-rotation symmetry (in the T-CQE and COE) there is weak localization ($\delta G < 0$) and with time-reversal symmetry but no spin-rotation symmetry (in the T-CRE and CSE) there is weak antilocalization ($\delta G > 0$).

Turning now to the variance, we address the thermal analogue of universal conductance fluctuations. It is a central result of RMT[4] that the Gaussian distribution of g has a variance of order unity in the large N-limit, determined entirely by the eigenvalue repulsion factor $\prod_{i<j} |T_i - T_j|^\beta$ in the probability distribution (2.5). The γ-dependent factors plays no role. The result of the Dyson ensembles [9, 10],

$$\mathrm{Var}\, g = \frac{2(N_1 N_2)^2}{\beta(N_1 + N_2)^4}, \tag{2.13}$$

therefore still applies in the Altland-Zirnbauer ensembles.

For $N_1 = N_2$ we find the variance of the thermal conductance $\mathrm{Var}\, G = G_0^2/p$ with $p = 8, 4, 2, 1$ in, respectively, the CRE, T-CRE, CQE, T-CQE. Breaking of time-reversal symmetry thus reduces the variance of the thermal conductance in the superconducting ensembles by a factor of two, while breaking of spin-rotation symmetry reduces it by a factor of four. This is fully analogous to the electrical conductance in the non-superconducting ensembles.

2.4.3 Arbitrary number of channels

While the results from the previous subsection for the average and variance of the thermal conductance hold in the limit of a large number of channels, it is also possible to derive exact results for arbitrary N_1, N_2. Following the method described in Ref. 12, the moments of g can be evaluated using the Selberg integral [8]. We find

$$\langle g \rangle = \frac{N_1 N_2}{N_t + \xi}, \tag{2.14}$$

$$\mathrm{Var}\, g = \frac{2N_1 N_2 (N_1 + \xi)(N_2 + \xi)}{\beta (N_t - 1 + \xi)(N_t + \xi)^2 (N_t + \xi + 2/\beta)}, \tag{2.15}$$

where we abbreviated $N_t = N_1 + N_2$ and $\xi = (2 - \beta + \gamma)/\beta$. One readily checks that the large-N limits (2.10), (2.11), and (2.13) are consistent with Eqs. (2.14) and (2.15).

2.5 How to reach the single-channel limit using topological phases

As explained in Sec. 2.4.1, the single-channel distribution (2.2) of the thermal conductance can only be realized in an Andreev quantum dot in two of the four superconducting ensembles: CQE and T-CQE. The minimal channel number in the CRE and T-CRE is two, with an entirely different conductance distribution (compare Figs. 2.2 and 2.4). Here we show how this fermion doubling can be avoided using topological insulators or superconductors.

Consider first the CRE. To have just a single nonzero transmission eigenvalue we need incoming and outgoing modes that contain only half the degrees of freedom of spin-polarized electrons. These so-called Majorana modes propagate along the edge of a two-dimensional spin-polarized-triplet, $p_x \pm ip_y$-wave superconductor [26, 33], Following Ref. 32, we consider the scattering geometry shown in Fig. 2.5. The role of the quantum dot is played by a disordered domain wall between p-wave superconductors of opposite chirality. The system has two incoming and two outgoing Majorana modes, with a 2×2 scattering matrix in the CRE. The thermal conductance between the two domains has the single-channel distribution (2.2) (with $\beta = 1$, $\gamma = -1$).

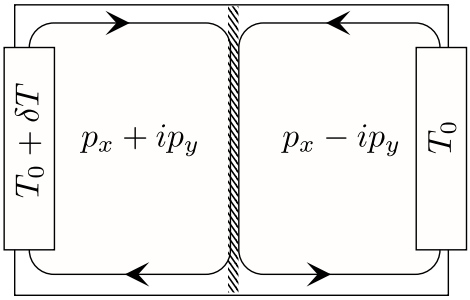

Figure 2.5. Realization of single-channel transmission in the CRE, following Ref. 32. The arrows indicate the direction of propagation of chiral Majorana modes at the edges of a $p_x \pm ip_y$-wave superconductor. The shaded strip at the center represents a disordered boundary between two domains of opposite chirality. The thermal conductance is measured between two reservoirs at a temperature difference δT, and has the single-channel distribution (2.2) (with $\beta = 1$, $\gamma = -1$).

We now turn to the T-CRE. For a single two-fold degenerate transmission eigenvalue we need a 4×4 scattering matrix. Time-reversal invariant scattering in this single-channel limit can be achieved if one uses *helical* Majorana modes (propagating in both directions) instead of *chiral* Majorana modes (propagating in a single direction only). These can be realized using s-wave superconductors deposited on the two-dimensional conducting surface of a three-dimensional topological insulator [34].

The scattering geometry is illustrated in Fig. 2.6. The helical Majorana modes propagate along a channel with superconducting boundaries having a phase difference of π (order parameter $\pm\Delta_0$). Two normal-metal contacts at a temperature difference δT inject quasiparticles via a pair of these modes into a region with chaotic scattering (provided by irregularly shaped boundaries or by disorder). The π phase difference of the superconductors that form the boundaries of the quantum dot also ensures that there is no excitation gap in that region. There are four incoming and four outgoing Majorana modes, so the scattering matrix has dimension 4×4 and the thermal conductance has the single-channel T-CRE distribution (2.2) (with $\beta = 2$, $\gamma = -1$).

The geometry of Fig. 2.6 also provides an alternative way to reach the single-channel limit in the CRE. One then needs to replace the two superconducting islands having order parameter $-\Delta_0$ by ferromagnetic

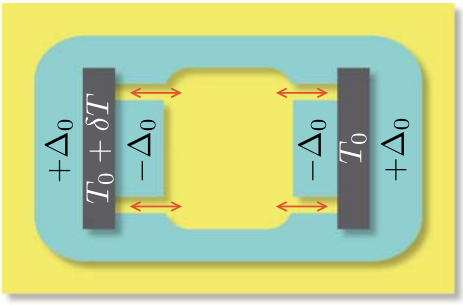

Figure 2.6. Realization of single-channel transmission in the T-CRE. The conducting surface of a topological insulator is partially covered by an s-wave superconductor, with order parameter $\pm\Delta_0$. Two contacts at temperature difference δT inject quasiparticles via two pairs of helical Majorana modes (indicated by arrows). For chaotic scattering in the central region, the thermal conductance is given by the single-channel distribution (2.2) (with $\beta = 2$, $\gamma = -1$).

insulators. The Majorana modes transform from helical to chiral [34] and one has essentially the same scattering geometry as in Fig. 2.5 — but with s-wave rather than p-wave superconductors.

2.6 Conclusion

In conclusion, we have obtained the distribution of transmission eigenvalues for low-energy chaotic scattering in the four superconducting ensembles. From this distribution all moments of the thermal conductance of an Andreev quantum dot can be calculated. In the limit of a large number of scattering channels the phenomena of weak (anti)-localization and mesoscopic fluctuations are analogous to those for the electrical conductance in the non-superconducting ensembles. The opposite single-channel limit, however, shows striking differences. Most notably, in the absence of time-reversal symmetry, the thermal conductance distribution is either peaked or suppressed at minimal and maximal conductance, while the corresponding distribution of the electrical conductance is completely uniform.

While Andreev quantum dots with multiple scattering channels can be realized in a two-dimensional electron gas with s-wave superconductors, the single-channel limit is out of reach in these systems in the absence of spin-rotation symmetry because of a fermion doubling prob-

lem. We have shown how Majorana modes at the interface between different topological phases can be used to overcome this problem.

In closing we point to the possibility to realize the four superconducting ensembles in graphene, where a strong proximity effect to *s*-wave superconductors has been demonstrated [35]. An Andreev quantum dot in graphene could be created using superconducting boundaries [36] ,as in Fig. 2.6. Since spin-orbit coupling is ineffective in graphene, only the two ensembles which preserve spin-rotation symmetry (CQE and T-CQE) are accessible in principle. However, if intervalley scattering is sufficiently weak (on the time scale set by the dwell time in the quantum dot), then the sublattice degree of freedom can play the role of the electron spin. This pseudospin is strongly coupled to the orbit, so one can then access the two ensembles with broken spin-rotation symmetry (CRE and T-CRE).

It is an interesting question to ask whether the single-channel limit might be reachable in graphene. For the CQE and T-CQE we need strong intervalley scattering, to remove the valley degeneracy. For the T-CRE we need weak intervalley scattering, and could use the very same setup as in Fig. 2.6. One can then do without a topological insulator, because the helical Majorana modes exist also in graphene at the interface between superconductors with a π phase difference [37]. For the CRE, however, weak intervalley scattering is not enough. We would also need to convert the helical Majorana mode into a chiral mode, which we do not know how to achieve without a topological phase.

Appendix 2.A Calculation of the transmission eigenvalue distribution

We briefly outline how to obtain the distribution (2.5) of the transmission eigenvalues from the invariant measure. (For a more detailed presentation of this type of calculation we refer to a textbook [38]). One goes through the following steps. The polar decomposition of S provides us with a parametrization in terms of the transmission eigenvalues T_i and angular parameters p_i. We express the invariant measure $d\mu(S)$ in terms of these parameters via the metric tensor m: $d\mu(S) = \sqrt{\det m}\prod_i dx_i$, where $\{x_i\}$ denotes the full set of parameters $\{T_i, p_i\}$ and m is defined by $\mathrm{Tr}\,(dS^\dagger dS) = \sum_{ij} m_{ij} dx_i dx_j$. Upon integration over the p_i's we obtain the required distribution $P(\{T_i\})$.

Starting from the first step, the polar decomposition reads

$$S = \begin{pmatrix} U_1 & 0 \\ 0 & U_2 \end{pmatrix} \begin{pmatrix} \sqrt{1-\Lambda\Lambda^T} & i\Lambda \\ i\Lambda^T & \sqrt{1-\Lambda^T\Lambda} \end{pmatrix} \begin{pmatrix} V_1^\dagger & 0 \\ 0 & V_2^\dagger \end{pmatrix}, \tag{2.16}$$

where the $N_1 \times N_2$ matrix Λ has elements $\Lambda_{jk} = \sqrt{T_j}\delta_{jk}$. Referring to Table 2.2, the transmission eigenvalues have a twofold electron-hole degeneracy in classes C and CI, as a direct consequence of the fact that the matrix elements can be represented by (real) quaternions. In addition, there is a twofold spin degeneracy because spin-rotation symmetry is preserved. In class DIII, the presence of time-reversal symmetry produces a twofold Kramers degeneracy of the transmission eigenvalues. (We focus on the situation where N_1 and N_2 are even.) The unitary matrices U_n and V_n are orthogonal in classes D and DIII and symplectic in classes C and CI. They are independent in classes D and C. In class DIII one has $V_n^\dagger = \sigma_2 U_n^T \sigma_2$, while in class CI $V_n^\dagger = U_n^*$.

The following steps are straightforward, apart from one complication. In the polar decomposition, the set of T_i's and the matrices U_n and V_n introduce more parameters than the number of independent degrees of freedom of the scattering matrix. The metric tensor, however, is defined through the derivatives of S with respect to the set of its independent parameters. Keeping $\{T_i\}$ in our parametrization, we define the angular parameters $\{p_i\}$ as independent combinations of the matrix elements of $\delta U_n = U_n^\dagger dU_n$ and $\delta V_n = V_n^\dagger dV_n$. In this way, the subsequent integration over these degrees of freedom does not involve dependencies

on the T_i's. The integration over these parameters thus only produces an irrelevant normalization constant and need not be carried out explicitly.

Bibliography

[1] S. Datta, *Electronic Transport in Mesoscopic Systems*, (Cambridge University Press, Cambridge, 1995).

[2] H. van Houten and C. W. J. Beenakker, Phys. Today **49** (7), 22 (1996).

[3] Y. Imry and R. Landauer, Rev. Mod. Phys. **71**, S306 (1999).

[4] C. W. J. Beenakker, Rev. Mod. Phys. **69**, 731 (1997).

[5] T. Guhr, A. Müller-Groeling, and H. A. Weidenmüller, Phys. Rep. **299**, 189 (1998).

[6] Y. Alhassid, Rev. Mod. Phys. **72**, 895 (2000).

[7] F. J. Dyson, J. Math. Phys. **3**, 140 (1962).

[8] M. L. Mehta, *Random Matrices* (Academic Press, New York, 1991).

[9] H. U. Baranger and P. A. Mello, Phys. Rev. Lett. **73**, 142 (1994).

[10] R. A. Jalabert, J.-L. Pichard, and C. W. J. Beenakker, Europhys. Lett. **27**, 255 (1994).

[11] C. W. J. Beenakker, The Oxford Handbook of Random Matrix Theory, edited by G. Akemann, J. Baik, and P. Di Francesco, Oxford University Press, 723–758 (2011), arXiv:0904.1432.

[12] D. V. Savin and H.-J. Sommers, Phys. Rev. B **73**, 081307 (2006).

[13] B. A. Khoruzhenko, D. V. Savin, and H.-J. Sommers, Phys. Rev. B **80**, 125301 (2009).

[14] V. A. Osipov and E. Kanzieper, Phys. Rev. Lett. **101**, 176804 (2008).

[15] A. Altland and M. R. Zirnbauer, Phys. Rev. B **55**, 1142 (1997).

[16] P. Heinzner, A. H. Huckleberry, and M. R. Zirnbauer, Commun. Math. Phys. **257**, 725 (2005).

[17] S. Ryu, A. P. Schnyder, A. Furusaki, and A. W. W. Ludwig, New J. Phys. **12**, 065010 (2010).

[18] M. R. Zirnbauer, The Oxford Handbook of Random Matrix Theory, edited by G. Akemann, J. Baik, and P. Di Francesco, Oxford University Press (2011), arXiv:1001.0722.

[19] M. Caselle, Mod. Phys. Lett. B **10**, 681 (1996).

[20] The parameters β and $\gamma + 1$ are the socalled root multiplicities of the symmetry class, see M. Caselle and U. Magnea, Phys. Rep. **394**, 41 (2004).

[21] T. Senthil and M. P. A. Fisher, Phys. Rev. B **61**, 9690 (2000).

[22] A. Vishwanath, Phys. Rev. Lett. **87**, 217004 (2001).

[23] J. T. Chalker, N. Read, V. Kagalovsky, B. Horovitz, Y. Avishai, and A. W. W. Ludwig, Phys. Rev. B **65**, 012506 (2002).

[24] P. W. Brouwer, A. Furusaki, I. A. Gruzberg, and C. Mudry, Phys. Rev. Lett. **85**, 1064 (2000).

[25] M. Titov, P. W. Brouwer, A. Furusaki, and C. Mudry, Phys. Rev. B **63**, 235318 (2001).

[26] G. E. Volovik, *The Universe in a Helium Droplet* (Clarendon Press, Oxford, 2003).

[27] X.-L. Qi and S.-C. Zhang, Phys. Today **63** (1), 33 (2010).

[28] M. Z. Hasan and C. L. Kane, Rev. Mod. Phys. **82**, 3045 (2010) .

[29] U. Sivan and Y. Imry, Phys. Rev. B **33**, 551 (1986).

[30] C. W. J. Beenakker, Lect. Notes Phys. **667**, 131 (2005).

[31] B. Béri, Phys. Rev. B **79**, 214506 (2009).

[32] I. Serban, B. Béri, A. R. Akhmerov, and C. W. J. Beenakker, Phys. Rev. Lett. **104**, 147001 (2010).

[33] C. Kallin and A. J. Berlinsky, J. Phys. Cond. Matter **21**, 164210 (2009).

[34] L. Fu and C. L. Kane, Phys. Rev. Lett. **100**, 096407 (2008).

[35] H. B. Heersche, P. Jarillo-Herrero, J. B. Oostinga, L. M. K. Vandersypen, and A. F. Morpurgo, Nature **446**, 56 (2007).

[36] J. Cserti, I. Hagymási, and A. Kormányos, Phys. Rev. B **80**, 073404 (2009).

[37] M. Titov, A. Ossipov, and C. W. J. Beenakker, Phys. Rev. B **75**, 045417 (2007).

[38] P. J. Forrester, *Log-Gases and Random Matrices* (Princeton University Press, Princeton, 2010).

Chapter 3

Random-matrix theory of Andreev reflection from a topological superconductor

3.1 Introduction

The random-matrix theory (RMT) of quantum transport studies the statistical distribution of phase-coherent transport properties in an ensemble of random scattering matrices. The theory finds a major application in the context of chaotic scattering, because then the ensemble is fully specified by fundamental symmetries — without requiring microscopic input [1]. Since scattering phase shifts for chaotic scattering are uniformly distributed on the unit circle, such ensembles are called "circular", following Dyson who first introduced these ensembles in a mathematical context [2]. The circular ensembles have been successful in describing experiments on low-temperature electrical and thermal conduction in quantum dots, which are confined geometries connected by point contacts to metallic or superconducting electrodes. For a recent overview of the field we refer to several chapters of a forthcoming Handbook [3].

While metallic quantum dots are characterized by the three circular ensembles introduced originally by Dyson [2], superconducting quantum dots are described by four different ensembles discovered by Altland and Zirnbauer [4]. The classification of the superconducting ensembles is based on the presence or absence of time-reversal and spin-

Symmetry class	D	DIII	C	CI
Ensemble name	CRE	T-CRE	CQE	T-CQE
Particle-hole symmetry	$r_{ee} = r_{hh}^*$, $r_{eh} = r_{he}^*$		$r_{ee} = r_{hh}^*$, $r_{eh} = -r_{he}^*$	
Time-reversal symmetry	$\times$	$r = \Sigma_y r^{\mathrm{T}} \Sigma_y$	$\times$	$r = r^{\mathrm{T}}$
Spin-rotation symmetry	$\times$	$\times$	$\checkmark$	$\checkmark$
topological quantum number Q	$\mathrm{Det}\, r$	$\mathrm{Pf}\, i\Sigma_y r$	$\times$	$\times$
degeneracy of $R_n \neq 0, 1$	2	2	2	2
degeneracy of $R_n = 0, 1$	1	2	2	2

Table 3.1. Classification of the symmetries of the reflection matrix r for a normal-metal–superconductor junction. See Sec. 3.2 for explanations.

rotation symmetry, as summarized in Table 3.1. The symmetry classes are called D, DIII, C, and CI, in a notation which originates from differential geometry [4]. The corresponding circular ensembles, in the nomenclature of Ref. 5, are the circular real (CRE) and circular quaternion (CQE) ensembles in class D and C, respectively, and their time-reversal invariant restrictions (T-CRE and T-CQE) in class DIII and CI.

In a remarkable recent development, it was found that some of these symmetry classes divide into disjunct subclasses, characterized by a topological quantum number [6–9]. For a quantum dot connected to a superconducting wire, such as shown in Fig. 3.1, the topological quantum number $Q = -1$ or $+1$ depending on whether or not the quantum dot has a bound state at zero excitation energy. (The state is only quasi-bound if the quantum dot is also connected by a point contact to a normal-metal electrode.) Because of particle-hole symmetry, such a fermionic excitation is equal to its own antiparticle, so it is a Majorana fermion. There is now an active search for the Majorana bound states predicted to appear at the ends of superconducting wires without spin-rotation symmetry [10–15].

The RMT of the four superconducting circular ensembles was developed for the quasiparticle transmission eigenvalues in Ref. 5, and applied to the thermal conductance. The probability distribution of this transport property does not depend on the topological quantum number, so it was not needed in that study to distinguish the topologically nontrivial ensemble (with a Majorana bound state) from the topologically trivial ensemble (without such a state).

The electrical conductance G, in contrast, can probe the presence or absence of the Majorana bound state through resonant Andreev re-

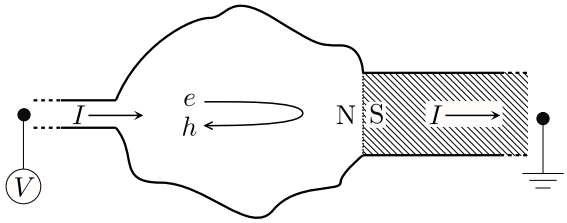

Figure 3.1. Quantum dot with an interface between a normal metal (N) and a superconductor (S, shaded region). Andreev reflection at the NS interface converts a normal current (carried by electron and hole excitations e and h) into a supercurrent (carried by Cooper pairs). The conductance G is the ratio of the current I into the grounded superconductor and the voltage V applied to the quantum dot via an N-mode point contact to a normal metal electrode (narrow opening at the left). The system is in a topologically nontrivial state if it supports a quasi-bound state at the Fermi level. This is possible if spin-rotation symmetry is broken by spin-orbit coupling. In the configuration shown in the figure (with a single NS interface), time-reversal symmetry should be broken to prevent the opening of an excitation gap in the quantum dot. In the presence of time-reversal symmetry a second NS interface, with a π phase difference, can be used to close the gap.

flection [16, 17]. This applies also to a quasi-bound state [18, 19], so even if the N-mode point contact to the normal metal has a conductance which is not small compared to e^2/h — although the effect of Q on G diminishes with increasing N. As we will show in this chapter, the Q-dependence of the conductance distribution $P(G)$ in the circular ensembles is nonperturbative in N: Cumulants of order p are identical in the topologically trivial and nontrivial phases for $p < N$ $(N/2)$ in the absence (presence) of time-reversal symmetry.

We derive this nonperturbative result by exactly computing (in Sec. 3.3 and App. 3.A) the joint probability distribution $P(\{R_n\})$ of the Andreev reflection eigenvalues $R_1, R_2, \ldots R_N$ (eigenvalues of the product $r_{he}^\dagger r_{he}$ of the matrix r_{he} of Andreev reflection amplitudes). This probability distribution was only known previously for one of the ensembles (CQE) without a topological phase [20], while here we calculate it for all four superconducting ensembles, including the possibility of a topologically nontrivial phase.

The distribution of the electrical conductance $G \propto \sum_n R_n$ follows on integration over the R_n's (Sec. 3.4). For small N we obtain a closed-form expression for $P(G)$ in the two cases $Q = \pm 1$, and we demonstrate

that, on increasing N, first the average becomes the same, followed by variance, skewness, kurtosis, etc. A proof for arbitrary N of the Q-independence of low-order cumulants is given in App. 3.B.

We conclude in Sec. 3.5 with a comparison of the analytical predictions from RMT with a computer simulation of a system that is of current experimental interest (a disordered semiconductor wire on an s-wave superconducting substrate, with Rashba spin-orbit coupling and Zeeman spin splitting) [10, 11].

3.2 Andreev reflection eigenvalues

Andreev reflection of electrons injected through a point contact towards a normal-metal–superconductor (NS) interface is described by the $N \times N$ subblock r_{he} of the $2N \times 2N$ reflection matrix r,

$$r = \begin{pmatrix} r_{ee} & r_{eh} \\ r_{he} & r_{hh} \end{pmatrix}. \tag{3.1}$$

The labels e and h refer to electron and hole excitations in the normal-metal point contact, each of which can be in one of N modes. We allow for spin-orbit coupling, so N counts both orbital and spin degrees of freedom. The Andreev reflection eigenvalues R_n ($n = 1, 2, \ldots N$) are the eigenvalues of the Hermitian matrix product $r_{he}^\dagger r_{he}$.

At excitation energies ε below the superconducting gap Δ there is no transmission of excitations through the superconductor (assuming that it is large compared to the penetration depth $\xi_0 = \hbar v_F/\Delta$). The reflection matrix is then a unitary matrix, $r^\dagger = r^{-1}$. An electrical current I can still enter into the superconductor, driven by a voltage difference V with the normal metal. The electrical conductance $G = I/V$ is fully determined by the Andreev reflection eigenvalues [21],

$$G/G_0 = N - \mathrm{Tr}\, r_{ee}^\dagger r_{ee} + \mathrm{Tr}\, r_{he}^\dagger r_{he} = 2\sum_{n=1}^{N} R_n. \tag{3.2}$$

The conductance quantum is $G_0 = e^2/h$ and the factor of two accounts for the fact that charge is added to the superconductor as Cooper pairs of charge $2e$. (Spin is counted in the sum over n.)

The relation (3.2) holds in the limit of zero voltage and zero temperature, when the reflection matrix is evaluated at the Fermi level ($\varepsilon \to 0$).

The subblocks in Eq. (3.1) are then related by particle-hole symmetry,

$$r_{hh} = r_{ee}^*, \quad r_{eh} = r_{he}^*. \tag{3.3}$$

Time-reversal symmetry imposes a further constraint on the reflection matrix,

$$r = \Sigma_y r^{\mathrm{T}} \Sigma_y, \tag{3.4}$$

with $\Sigma_y = \sigma_y \oplus \sigma_y \oplus \cdots \oplus \sigma_y$ and σ_y a 2×2 Pauli matrix. (The superscript T denotes the transpose.)

The Andreev reflection eigenvalues are all twofold degenerate in the presence of time-reversal symmetry. This is the usual Kramers degeneracy, which follows directly from the fact that $\Sigma_y r$ is an antisymmetric matrix [$\Sigma_y r = -(\Sigma_y r)^{\mathrm{T}}$] when Eq. (3.4) holds [22].

Remarkably enough, a twofold degeneracy persists even if time-reversal symmetry is broken. More precisely, as discovered by Béri [23], if R_n is not degenerate then it must equal 0 or 1. This follows from the antisymmetry of the matrix $r_{he}^{\mathrm{T}} r_{ee}$, which is required by particle-hole symmetry and unitarity irrespective of whether time-reversal symmetry is present or not. The degeneracy of the Andreev reflection eigenvalues $R_n \neq 0, 1$ is remarkable because the eigenvalues of the Hamiltonian are not degenerate in the absence of time-reversal symmetry. To distinguish it from the Kramers degeneracy, we propose the name "Béri degeneracy".

The determinant of r is real due to particle-hole symmetry, and therefore equal to either $+1$ or -1 due to unitarity. The topological quantum number $Q = \mathrm{Det}\, r$ distinguishes the topologically trivial phase ($Q = 1$) from the topologically nontrivial phase ($Q = -1$) [24–26]. This quantum number is ineffective in the presence of time-reversal symmetry, when Kramers degeneracy enforces $\mathrm{Det}\, r = 1$. In that case the Pfaffian (the square root of the determinant of an antisymmetric matrix) can be used instead of the determinant to identify the topologically nontrivial phase [27]: $Q = \mathrm{Pf}\, i\Sigma_y r$ equals $+1$ or -1 depending on whether the superconductor is topologically trivial or not.

A topologically nontrivial superconductor has a (possibly degenerate) bound state at $\varepsilon = 0$, consisting of an equal-weight superposition of electrons and holes from the same spin band. It is the π phase shift upon reflection from such a Majorana bound state which is responsible for the minus sign in the topological quantum number [26].

These properties of the reflection matrix in the absence of spin-rotation symmetry are summarized in Table 3.1. For completeness, we also include in that table the case when there is no spin-orbit coupling. In that case it is sufficient to consider only the orbital degree of freedom, with a two-fold spin degeneracy of all R_n's. The conditions for particle-hole symmetry and time-reversal symmetry are then both different from Eqs. (3.3) and (3.4), given respectively by

$$r_{hh} = r_{ee}^*, \quad r_{eh} = -r_{he}^*, \tag{3.5}$$

$$r = r^{\mathrm{T}}. \tag{3.6}$$

As a consequence, the determinant of r is now always $+1$, while the Pfaffian does not exist (for want of an antisymmetric matrix). Without spin-orbit coupling Andreev reflection exclusively couples electrons and holes from opposite spin bands, which prevents the formation of a Majorana bound state at the NS interface.

3.3 Random-matrix theory

In this section we calculate the distribution of the Andreev reflection eigenvalues, which we then apply to electrical conduction in the next section. For each symmetry class we first determine the polar decomposition of r in terms of the R_n's. The resulting invariant measure $d\mu(r) \propto P(\{R_n\}) \prod_n dR_n$ then gives the probability distribution $P(\{R_n\})$ of the Andreev reflection eigenvalues in the corresponding circular ensemble.

3.3.1 Class D, ensemble CRE

In the absence of time-reversal and spin-rotation symmetry the scattering matrix has the polar decomposition

$$r = \begin{pmatrix} U & 0 \\ 0 & U^* \end{pmatrix} \begin{pmatrix} \Gamma & -i\Lambda \\ i\Lambda & \Gamma \end{pmatrix} \begin{pmatrix} V^\dagger & 0 \\ 0 & V^{\mathrm{T}} \end{pmatrix}. \tag{3.7}$$

The $N \times N$ matrices U, V are unitary and the $N \times N$ matrices Λ and Γ are real, to satisfy the particle-hole symmetry condition (3.3). Unitarity of r requires, in addition to $\Gamma^{\mathrm{T}}\Gamma + \Lambda^{\mathrm{T}}\Lambda = 1$, that $\Lambda^{\mathrm{T}}\Gamma = -\Gamma^{\mathrm{T}}\Lambda$ is antisymmetric. As derived in Ref. 23, the matrices Λ and Γ must therefore have a 2×2 block diagonal structure.

For $N = 2M$ even and $Q = 1$ one has $\Lambda = \Lambda_M$, $\Gamma = \Gamma_M$ with

$$\Lambda_M = \bigoplus_{n=1}^{M} \begin{pmatrix} \sin\alpha_n & 0 \\ 0 & \sin\alpha_n \end{pmatrix} = \bigoplus_{n=1}^{M} \sigma_0 \sin\alpha_n, \tag{3.8}$$

$$\Gamma_M = \bigoplus_{n=1}^{M} \begin{pmatrix} 0 & \cos\alpha_n \\ -\cos\alpha_n & 0 \end{pmatrix} = \bigoplus_{n=1}^{M} i\sigma_y \cos\alpha_n. \tag{3.9}$$

The 2×2 Pauli matrices are $\sigma_x, \sigma_y, \sigma_z$ (with σ_0 the 2×2 unit matrix). The real angles $\alpha_n \in (0, 2\pi)$ determine the Andreev reflection eigenvalues $R_n = \sin^2\alpha_n$. These are all twofold degenerate.

The parameterization derived in Ref. 23 has $\Lambda_M \propto i\sigma_y$ and $\Gamma_M \propto \sigma_0$. The present, equivalent, form is chosen because it is more easily extended to symmetry class DIII (where an additional symmetry condition applies). For the same reason, we parameterize the diagonal entries in terms of the angles α_n rather than in terms of $\sqrt{R_n}$ and $\sqrt{1-R_n}$. (The sign of the terms $\sin\alpha_n$, $\cos\alpha_n$ cannot be fixed in class DIII.)

To check that the polar decomposition (3.7)–(3.9) indeed gives $\mathrm{Det}\, r = 1$, one can use the identities $\mathrm{Det}\, AB = (\mathrm{Det}\, A)(\mathrm{Det}\, B)$ and

$$\mathrm{Det} \begin{pmatrix} A & B \\ C & D \end{pmatrix} = \mathrm{Det}\,(AD - ACA^{-1}B). \tag{3.10}$$

For $N = 2M$ even and $Q = -1$ one has

$$\Lambda = \Lambda_{M-1} \oplus \begin{pmatrix} 0 & 0 \\ 0 & 1 \end{pmatrix}, \quad \Gamma = \Gamma_{M-1} \oplus \begin{pmatrix} 1 & 0 \\ 0 & 0 \end{pmatrix}, \tag{3.11}$$

so in addition to $M-1$ two-fold degenerate eigenvalues $R_1, R_2, \ldots R_{M-1}$ there is one nondegenerate eigenvalue equal to 0 and one nondegenerate eigenvalue equal to 1. It is this unit Andreev reflection eigenvalue which contributes a factor -1 to $\mathrm{Det}\, r$.

For $N = 2M+1$ odd there are M two-fold degenerate eigenvalues $R_1, R_2, \ldots R_M$ plus one nondegenerate eigenvalue equal to $q = (1 - Q)/2$,

$$\Lambda = \Lambda_M \oplus (q), \quad \Gamma = \Gamma_M \oplus (1-q). \tag{3.12}$$

The nondegenerate eigenvalue equals 1 in the topologically nontrivial phase and 0 otherwise. Again, it is the unit Andreev reflection eigenvalue which gives $\mathrm{Det}\, r = -1$.

The calculation of the invariant measure from these polar decompositions is outlined in App. 3.A. The resulting probability distributions of the twofold degenerate Andreev reflection eigenvalues in the CRE are

$$P(\{R_n\}) \propto \prod_{i<j=1}^{M} (R_i - R_j)^4, \quad \text{if } N = 2M \text{ and } Q = 1, \tag{3.13}$$

$$P(\{R_n\}) \propto \prod_{i<j=1}^{M-1} (R_i - R_j)^4 \prod_{k=1}^{M-1} R_k^2 (1 - R_k)^2, \quad \text{if } N = 2M \text{ and } Q = -1, \tag{3.14}$$

$$P(\{R_n\}) \propto \prod_{i<j=1}^{M} (R_i - R_j)^4 \prod_{k=1}^{M} [R_k - \tfrac{1}{2}(1 - Q)]^2, \quad \text{if } N = 2M + 1. \tag{3.15}$$

The degenerate Andreev reflection eigenvalues repel each other with the fourth power of their separation. In addition there is a repulsion with the second power of the separation to each of the nondegenerate eigenvalues, pinned at 0 or 1.

3.3.2 Class DIII, ensemble T-CRE

In the presence of time-reversal symmetry the scattering matrix should also satisfy the condition (3.4), which implies that $i\Sigma_y r$ is antisymmetric. The polar decomposition which respects this symmetry condition (as well as the condition (3.3) for particle-hole symmetry) is

$$i\Sigma_y r = \begin{pmatrix} \Omega & 0 \\ 0 & \Omega^* \end{pmatrix} \begin{pmatrix} \Gamma & -i\Lambda \\ i\Lambda & \Gamma \end{pmatrix} \begin{pmatrix} \Omega^{\mathrm{T}} & 0 \\ 0 & \Omega^\dagger \end{pmatrix}, \tag{3.16}$$

with Ω an $N \times N$ unitary matrix. Unitarity still requires that $\Lambda^{\mathrm{T}}\Gamma$ is antisymmetric, while time-reversal symmetry requires $\Gamma^{\mathrm{T}} = -\Gamma$, $\Lambda^{\mathrm{T}} = \Lambda$.

The number of channels $N = 2M$ is even, with M the number of channels per spin. Each reflection eigenvalue has a two-fold degeneracy, including those equal to 0 or 1. This Kramers degeneracy due to time-reversal symmetry [22] in class DIII *replaces* the Béri degeneracy due to electron-hole symmetry [23] in class D — it is not an additional

degeneracy. The topological quantum number [27] $Q = \mathrm{Pf}\, i\Sigma_y r$ can be calculated using the identity

$$\mathrm{Pf}\begin{pmatrix} 0 & a & b & c \\ -a & 0 & d & e \\ -b & -d & 0 & f \\ -c & -e & -f & 0 \end{pmatrix} = af - be + cd, \tag{3.17}$$

for scalars a, b, c, d, e, f, and also the formulas $\mathrm{Pf}\, XYX^{\mathrm{T}} = (\mathrm{Det}\, X)(\mathrm{Pf}\, Y)$, $\mathrm{Pf} \bigoplus_n Y_n = \prod_n \mathrm{Pf}\, Y_n$ (valid for arbitrary square matrices X and antisymmetric matrices Y, Y_n).

For $Q = 1$ we take $\Lambda = \Lambda_M$ and $\Gamma = \Gamma_M$ from Eqs. (3.8) and (3.9). The Pfaffian of the matrix (3.16) is always $+1$, so this polar decomposition describes the topologically trivial phase. In order to reach the topologically nontrivial phase, we include a twofold degenerate eigenvalue equal to unity, but with a σ_z matrix rather than a σ_0 matrix: $\Lambda = \Lambda_{M-1} \oplus \mathrm{diag}\,(1, -1)$, $\Gamma = \Gamma_{M-1} \oplus \mathrm{diag}\,(0, 0)$. Then the Pfaffian is -1.

As derived in App. 3.A, the distribution of the M degenerate Andreev reflection eigenvalues in the T-CRE is given most compactly in terms of the variables $\xi_n = \sin \alpha_n \in (-1, 1)$ (with $R_n = \xi_n^2$). For $Q = 1$ the result is

$$P(\{\xi_n\}) \propto \prod_{i<j=1}^{M} (\xi_i - \xi_j)^4. \tag{3.18}$$

Notice that there is no repulsion of pairs of Andreev reflection eigenvalues: If $\xi_i \to -\xi_j$ then $R_i \to R_j$ and yet the probability distribution does not vanish.

For $Q = -1$ one pair of eigenvalues is pinned at $R_M = 1 \Rightarrow \xi_M = 1$. The distribution of the remaining $M - 1$ degenerate eigenvalues is

$$P(\{\xi_n\}) \propto \prod_{i<j=1}^{M-1} (\xi_i - \xi_j)^4 \prod_{k=1}^{M-1} (1 - \xi_k^2)^2. \tag{3.19}$$

While pairs of Andreev reflection eigenvalues $R_n \in (0, 1)$ in the T-CRE do not repel each other, they are repelled from the eigenvalue pinned at $R_M = 1$, with the same second power of the separation as in the CRE.

3.3.3 Class C, ensemble CQE

For completeness we also consider the two symmetry classes C and CI without a topological phase. Then spin-rotation symmetry is preserved, so it is sufficient to consider a single spin degree of freedom, say an electron in the spin-up band coupled to a hole in the spin-down band. The reflection matrix for this scattering process has dimension $2M \times 2M$, where M only counts the orbital degree of freedom. Each reflection eigenvalue has a twofold spin degeneracy.

The polar decomposition of the reflection matrix reads

$$r = \begin{pmatrix} U & 0 \\ 0 & U^* \end{pmatrix} \begin{pmatrix} \cos\boldsymbol{\alpha} & i\sin\boldsymbol{\alpha} \\ i\sin\boldsymbol{\alpha} & \cos\boldsymbol{\alpha} \end{pmatrix} \begin{pmatrix} V^\dagger & 0 \\ 0 & V^{\mathrm{T}} \end{pmatrix}, \tag{3.20}$$

as required by unitarity and the particle-hole symmetry condition (3.5). Here U, V are unitary $M \times M$ matrices and $\boldsymbol{\alpha} = \mathrm{diag}\,(\alpha_1, \alpha_2, \ldots \alpha_M)$ is the diagonal matrix of real angles that determine the reflection eigenvalues $R_n = \sin^2 \alpha_n$. As before, we might have replaced $\sin\alpha_n \mapsto \sqrt{R_n}$ and $\cos\alpha_n \mapsto \sqrt{1-R_n}$ in this polar decomposition for class C, but not when we additionally impose time-reversal symmetry (in class CI).

The factor i in Eq. (3.20) accounts for the $\pi/2$ phase shift associated with Andreev reflection of an electron into a hole from the opposite spin band. No such factor appears in the polar decomposition (3.7) in the absence of spin-rotation symmetry, because there it can be absorbed in the unitary matrices (which in that case contain both spin bands for electrons and holes).

The probability distribution of the Andreev reflection eigenvalues in the CQE was calculated previously by Khaymovich et al [20]. We find

$$P(\{R_n\}) \propto \prod_{i<j=1}^{M} |R_i - R_j|, \tag{3.21}$$

in agreement with Ref. 20 (up to an evident misprint, $\prod_{i\neq j}$ instead of $\prod_{i<j}$).

3.3.4 Class CI, ensemble T-CQE

Finally, in class CI we have the additional requirement (3.6) of time-reversal symmetry. The polar decomposition becomes

$$r = \begin{pmatrix} U & 0 \\ 0 & U^* \end{pmatrix} \begin{pmatrix} \cos\boldsymbol{\alpha} & i\sin\boldsymbol{\alpha} \\ i\sin\boldsymbol{\alpha} & \cos\boldsymbol{\alpha} \end{pmatrix} \begin{pmatrix} U^{\mathrm{T}} & 0 \\ 0 & U^\dagger \end{pmatrix}. \tag{3.22}$$

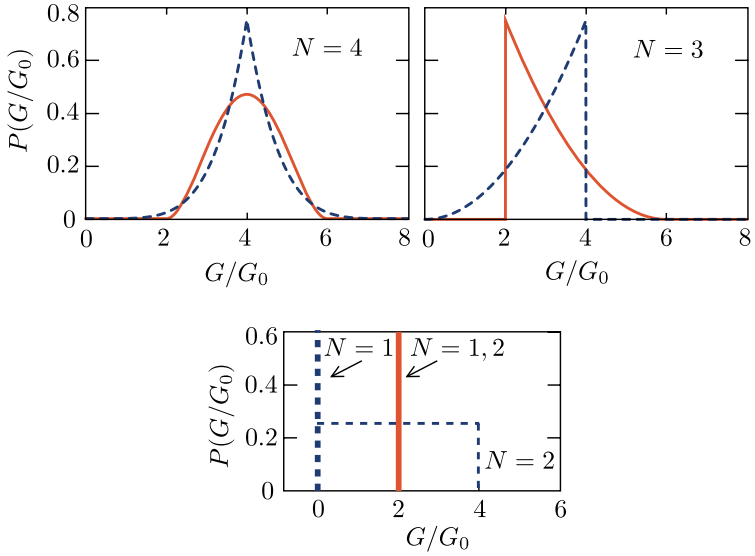

Figure 3.2. Probability distribution of the conductance in the CRE, for channel numbers $N = 1, 2, 3, 4$ and topological charges $Q = -1$ (red solid curves) and $Q = +1$ (blue dashed curves). In the lower panel the thick vertical lines indicate a delta-function distribution.

The distribution of the R_n's in the T-CQE (each doubly degenerate) is again given most compactly in terms of the variables $\xi_n = \sin\alpha_n \in (-1, 1)$ (with $R_n = \xi_n^2$). We find

$$P(\{\xi_n\}) \propto \prod_{i<j=1}^{M} |\xi_i - \xi_j|. \tag{3.23}$$

As in the T-CRE, there is no repulsion between pairs of Andreev reflection eigenvalues in the presence of time-reversal symmetry.

3.4 Dependence of conductance distributions on topological invariant

3.4.1 Broken time-reversal symmetry

From the probability distributions $P(\{R_n\})$ in Secs. 3.3.1 and 3.3.2 we readily calculate the distribution $P(G)$ of the conductance (3.2), in both

	$\langle\langle (G/G_0)^p \rangle\rangle$				
	$p=1$	$p=2$	$p=3$	$p=4$	$p=5$
$N=1$	$\mathbf{0 \vdots 2}$	$0 \vdots 0$	$0 \vdots 0$	$0 \vdots 0$	$0 \vdots 0$
$N=2$	$2 \vdots 2$	$\mathbf{\frac{4}{3} \vdots 0}$	$0 \vdots 0$	$-\frac{32}{15} \vdots 0$	$0 \vdots 0$
$N=3$	$3 \vdots 3$	$\frac{3}{5} \vdots \frac{3}{5}$	$\mathbf{-\frac{2}{5} \vdots \frac{2}{5}}$	$\frac{6}{175} \vdots \frac{6}{175}$	$\frac{24}{35} \vdots -\frac{24}{35}$
$N=4$	$4 \vdots 4$	$\frac{4}{7} \vdots \frac{4}{7}$	$0 \vdots 0$	$\mathbf{\frac{176}{735} \vdots -\frac{32}{147}}$	$0 \vdots 0$
$N=5$	$5 \vdots 5$	$\frac{5}{9} \vdots \frac{5}{9}$	$0 \vdots 0$	$\frac{10}{2079} \vdots \frac{10}{2079}$	$\mathbf{-\frac{8}{63} \vdots \frac{8}{63}}$

Table 3.2. First five cumulants ($p \leq 5$) of conductance in the CRE, calculated for number of modes $N \leq 5$ and topological quantum number Q. (The first entry in each cell is for $Q = 1$, the second entry is for $Q = -1$.) The conductance distribution depends on Q starting from the N-th cumulant (bold).

the topologically trivial and nontrivial phases. We first consider the case without time-reversal symmetry (class D, ensemble CRE). Using Eqs. (3.13)–(3.15) we obtain the distributions for the first few channel numbers $N = 1, 2, 3, 4$. The results are plotted in Fig. 3.2, and given by:

- For $N = 1$, the conductance $G/G_0 = 1 - Q$ without statistical fluctuations [23, 18].
- For $N = 2$, the conductance $G/G_0 = 2$ for $Q = -1$ without statistical fluctuations; if $Q = 1$, instead $G/G_0 = 4g$ with $P(g) = 1$.
- For $N = 3$ the conductance $G/G_0 = 1 - Q + 4g$, with $P(g) = 3(\frac{1}{2} - \frac{1}{2}Q - g)^2$.
- For $N = 4$ the conductance $G/G_0 = 2 + 4g$ if $Q = -1$, with $P(g) = 30\,g^2(1-g)^2$, while if $Q = 1$ we have $G/G_0 = 8g$ with $P(g) = 6(1 - |1 - 2g|)^5$.

In these expressions, g denotes a stochastic variable in the range $(0, 1)$.

From Fig. 3.2 we see that upon increasing N, the conductance distributions for $Q = 1$ and $Q = -1$ become more and more similar. To quantify the difference, we list in Table 3.2 the first few cumulants $\langle\langle G^p \rangle\rangle$ of $P(G)$ for several values of N. Inspection of the table brings us to propose that:

> *The cumulant of order p of the N-mode conductance in the CRE is independent of the topological charge for $p < N$.*

A proof for arbitrary N is given in App. 3.B.

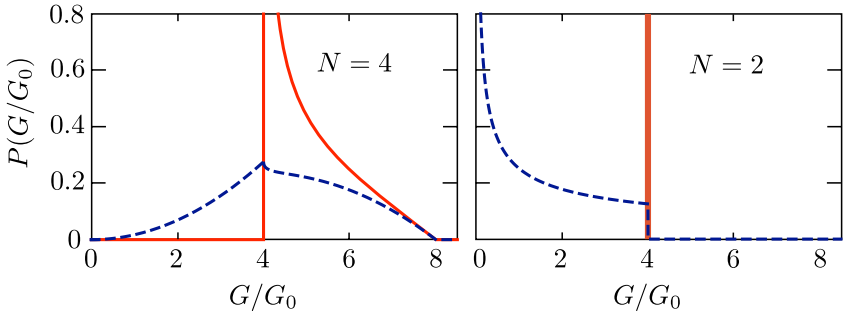

Figure 3.3. Same as Fig. 3.2, for the T-CRE.

3.4.2 Preserved time-reversal symmetry

In the presence of time-reversal symmetry (class DIII, ensemble T-CRE) we can similarly calculate the conductance distribution from Eqs. (3.18) and (3.19). For small N we find:

- For $N = 2$, the conductance $G/G_0 = 4$ without statistical fluctuations if $Q = -1$, while if $Q = 1$ we have $G/G_0 = 4g$ with $P(g) = \frac{1}{2}g^{-1/2}$.
- For $N = 4$ the conductance $G/G_0 = 4 + 4g$ if $Q = -1$, with $P(g) = \frac{15}{16}(1-g)^2 g^{-1/2}$; if $Q = 1$, instead $G/G_0 = 8g$ with $P(g)$ plotted in Fig. 3.3, upper panel. (The analytic expression is lengthy.)

The analogous theorem for the Q-independence of low-order cumulants now reads:

> *The cumulant of order p of the N-mode conductance in the T-CRE is independent of the topological charge for $p < N/2$.*

A proof for arbitrary (even) N is given also in App. 3.B.

3.4.3 Weak localization and UCF

Weak localization and universal conductance fluctuations (UCF) refer to the average and to the variance of the conductance in the large-N limit. Since the dependence on the topological charge is nonpertubative in N, these two effects cannot contain any information on whether the superconductor is in a topological phase or not. As a check, we have calculated the average $\langle G \rangle$ and the variance $\mathrm{Var}\, G = \langle G^2 \rangle - \langle G \rangle^2$ for

$N \gg 1$, directly from the probability distribution of the Andreev reflection eigenvalues. This calculation also allows us to verify a conjecture from Ref. 4 on the UCF in the presence of time-reversal symmetry. Since the calculation follows established methods in random-matrix theory [28], we only give the results.

The weak-localization correction $\delta G = G - NG_0$ to the conductance vanishes in the CRE and CQE, while $\delta G/G_0 = \frac{1}{2}, -1$ in the T-CRE and T-CQE, respectively. The UCF are given by $\operatorname{Var} G/G_0 = \frac{1}{2}, 1, 2, 4$ in the CRE, T-CRE, CQE, and T-CQE, respectively. These Q-independent results are in full agreement with Ref. 4.

All these results assume that the proximity to the superconductor does not induce an excitation gap in the quantum dot. In the CRE and CQE this is realized by the pair-breaking magnetic field. In the T-CRE and T-CQE we need a π-junction to close the gap: Two NS interfaces, coupled equally well to the quantum dot and with a π phase difference of the superconducting phase [4]. For a single NS interface in zero magnetic field, the presence of an excitation gap does not change the value of δG, but the variance of the conductance is changed into [29] $\operatorname{Var} G/G_0 = 9/4\beta$, with $\beta = 1$ or $\beta = 4$ in the presence or absence of spin-rotation symmetry. Notice that time-reversal symmetry breaking then has only a relatively small 10% effect on the UCF [28], while in the absence of the excitation gap the effect on the variance is a factor of two [4].

3.5 Conclusion and comparison with a model Hamiltonian

In conclusion, we have shown that the distribution $P(G)$ of the electrical conductance in a quantum dot connecting a normal-metal to a superconducting electrode has a striking dependence on the topological quantum number Q of the superconductor, but only if the number of modes N in which the current is injected is sufficiently small. In the absence of time-reversal and spin-rotation symmetry, the distributions for $Q = -1$ and $Q = +1$ differ in the average conductance for $N = 1$, in the variance for $N = 2$, in the skewness for $N = 3$, and in the kurtosis for $N = 4$. More generally, the dependence appears in the cumulant of order N or $N/2$, depending on whether time-reversal symmetry is broken or not.

The system we have considered (Fig. 3.1) is constructed to ensure

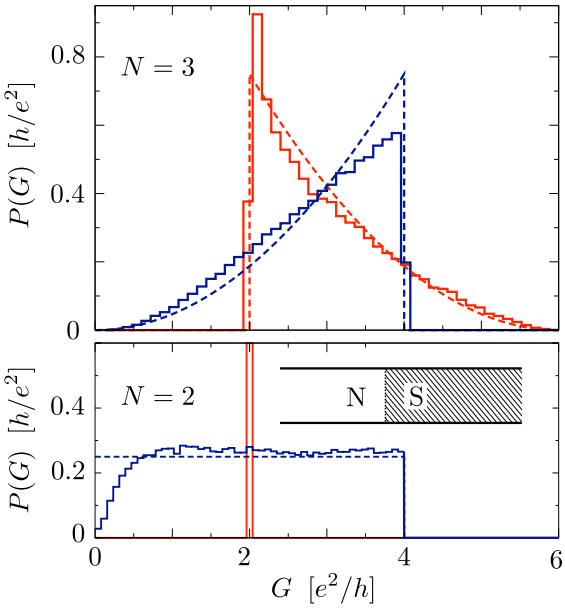

Figure 3.4. Comparison of the probability distribution of the electrical conductance as predicted by RMT (dashed curves) and as resulting from numerical simulation of the model Hamiltonian (3.24) (solid histograms). The simulation is for the disordered normal-metal–superconductor junction shown in the inset. The number of propagating modes in the normal region is $N = 2$ (lower panel) and $N = 3$ (upper panel), while the red and blue curves are for topological quantum number $Q = -1$ and $Q = +1$, respectively. The disorder strength is fixed at $U_0 = 130\,E_{\rm so}$ for $N = 2$ and $U_0 = 100\,E_{\rm so}$ for $N = 3$. The values used for Fermi energy and Zeeman energy (in units of $E_{\rm so}$) are as follows. For $N = 2$: $E_F = 12$, $E_Z = 3.8$ ($Q = 1$) and $E_F = 13$, $E_Z = 9$ ($Q = -1$). For $N = 3$: $E_F = 19$, $E_Z = 3.8$ ($Q = 1$) and $E_F = 19$, $E_Z = 8$ ($Q = -1$).

chaotic scattering, which is the requirement for application of the circular ensembles of RMT. Systems of present experimental focus in the search for Majorana bound states have a simpler wire geometry, without the quantum dot (Fig. 3.4, inset). Impurity scattering within a superconducting coherence length from the NS interface can still lead to chaotic dynamics, at least if the number of modes is sufficiently small that they are fully mixed by the disorder.

To test the applicability of our RMT results to such a system we have performed numerical simulations of the model Hamiltonian of Refs. 10, 11, which describes an InAs nanowire on an Al or Nb substrate. The

Bogoliubov-De Gennes Hamiltonian

$$\begin{aligned}\mathcal{H} &= \begin{pmatrix} 1 & 0 \\ 0 & \sigma_y \end{pmatrix} \begin{pmatrix} H_{\rm R} - E_F & \Delta \\ \Delta^* & E_F - \sigma_y H_{\rm R}^* \sigma_y \end{pmatrix} \begin{pmatrix} 1 & 0 \\ 0 & \sigma_y \end{pmatrix} \\ &= \begin{pmatrix} H_{\rm R} - E_F & \Delta\sigma_y \\ \Delta^*\sigma_y & E_F - H_{\rm R}^* \end{pmatrix} \end{aligned} \tag{3.24}$$

couples electron and hole excitations near the Fermi energy E_F through an s-wave superconducting order parameter Δ. (We have made a unitary transformation to ensure that the condition for particle-hole symmetry has the form used in the preceding sections.)

The excitations are confined to a wire of width W in the $x-y$ plane of the semiconductor surface inversion layer, where their dynamics is governed by the Rashba Hamiltonian

$$H_{\rm R} = \frac{\boldsymbol{p}^2}{2m_{\rm eff}} + U(\boldsymbol{r}) + \frac{\alpha_{\rm so}}{\hbar}(\sigma_x p_y - \sigma_y p_x) + \tfrac{1}{2} g_{\rm eff}\mu_B B\sigma_x. \tag{3.25}$$

The spin is coupled to the momentum $\boldsymbol{p} = -i\hbar\partial/\partial\boldsymbol{r}$ by the Rashba effect, and polarized through the Zeeman effect by a magnetic field B parallel to the wire (in the x-direction). Characteristic length and energy scales are $l_{\rm so} = \hbar^2/m_{\rm eff}\alpha_{\rm so}$ and $E_{\rm so} = m_{\rm eff}\alpha_{\rm so}^2/\hbar^2$. Typical values in InAs are $l_{\rm so} = 100\,{\rm nm}$, $E_{\rm so} = 0.1\,{\rm meV}$, $E_Z = \frac{1}{2} g_{\rm eff}\mu_B = 1\,{\rm meV}$ at $B = 1\,{\rm T}$.

We have solved the scattering problem numerically [30] by discretizing the Hamiltonian (3.24) on a square lattice (lattice constant $a = l_{\rm so}/20$), with an electrostatic disorder potential $U(x,y)$ that varies randomly from site to site, distributed uniformly in the interval $(-U_0, U_0)$. The disordered superconducting wire (width $W = 20\,a$, length $L = 800\,a$, $\Delta = 4\,E_{\rm so}$) is connected at two ends to ideal normal-metal leads, obtained by setting $\Delta, U_0 \equiv 0$ for $x < 0$, $x > L$. The length L was chosen large enough that the transmission probability through the wire was $< 10^{-2}$.

Results for the probability distribution of the electrical conductance are shown in Fig. 3.4, for $N = 2, 3$ and $Q = -1, 1$. (For $N = 1$ we simply find the two delta-function distributions at $G = (e^2/h)(1-Q)$, as expected.) The histograms were obtained by averaging over 10^5 disorder realizations, conditionally on the value of the topological quantum number $Q = \pm 1$ (calculated from $Q = \mathrm{sign}\,\mathrm{Det}\,r$, as in Ref. 26.) The agreement with the predictions from RMT is quite satisfactory.

Appendix 3.A Calculation of the invariant measure

In this appendix we derive the probability distributions of the Andreev reflection eigenvalues in the circular ensembles, given in Sec. 3.3. We work out the derivation for the symmetry classes D and DIII, for an even number $N = 2M$ of modes and for topological charge $Q = 1$, following established methods of random-matrix theory [31]. The calculations for the other ensembles are entirely analogous, so we do not present them here.

The circular ensembles are characterized by a uniform probability distribution, constrained only by fundamental symmetries. Uniformity in the unitary group is defined with respect to the invariant (Haar) measure $d\mu(r) = r^\dagger dr \equiv \delta r$. Since the polar decompositions in Sec. 3.3 give a parametrization of the (unitary) reflection matrix r in terms of the angles α_n, we can transform the measure into $d\mu(r) = J \prod_i dp_i \prod_n d\alpha_n$. The p_i's are the degrees of freedom of the matrices of eigenvectors and J is the Jacobian of the transformation. From this expression the probability distribution of the angles α_n follows upon integration over the p_i's,

$$P(\{\alpha_n\}) \propto \int J \prod_i dp_i, \tag{3.26}$$

up to a normalization constant.

The Jacobian can be found from the metric tensor $g_{\mu\nu}$, which can be read off from the trace $\mathrm{Tr}\,\delta r \delta r^\dagger$ when it is expressed in terms of the infinitesimals $d\alpha_n$ and dp_i (collectively denoted as dx_μ):

$$\mathrm{Tr}\,\delta r \delta r^\dagger = \sum_{\mu,\nu} g_{\mu\nu} dx_\mu dx_\nu, \quad J = |\mathrm{Det}\, g_{\mu\nu}|^{1/2}. \tag{3.27}$$

We carry out this calculation first for class D and then for class DIII.

3.A.1 Class D (ensemble CRE)

In view of the polar decomposition (3.7) one has

$$\begin{pmatrix} U^\dagger & 0 \\ 0 & U^{\mathrm{T}} \end{pmatrix} dr \begin{pmatrix} V & 0 \\ 0 & V^* \end{pmatrix} = \begin{pmatrix} \delta U & 0 \\ 0 & \delta U^* \end{pmatrix} L + dL - L \begin{pmatrix} \delta V & 0 \\ 0 & \delta V^* \end{pmatrix}, \tag{3.28}$$

where we abbreviated

$$L = \begin{pmatrix} \Gamma & -i\Lambda \\ i\Lambda & \Gamma \end{pmatrix}. \tag{3.29}$$

The quantities $\delta U = U^\dagger dU$ and $\delta V = V^\dagger dV$ represent measures on the eigenvector manifolds. We used that $d(V^\dagger V) = 0 \Rightarrow (dV^\dagger)V = (\delta V)^\dagger = -\delta V$.

Substitution of Eq. (3.28) into $\mathrm{Tr}\,\delta r \delta r^\dagger = \mathrm{Tr}\,dr dr^\dagger$ gives

$$\begin{aligned} \mathrm{Tr}\,\delta r \delta r^\dagger = {} & 2\,\mathrm{Tr}\,L \begin{pmatrix} \delta V & 0 \\ 0 & \delta V^* \end{pmatrix} L^\dagger \begin{pmatrix} \delta U & 0 \\ 0 & \delta U^* \end{pmatrix} \\ & - \mathrm{Tr}\,[\delta U^2 + (\delta U^*)^2 + \delta V^2 + (\delta V^*)^2] \\ & + \mathrm{Tr}\,dL dL^\dagger. \end{aligned} \tag{3.30}$$

(All other cross terms vanish.) In terms of Γ and Λ this can be expressed as a sum of five traces,

$$\begin{aligned} \mathrm{Tr}\,\delta r \delta r^\dagger = {} & \mathrm{Tr}\,(\Gamma\delta V - \delta U\Gamma)(\Gamma^{\mathrm{T}}\delta U - \delta V\Gamma^{\mathrm{T}}) \\ & + \mathrm{Tr}\,(\Gamma\delta V^* - \delta U^*\Gamma)(\Gamma^{\mathrm{T}}\delta U^* - \delta V^*\Gamma^{\mathrm{T}}) \\ & + \mathrm{Tr}\,(\Lambda\delta V^* - \delta U\Lambda)(\Lambda^{\mathrm{T}}\delta U - \delta V^*\Lambda^{\mathrm{T}}) \\ & + \mathrm{Tr}\,(\Lambda\delta V - \delta U^*\Lambda)(\Lambda^{\mathrm{T}}\delta U^* - \delta V\Lambda^{\mathrm{T}}) \\ & + \mathrm{Tr}\,dL dL^{\mathrm{T}} \\ \equiv {} & T_1 + T_2 + T_3 + T_4 + T_5. \end{aligned} \tag{3.31}$$

Each of the traces in Eq. (3.31) is of the form $\mathrm{Tr}\,AA^\dagger = \sum_{ij} |A_{ij}|^2$, and is therefore real. Since the second line is the complex conjugate of the first line and the fourth line is the complex conjugate of the third line, their traces are the same, hence $T_1 = T_2$ and $T_3 = T_4$. For the evaluation of the expression we need to distinguish between the different values of the topological quantum number and between the cases of odd and even number of channels.

We work out the calculation for $N = 2M$ even and $Q = 1$, when Λ and Γ are given by Eqs. (3.8) and (3.9). The trace T_5 is easiest to evaluate,

$$T_5 = \sum_{i,j} |dL_{ij}|^2 = 4 \sum_{i=1}^{M} d\alpha_i^2. \tag{3.32}$$

This trace contributes a diagonal block to the metric tensor and a constant factor to the Jacobian, for M independent real parameters. The other two traces T_1 and T_3 require more work,

$$\begin{aligned} T_1 = & \sum_{r<s=1}^{M} \sum_{k,l=0}^{1} \Big\{ \tfrac{1}{2}(\cos\alpha_r + \cos\alpha_s)^2 |\delta U_{2r-k,2s-l} - (-1)^{k+l} \delta V_{2r-\bar{k},2s-\bar{l}}|^2 \\ & + \tfrac{1}{2}(\cos\alpha_r - \cos\alpha_s)^2 |\delta U_{2r-k,2s-l} + (-1)^{k+l} \delta V_{2r-\bar{k},2s-\bar{l}}|^2 \Big\} \\ & + \sum_{m}^{M} \sum_{k,l=0}^{1} \cos^2\alpha_m |\delta V_{2m-k,2m-l} - (-1)^{k+l} \delta U_{2m-\bar{k},2m-\bar{l}}|^2, \end{aligned} \tag{3.33}$$

$$\begin{aligned} T_3 = & \sum_{r<s=1}^{M} \sum_{k,l=0}^{1} \{ \tfrac{1}{2}(\sin\alpha_r + \sin\alpha_s)^2 |\delta V^*_{2r-k,2s-l} - \delta U_{2r-k,2s-l}|^2 \\ & + \tfrac{1}{2}(\sin\alpha_r - \sin\alpha_s)^2 |\delta V^*_{2r-k,2s-l} + \delta U_{2r-k,2s-l}|^2 \} \\ & + \sum_{m}^{M} \sum_{k,l=0}^{1} \sin^2\alpha_m |\delta V^*_{2m-k,2m-l} - \delta U_{2m-k,2m-l}|^2. \end{aligned} \tag{3.34}$$

We denote $\bar{k} = 0, 1$ for $k = 1, 0$.

We group the indices of the matrices δU and δV into 2×2 blocks, and consider first the off-diagonal blocks. For these we can choose as independent parameters

$$\begin{aligned} &\delta U_{2r,2s}, \quad \delta U_{2r-1,2s}, \quad \delta U_{2r,2s-1}, \quad \delta U_{2r-1,2s-1}, \\ &\delta V_{2r,2s}, \quad \delta V_{2r-1,2s}, \quad \delta V_{2r,2s-1}, \quad \delta V_{2r-1,2s-1}, \end{aligned}$$

with $1 \le r < s \le M$. The real and imaginary parts, denoted by $\delta U^{\mathrm{R}}, \delta U^{\mathrm{I}}, \delta V^{\mathrm{R}}, \delta V^{\mathrm{I}}$, produce a total of $8M(M-1)$ independent parameters. The contribution to $\mathrm{Tr}\,\delta r \delta r^\dagger$ for given values of r and s has the

form

$$\begin{aligned}
&\sum_{k=2r-1}^{2r}\sum_{l=2s-1}^{2s}\Big\{4\left[(\delta U_{kl}^{\mathrm{R}})^2+(\delta U_{kl}^{\mathrm{I}})^2+(\delta V_{kl}^{\mathrm{R}})^2+(\delta V_{kl}^{\mathrm{I}})^2\right]\\
&\quad+2a\left[\delta V_{kl}^{\mathrm{R}}\delta U_{kl}^{\mathrm{R}}-\delta V_{kl}^{\mathrm{I}}\delta U_{kl}^{\mathrm{I}}\right]\Big\}\\
&+2b\left[\delta V_{2r-1,2s-1}^{\mathrm{R}}\delta U_{2r,2s}^{\mathrm{R}}+\delta V_{2r-1,2s-1}^{\mathrm{I}}\delta U_{2r,2s}^{\mathrm{I}}\right]\\
&+2b\left[\delta V_{2r,2s}^{\mathrm{R}}\delta U_{2r-1,2s-1}^{\mathrm{R}}+\delta V_{2r,2s}^{\mathrm{I}}\delta U_{2r-1,2s-1}^{\mathrm{I}}\right]\\
&-2b\left[\delta V_{2r-1,2s}^{\mathrm{R}}\delta U_{2r,2s-1}^{\mathrm{R}}+\delta V_{2r-1,2s}^{\mathrm{I}}\delta U_{2r,2s-1}^{\mathrm{I}}\right]\\
&-2b\left[\delta V_{2r,2s-1}^{\mathrm{R}}\delta U_{2r-1,2s}^{\mathrm{R}}+\delta V_{2r,2s-1}^{\mathrm{I}}\delta U_{2r-1,2s}^{\mathrm{I}}\right],
\end{aligned}$$

where we abbreviated $a=-4\sin\alpha_r\sin\alpha_s$ and $b=-4\cos\alpha_r\cos\alpha_s$.

The contribution to the metric tensor is a block matrix with elements

$$\begin{pmatrix}
4\tau_0 & 0 & 0 & 0 & a\tau_z & 0 & 0 & b\tau_0\\
0 & 4\tau_0 & 0 & 0 & 0 & a\tau_z & -b\tau_0 & 0\\
0 & 0 & 4\tau_0 & 0 & 0 & -b\tau_0 & a\tau_z & 0\\
0 & 0 & 0 & 4\tau_0 & b\tau_0 & 0 & 0 & a\tau_z\\
a\tau_z & 0 & 0 & b\tau_0 & 4\tau_0 & 0 & 0 & 0\\
0 & a\tau_z & -b\tau_0 & 0 & 0 & 4\tau_0 & 0 & 0\\
0 & -b\tau_0 & a\tau_z & 0 & 0 & 0 & 4\tau_0 & 0\\
b\tau_0 & 0 & 0 & a\tau_z & 0 & 0 & 0 & 4\tau_0
\end{pmatrix},$$

where the Pauli matrix τ_z and the 2×2 unit matrix τ_0 were introduced to account for real and imaginary parts in a compact way. The determinant of this matrix is $(\sin^2\alpha_r-\sin^2\alpha_s)^8$, hence the contribution to the Jacobian from the off-diagonal matrix elements is

$$J_{\text{off-diagonal}}=\prod_{r<s=1}^{M}\left|\sin^2\alpha_r-\sin^2\alpha_s\right|^4. \tag{3.35}$$

Next we consider the diagonal blocks. We choose as independent parameters

$$\begin{aligned}
w_1&=-i(\delta V_{2m,2m}-\delta U_{2m-1,2m-1}),\\
w_2&=-i(\delta V_{2m-1,2m-1}-\delta U_{2m,2m}),\\
w_3&=-i(\delta V_{2m,2m}+\delta U_{2m,2m}),\\
w_4&=\delta V_{2m-1,2m}+\delta U_{2m,2m-1}.
\end{aligned}$$

These are in total $5M$ real parameters. (Since w_1, w_2, w_3 are real numbers they contribute only M parameters each.) The contribution to $\mathrm{Tr}\,\delta r \delta r^\dagger$ is

$$w_1^2 + w_2^2 + 2(w_2 w_3 - w_1 w_3 - w_1 w_2 + w_3^2)\sin^2\alpha_m + 2w_4^2,$$

and the contribution to the metric tensor is the block matrix

$$\begin{pmatrix} 2 & 0 & 0 & 0 \\ 0 & 1 & -\sin^2\alpha_m & -\sin^2\alpha_m \\ 0 & -\sin^2\alpha_m & 1 & \sin^2\alpha_m \\ 0 & -\sin^2\alpha_m & \sin^2\alpha_m & 2\sin^2\alpha_m \end{pmatrix},$$

with determinant $2(\sin\alpha_m \cos\alpha_m)^2$. Hence the contribution to the Jacobian from the diagonal matrix elements is

$$J_{\text{diagonal}} = \prod_{m=1}^{M} |\sin\alpha_m \cos\alpha_m|. \tag{3.36}$$

The number of independent parameters that we have accounted for totals to $8M^2 - 2M$, which should equal the number of degrees of freedom of a matrix in class D. The matrix space in class D is isomorphic to the group of $2N \times 2N$ orthogonal matrices [4], which indeed has $N(2N-1) = 8M^2 - 2M$ degrees of freedom.

Gathering all terms that contribute to the Jacobian in Eq. (3.26), we obtain the probability distribution

$$P(\{\alpha_n\}) \propto \prod_{r<s=1}^{M} \left|\sin^2\alpha_r - \sin^2\alpha_s\right|^4 \prod_{m=1}^{M} |\sin\alpha_m \cos\alpha_m|\,. \tag{3.37}$$

The integration $\int dp_i$ over the degrees of freedom of the eigenvector matrices only contributes a prefactor, which can be absorbed in the proportionality constant. Upon transformation to the Andreev reflection eigenvalues $R_n = \sin^2\alpha_n$, we arrive at the result (3.13) stated in the main text.

3.A.2 Class DIII (ensemble T-CRE)

For the treatment of class DIII it is useful to notice the similarity of the polar decomposition of $i\Sigma_y r$ given in Eq. (3.16) to the one of r in class D given in Eq. (3.7). Since $\delta(i\Sigma_y r) = \delta r$ all the equations up to

Eq. (3.34) derived for class D also hold for class DIII, upon replacement $U \mapsto \Omega$ and $V \mapsto \Omega^*$. (As before, we only give the detailed derivation for $Q = 1$.) The expressions for the traces T_1 and T_3 then simplify to

$$\begin{aligned} T_1 = \sum_{r<s=1}^{M} \big\{ &(\cos\alpha_r + \cos\alpha_s)^2 \left[|\delta\Omega_{2r,2s} - \delta\Omega^*_{2r-1,2s-1}|^2 \right. \\ &\left. + |\delta\Omega_{2r-1,2s} + \delta\Omega^*_{2r,2s-1}|^2 \right] \\ &+ (\cos\alpha_r - \cos\alpha_s)^2 \left[|\delta\Omega_{2r,2s} + \delta\Omega^*_{2r-1,2s-1}|^2 \right. \\ &\left. + |\delta\Omega_{2r-1,2s} - \delta\Omega^*_{2r,2s-1}|^2 \right] \big\} \\ &+ 2\sum_{m}^{M} \cos^2\alpha_m |\delta\Omega_{2m,2m} + \delta\Omega_{2m-1,2m-1}|^2, \end{aligned} \tag{3.38}$$

$$T_3 = 2 \sum_{r<s=1}^{M} \sum_{k,l=0}^{1} (\sin\alpha_r - \sin\alpha_s)^2 |\delta\Omega_{2r-k,2s-l}|^2. \tag{3.39}$$

For the off-diagonal blocks we choose

$$\delta\Omega_{2r,2s}, \quad \delta\Omega_{2r-1,2s}, \quad \delta\Omega_{2r,2s-1}, \quad \delta\Omega_{2r-1,2s-1},$$

with $1 \le r < s \le M$, as the independent real parameters (a total of $4M^2 - 4M$). The contribution to $\mathrm{Tr}\,\delta r \delta r^+$ for given values of r and s is

$$\begin{aligned} c \sum_{k=2r-1}^{2r} \sum_{l=2s-1}^{2s} &\left[(\delta\Omega^{\mathrm{R}}_{kl})^2 + (\delta\Omega^{\mathrm{I}}_{kl})^2 \right] \\ + 2d &\left[\delta\Omega^{\mathrm{R}}_{2r-1,2s} \delta\Omega^{\mathrm{R}}_{2r,2s-1} - \delta\Omega^{\mathrm{I}}_{2r-1,2s} \delta\Omega^{\mathrm{I}}_{2r,2s-1} \right. \\ &\left. - \delta\Omega^{\mathrm{R}}_{2r-1,2s-1} \delta\Omega^{\mathrm{R}}_{2r,2s} + \delta\Omega^{\mathrm{I}}_{2r-1,2s-1} \delta\Omega^{\mathrm{I}}_{2r,2s} \right], \end{aligned}$$

with $c = 4 - 4\sin\alpha_r \sin\alpha_s$ and $d = 4\cos\alpha_r \cos\alpha_s$. The contribution to the metric tensor is a block matrix with elements

$$\begin{pmatrix} c\tau_0 & 0 & 0 & -d\tau_z \\ 0 & c\tau_0 & d\tau_z & 0 \\ 0 & d\tau_z & c\tau_0 & 0 \\ -d\tau_z & 0 & 0 & c\tau_0 \end{pmatrix},$$

with determinant $(\sin\alpha_r - \sin\alpha_s)^8$. The contribution to the Jacobian is

$$J_{\text{off-diagonal}} = \prod_{r<s=1}^{M} |\sin\alpha_r - \sin\alpha_s|^4 . \tag{3.40}$$

The diagonal blocks have M independent degrees of freedom,

$$\delta\Omega_{2m\,2m} + \delta\Omega_{2m-1\,2m-1},$$

which contribute to the Jacobian a factor

$$J_{\text{diagonal}} = \prod_{m=1}^{M} |\cos\alpha_m| \,. \tag{3.41}$$

The total number of independent parameters (including also the M degrees of freedom from the α_n's) is then $4M^2 - 2M$. This agrees with the number of degrees of freedom of the matrix space $O(2N)/U(N)$ in class DIII [4].

The distribution of the α_n's results from the product of $J_{\text{off-diagonal}}$ and J_{diagonal},

$$P(\{\alpha_n\}) \propto \prod_{r<s=1}^{M} |\sin\alpha_r - \sin\alpha_s|^4 \prod_{m=1}^{M} |\cos\alpha_m| \,. \tag{3.42}$$

Transformation to $\xi_n = \sin\alpha_n$ gives the expression (3.18) in the main text.

Appendix 3.B Proof of the topological-charge theorem for circular ensembles

The theorem we wish to prove states that the p-th cumulant of the conductance in the N-mode circular ensemble is independent of the topological charge Q for $p < N/d$, with $d = 1$ in the CRE and $d = 2$ in the T-CRE.

We start from the definition (3.2) of the conductance, which we rewrite as

$$G/G_0 = \tfrac{1}{2}\mathrm{Tr}\,[1 - r^\dagger \tau_z r(1+\tau_z)], \quad \tau_z = \begin{pmatrix} 1 & 0 \\ 0 & -1 \end{pmatrix}. \tag{3.43}$$

The reflection matrix r is a $2N \times 2N$ unitary matrix, satisfying the particle-hole symmetry relation (3.3), which we rewrite as

$$r = \tau_x r^* \tau_x, \quad \tau_x = \begin{pmatrix} 0 & 1 \\ 1 & 0 \end{pmatrix}. \tag{3.44}$$

This equation implies that $\mathrm{Tr}\, r^\dagger \tau_z r = 0$, hence Eq. (3.43) reduces to

$$G/G_0 = \tfrac{1}{2}\mathrm{Tr}\,[1 - r^\dagger \tau_z r \tau_z)]. \tag{3.45}$$

The p-th cumulant of G contains only averages $m_q = \langle (\mathrm{Tr}\, r^\dagger \tau_z r \tau_z)^q \rangle$ with $q \leq p$, hence to prove the theorem is it sufficient to prove that m_p is independent of Q for $p < N/d$.

We first do this for the CRE. Then the average m_p can be written as

$$m_p = \int d\mu(r) \left(\mathrm{Tr}\, r^\dagger \tau_z r \tau_z\right)^p \tfrac{1}{2}(1 + Q\,\mathrm{Det}\, r), \tag{3.46}$$

where $d\mu(r)$ is the invariant measure of class D. The defining property of this measure is that $d\mu(Ur) = d\mu(rU) = d\mu(r)$ for any $2N \times 2N$ unitary matrix U that satisfies $U = \tau_x U^* \tau_x$. What we seek to prove, therefore, is that

$$\int d\mu(r) \left(\mathrm{Tr}\, r^\dagger \tau_z r \tau_z\right)^p \mathrm{Det}\, r = 0 \;\text{ if }\; p < N. \tag{3.47}$$

We decompose

$$\tau_z = \sum_{n=1}^{N} \tau^{(n)}, \quad \tau^{(n)}_{kl} = \delta_{k,l}(\delta_{k,n} - \delta_{k,n+N}) \tag{3.48}$$

and apply this decomposition to one of the τ_z's in Eq. (3.47),

$$\begin{aligned}\left(\mathrm{Tr}\, r^\dagger \tau_z r \tau_z\right)^p = \sum_{p_1=0}^{N} \sum_{p_2=0}^{N} \cdots \sum_{p_N=0}^{N} \frac{p!}{p_1! p_2! \cdots p_N!} \\ \times \delta_{p,p_1+p_2+\cdots+p_N} \prod_{n=1}^{N} \left(\mathrm{Tr}\, r^\dagger \tau^{(n)} r \tau_z\right)^{p_n}.\end{aligned} \tag{3.49}$$

Consider one of the terms

$$\mathcal{M} = \int d\mu(r) \prod_{n=1}^{N} \left(\mathrm{Tr}\, r^\dagger \tau^{(n)} r \tau_z\right)^{p_n} \mathrm{Det}\, r. \tag{3.50}$$

If $p < N$, there is at least one index $n_0 \in \{1, 2, \ldots N\}$ such that $p_{n_0} = 0$. Transform $r \mapsto U^{(n_0)} r$, with

$$U^{(n_0)}_{kl} = \begin{cases} \delta_{k,l} & \text{if } k \neq n_0, n_0 + N, \\ \delta_{l,n_0+N} & \text{if } k = n_0, \\ \delta_{l,n_0} & \text{if } k = n_0 + N, \end{cases} \tag{3.51}$$

a real, symmetric, unitary matrix which commutes with τ_x. This transformation does not change the invariant measure, $d\mu(U^{(n_0)}r) = d\mu(r)$, while the integrand transforms to

$$\begin{aligned}\mathcal{M} &= \int d\mu(r) \prod_{n=1}^{N} \left(\operatorname{Tr} r^\dagger U^{(n_0)} \tau^{(n)} U^{(n_0)} r \tau_z\right)^{p_n} \\ &\quad \times \operatorname{Det} U^{(n_0)} r \\ &= -\int d\mu(r) \prod_{n=1}^{N} \left(\operatorname{Tr} r^\dagger \tau^{(n)} r \tau_z\right)^{p_n} \operatorname{Det} r \\ &= -\mathcal{M}, \end{aligned} \tag{3.52}$$

since $\operatorname{Det} U^{(n_0)} = -1$ and $U^{(n_0)}$ commutes with $\tau^{(n)}$ for $n \neq n_0$, while $p_{n_0} = 0$. Hence $\mathcal{M} = 0$.

This completes the proof for the CRE. For the T-CRE, we seek to prove that

$$\int d\mu(r) \left(\operatorname{Tr} r^\dagger \tau_z r \tau_z\right)^p \operatorname{Pf} i\Sigma_y r = 0 \ \text{ if } \ p < N/2, \tag{3.53}$$

where now $d\mu(r)$ is the invariant measure of class DIII. The invariance property reads $d\mu(\Sigma_y U^{\mathrm{T}} \Sigma_y r U) = d\mu(r)$ for any $2N \times 2N$ unitary matrix U that satisfies $U = \tau_x U^* \tau_x$. Since τ_z and Σ_y commute, we may rewrite Eq. (3.53) as

$$\int d\mu(r) \left(\operatorname{Tr} r^\dagger \Sigma_y \tau_z \Sigma_y r \tau_z\right)^p \operatorname{Pf} i\Sigma_y r = 0 \ \text{ if } \ p < N/2. \tag{3.54}$$

Substitute the decomposition (3.48) in both the τ_z's,

$$\begin{aligned}\left(\operatorname{Tr} r^\dagger \Sigma_y \tau_z \Sigma_y r \tau_z\right)^p &= \sum_{p_{11}=0}^{N} \cdots \sum_{p_{NN}=0}^{N} \frac{p!}{\prod_{n,m} p_{nm}!} \\ &\quad \times \delta_{p, \sum_{n,m} p_{nm}} \prod_{n,m=1}^{N} \left(\operatorname{Tr} r^\dagger \Sigma_y \tau^{(n)} \Sigma_y r \tau^{(m)}\right)^{p_{nm}}. \end{aligned} \tag{3.55}$$

Consider one of the terms

$$\begin{aligned}\mathcal{M} &= \int d\mu(r) \prod_{n,m=1}^{N} \left(\operatorname{Tr} r^\dagger \Sigma_y \tau^{(n)} \Sigma_y r \tau^{(m)}\right)^{p_{nm}} \\ &\quad \times \operatorname{Pf} i\Sigma_y r. \end{aligned} \tag{3.56}$$

If $p < N/2$, there is at least one index $n_0 \in \{1, 2, \dots N\}$ such that $p_{n_0 m} = 0$ and $p_{n n_0} = 0$ for each $n, m \in \{1, 2, \dots N\}$. Transform $r \mapsto \Sigma_y U^{(n_0)} \Sigma_y r U^{(n_0)}$, with $U^{(n_0)}$ defined in Eq. (3.51). This transformation does not change the invariant measure, so the integral transforms to

$$\begin{aligned}
\mathcal{M} = & \int d\mu(r) \prod_{n,m=1}^{N} \Big(\mathrm{Tr}\, r^\dagger \Sigma_y U^{(n_0)} \tau^{(n)} U^{(n_0)} \Sigma_y r \\
& \times U^{(n_0)} \tau^{(m)} U^{(n_0)} \Big)^{p_{nm}} \mathrm{Pf}\left(U^{(n_0)} i \Sigma_y r U^{(n_0)} \right) \\
= & - \int d\mu(r) \prod_{n,m=1}^{N} \left(\mathrm{Tr}\, r^\dagger \Sigma_y \tau^{(n)} \Sigma_y r \tau^{(m)} \right)^{p_{nm}} \\
& \times \mathrm{Pf}\, i \Sigma_y r = -\mathcal{M}, \qquad (3.57)
\end{aligned}$$

where we have used that $\mathrm{Pf}\, X Y X^{\mathrm{T}} = (\mathrm{Det}\, X)(\mathrm{Pf}\, Y)$. Hence $\mathcal{M} = 0$ and we have completed the proof for the T-CRE.

Bibliography

[1] R. Blümel and U. Smilansky, Phys. Rev. Lett. **64**, 241 (1990).

[2] F. J. Dyson, J. Math. Phys. **3**, 140 (1962).

[3] *The Oxford Handbook on Random Matrix Theory*, edited by G. Akemann, J. Baik, and P. Di Francesco, Oxford University Press, 723–758 (2011).

[4] A. Altland and M. R. Zirnbauer, Phys. Rev. B **55**, 1142 (1997).

[5] J. P. Dahlhaus, B. Béri, and C. W. J. Beenakker, Phys. Rev. B **82**, 014536 (2010).

[6] A. Yu. Kitaev Phys. Usp. **44** (suppl.), 131 (2001).

[7] X.-L. Qi, T. L. Hughes, and S.-C. Zhang, Phys. Rev. B **78**, 195424 (2008); X.-L. Qi and S.-C. Zhang, Rev. Mod. Phys. **83**, 1057 (2011) .

[8] A. P. Schnyder, S. Ryu, A. Furusaki, and A. W. W. Ludwig, Phys. Rev. B **78** 195125 (2008); S. Ryu, A. P. Schnyder, A. Furusaki, and A. W. W. Ludwig, New J. Phys. **12**, 065010 (2010).

[9] L. Fu and C. L. Kane, Phys. Rev. B 79, 161408(R) (2009); M. Z. Hasan and C. L. Kane, Rev. Mod. Phys. **82**, 3045 (2010).

[10] R. M. Lutchyn, J. D. Sau, and S. Das Sarma, Phys. Rev. Lett. **105**, 077001 (2010).

[11] Y. Oreg, G. Refael, and F. von Oppen, Phys. Rev. Lett. **105**, 177002 (2010).

[12] M. Wimmer, A. R. Akhmerov, M. V. Medvedyeva, J. Tworzydło, and C. W. J. Beenakker, Phys. Rev. Lett. **105**, 046803 (2010).

[13] A. C. Potter and P. A. Lee, Phys. Rev. Lett. **105**, 227003 (2010).

[14] R. M. Lutchyn, T. Stanescu, and S. Das Sarma, Phys. Rev. Lett. **106**, 127001 (2011).

[15] M. Duckheim and P. W. Brouwer, Phys. Rev. B **83**, 054513 (2011) .

[16] K. T. Law, P. A. Lee, and T. K. Ng, Phys. Rev. Lett. **103**, 237001 (2009).

[17] K. Flensberg, Phys. Rev. B **82**, 180516(R) (2010).

[18] B. Béri, J. N. Kupferschmidt, C. W. J. Beenakker, and P. W. Brouwer, Phys. Rev. B **79**, 024517 (2009).

[19] M. Wimmer, A. R. Akhmerov, J. P. Dahlhaus, and C. W. J. Beenakker, New J. Phys. **13** 053016 (2011).

[20] I. M. Khaymovich, N. M. Chtchelkatchev, I. A. Shereshevskii, and A. S. Mel'nikov, Europhys. Lett. **91**, 17005 (2010).

[21] G. E. Blonder, M. Tinkham, and T. M. Klapwijk, Phys. Rev. B **25**, 4515 (1982).

[22] J. H. Bardarson, J. Phys. A **41**, 405203 (2008).

[23] B. Béri, Phys. Rev. B **79**, 245315 (2009).

[24] M. Bocquet, D. Serban, and M. Zirnbauer, Nucl. Phys. B **578**, 628 (2000).

[25] F. Merz and J. T. Chalker, Phys. Rev. B **65**, 054425 (2002).

[26] A. R. Akhmerov, J. P. Dahlhaus, F. Hassler, M. Wimmer, and C. W. J. Beenakker, Phys. Rev. Lett. **106**, 057001 (2011).

[27] I. C. Fulga, F. Hassler, A. R. Akhmerov, and C. W. J. Beenakker, Phys. Rev. B **83**, 155429 (2011).

[28] C. W. J. Beenakker, Rev. Mod. Phys. **69**, 731 (1997).

[29] C. W. J. Beenakker, Phys. Rev. B **47**, 15763 (1993).

[30] M. Wimmer and K. Richter, J. Comput. Phys. **228**, 8548 (2009).

[31] P. J. Forrester, *Log-Gases and Random Matrices* (Princeton University Press, Princeton, 2010).

Chapter 4

Quantum point contact as a probe of a topological superconductor

4.1 Introduction

Massless Dirac fermions have the special property that they can be confined without the energy cost from zero-point motion. In graphene, this manifests itself as a Landau level at zero energy, without the usual $\frac{1}{2}\hbar\omega_c$ offset [1]. The zeroth Landau level contributes half as much to the Hall conductance as the higher levels (because it is already half-filled in equilibrium), leading to the celebrated half-integer quantum Hall plateaus [2, 3]. In a semiclassical description, the π phase shift at turning points, responsible for the zero-point energy, is canceled by the Berry phase of π, characteristic for the periodic orbit of a Dirac fermion.

The same absence of zero-point energy appears when Dirac fermions are confined by superconducting barriers, produced by the proximity effect in a topological insulator [4, 5]. Because of particle-hole symmetry in a superconductor, a state at zero excitation energy is a Majorana bound state, with identical creation and annihilation operators. A superconductor that supports Majorana bound states is called topological [6, 7].

Tunneling spectroscopy is a direct method of detection of a topological superconductor [8–11]. Resonant tunneling into a Majorana bound state produces a conductance of $2e^2/h$, while without this state the

tunneling conductance vanishes [9]. The tunneling resonance becomes broader if the tunneling probability is increased, and one might surmise that the resonance would vanish if the conductance is measured via a ballistic contact. We show in this chapter, by means of a model calculation, that the contrary is true: The signature of the topological phase is more robust when measured by a ballistic contact than by a tunnel contact.

Our model calculation is in accord with general theoretical considerations [12, 13], but may appear counter-intuitive. After all, the Majorana bound state no longer exists as an individual energy level if it is connected by a ballistic contact to a normal metal, since the level broadening then exceeds the level spacing. As we have found, the topological phase of the superconductor still manifests itself in the conductance of a ballistic point contact, in a way reminiscent of the half-integer quantum Hall plateaus.

4.2 Integer versus half-integer conductance plateaus

We consider the model Hamiltonian [14, 15] of a two-dimensional semiconducting wire with an s-wave proximity-induced superconducting gap Δ. (See App. 4.A for a detailed description.) We have calculated the scattering matrix of a quantum point contact (QPC) in the normal region (N) at a distance d from the superconducting region (S), by discretizing the Hamiltonian on a square lattice (lattice constant $a = l_{\rm so}/40$, with $l_{\rm so}$ the spin-orbit scattering length). Our key result is presented in Fig. 4.1. The number of propagating modes in the point contact (and hence the transmittance $T_{\rm QPC}$) is varied by changing the electrostatic potential $V_{\rm QPC}$ inside the point contact, at constant Fermi energy E_F. Spin degeneracy is removed by the Zeeman energy $E_Z = \frac{1}{2}g\mu_B B$ in a magnetic field B (parallel to the wire), so that when the entire system is in the normal state ($\Delta \to 0$) the conductance increases step wise in units of e^2/h (black dashed curve, showing the step wise increase of the transmittance from $T_{\rm QPC} = 0$, for a fully pinched off contact, to $T_{\rm QPC} = 8$, for a maximally open contact).

The conductance G of the NS junction is obtained from the Andreev reflection eigenvalues R_n at the Fermi level,

$$G = \frac{2e^2}{h}\sum_n R_n(E_F). \tag{4.1}$$

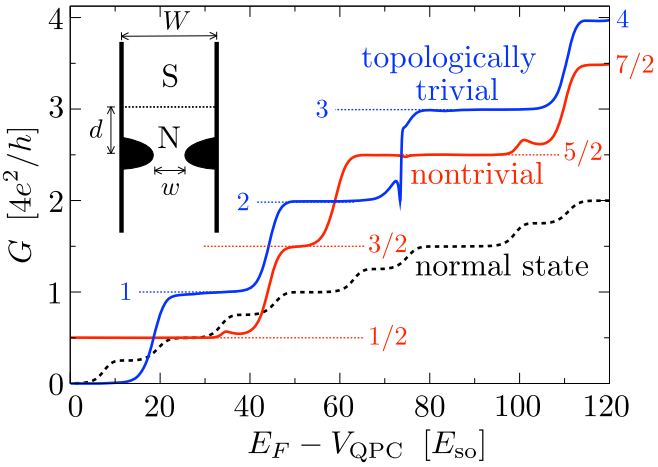

Figure 4.1. Solid curves: conductance of a ballistic normal-metal–superconductor (NS) junction, with the superconductor in a topologically trivial phase (blue curve, $\Delta = 8\,E_{\rm so}$) or nontrivial phase (red curve, $\Delta = 4\,E_{\rm so}$). The black dashed curve is for an entirely normal system ($\Delta = 0$). The data is obtained from the model Hamiltonian [14, 15] of a semiconducting wire on a superconducting substrate in a parallel magnetic field (Zeeman energy $E_Z = 6\,E_{\rm so}$), for the ballistic point contact geometry shown in the inset (not to scale, $d = 2.5\,l_{\rm so}$, $W = l_{\rm so}$). By varying the potential $V_{\rm QPC}$ at constant Fermi energy $E_F = 120\,E_{\rm so}$, the point contact width w is varied between 0 and W. The dotted horizontal lines indicate the shift from integer to half-integer conductance plateaus upon transition from the topologically trivial to nontrivial phase.

The factor of two accounts for the fact that charge is added to the superconductor as Cooper pairs of charge $2e$. (The spin degree of freedom is included in the sum over n.) The superconductor can be in a topologically trivial ($Q = 1$) or nontrivial ($Q = -1$) phase, depending on the relative magnitude of E_Z, Δ, and the spin-orbit coupling energy $E_{\rm so} = \hbar^2/m_{\rm eff}l_{\rm so}^2$. The blue and red solid curves show these two cases, where the topological quantum number $Q = \operatorname{sign}\operatorname{Det} r$ was obtained in an independent calculation from the determinant of the reflection matrix [16–18]. As we see from Fig. 4.1, the conductance shows plateaus at values G_p, $p = 0, 1, 2, \ldots$, given by

$$G_p = \frac{4e^2}{h} \times \begin{cases} p & \text{if } Q = 1, \\ p + 1/2 & \text{if } Q = -1. \end{cases} \tag{4.2}$$

The sequence of conductance plateaus in the topologically trivial and nontrivial phases can be understood from basic symmetry requirements. As discovered by Béri [13], particle-hole symmetry requires that the R_n's at the Fermi level are either twofold degenerate or equal to 0 or 1. (See App. 4.B for a derivation.) A nondegenerate unit Andreev reflection eigenvalue is therefore pinned to exactly this value and contributes to the conductance a quantized amount of $2e^2/h$. This is the signature of the topological superconductor which persists even after the Majorana bound state has merged with the continuum of states in the normal metal contact.

If we include only the degenerate R_n's in the sum over n (indicated by a prime, $\sum'$), we may write

$$G = \frac{e^2}{h}\left(1 - Q + 4\sum\nolimits'_n R_n\right). \tag{4.3}$$

A new mode that is fully Andreev reflected thus adds $4e^2/h$ to the conductance, with an offset of 0 or $2e^2/h$ in the topologically trivial or nontrivial phases. The resulting conductance plateaus therefore appear at integer or half-integer multiples of $4e^2/h$, depending on the topological quantum number, as expressed by Eq. (4.2) and observed in the model calculation.

The quantum point contact conductance plateaus in the topologically nontrivial phase occur at the same half-integer multiples of $4e^2/h$ as the quantum Hall plateaus in graphene, but the multiplicity of 4 has an entirely different origin: In graphene, the factor of four accounts for the twofold spin and valley degeneracy of the energy levels, while in the NS junction there is no degeneracy of the energy levels. One factor of two accounts for the Cooper pair charge, while the other factor of two is due to the Béri degeneracy of the non-unit Andreev reflection eigenvalues.

4.3 Effect of disorder

While in the quantum Hall effect all plateaus are insensitive to disorder, in the NS junction this applies only to the first plateau. As follows from Eq. (4.3), the first plateau at $G = (1 - Q)(e^2/h)$ is determined by the topological quantum number Q, which is robust against perturbations of the Hamiltonian. No such topological protection applies to the higher

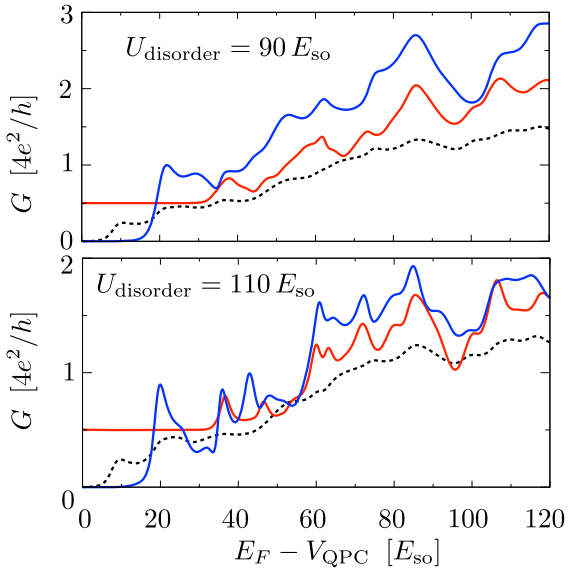

Figure 4.2. Same as Fig. 4.1, but now in the presence of disorder (for two values of the disorder strength). The first conductance plateau in the topologically nontrivial phase remains precisely quantized.

plateaus, since R_n can take on any value between 0 and 1 in the presence of disorder.

This is demonstrated in Fig. 4.2, where we have added disorder to the model calculation (both in the normal and in the superconducting region), by randomly chosing the electrostatic potential at each lattice point from the interval $[-U_{\mathrm{disorder}}, U_{\mathrm{disorder}}]$. The mean free path $l_{\mathrm{mfp}} \propto U_{\mathrm{disorder}}^{-2}$ depends rather sensitively on the disorder strength. We show results for $U_{\mathrm{disorder}} = 90\,E_{\mathrm{so}}$ and $110\,E_{\mathrm{so}}$, when the mean free path (calculated in Born approximation) is estimated at $l_{\mathrm{mfp}} = 9\,l_{\mathrm{so}}$ and $6\,l_{\mathrm{so}}$, respectively. (The topologically nontrivial phase itself persists up to $l_{\mathrm{mfp}} = 3\,l_{\mathrm{so}}$.)

4.4 Effect of finite voltage and temperature

These are all results in the limit of zero applied voltage V and zero temperature T. There is then no qualitative difference between the $2e^2/h$ conductance resonance in the tunneling regime or in the ballistic regime. A substantial difference appears at finite voltages or temperatures.

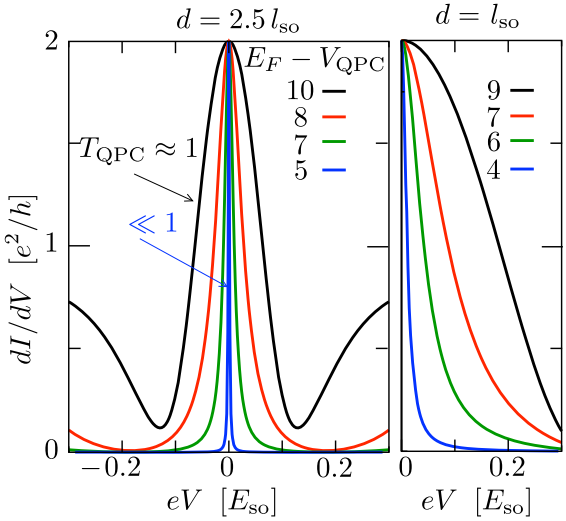

Figure 4.3. Differential conductance at different values of $E_F - V_{\rm QPC}$ (listed in units of $E_{\rm so}$), for two values of the distance d between quantum point contact and superconductor. The data is taken on the first conductance plateau in the topologically nontrivial phase ($\Delta = 4\,E_{\rm so}$, $U_{\rm disorder} = 90\,E_{\rm so}$). The quantum point contact is in the tunneling regime for the blue curve (transmittance $T_{\rm QPC} = 0.1$) and in the single-mode ballistic regime for the black curve ($T_{\rm QPC} \approx 1$). The width of the conductance peak increases both upon increasing $T_{\rm QPC}$ and upon decreasing d.

Considering first the effect of a nonzero applied voltage, we show in Fig. 4.3 the differential conductance

$$\frac{dI}{dV} = \frac{2e^2}{h} \sum_n R_n(E_F + eV). \tag{4.4}$$

The peak centered at $V = 0$ is the signature of the topologically nontrivial phase [9]. The height $2e^2/h$ of this peak remains the same as $T_{\rm QPC}$ is raised from 0 to 1 by opening up the point contact, but the peak width increases. For a given $T_{\rm QPC}$, moving the point contact closer to the superconductor also has the effect of increasing the peak width (right panel in Fig. 4.3).

These considerations apply to the transition from the tunneling regime ($T_{\rm QPC} \ll 1$) to the ballistic regime with a single transmitted mode ($T_{\rm QPC} \approx 1$). If we open the point contact further, a second mode is partially transmitted and at $T_{\rm QPC} \approx 1.3$ the conductance peak switches to a conduc-

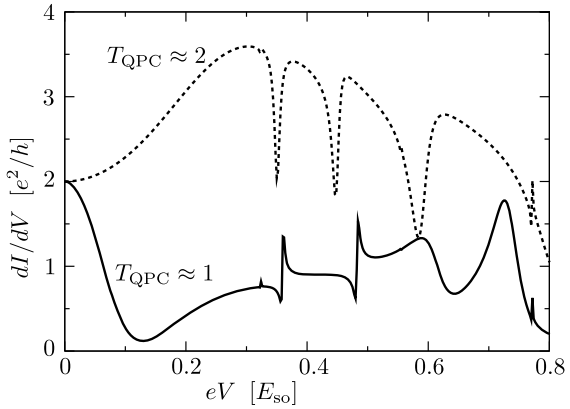

Figure 4.4. The solid curve is the same data as the black curve in the left panel of Fig. 4.3 ($E_F - V_{\rm QPC} = 10\,E_{\rm so}$, $T_{\rm QPC} \approx 1$), but on a larger voltage scale to show the resonances beyond the conductance peak centered at $V = 0$. (The curve is $\pm V$ symmetric.) The dashed curve shows that the conductance peak becomes a conductance dip when a second mode opens up in the quantum point contact ($E_F - V_{\rm QPC} = 20\,E_{\rm so}$, $T_{\rm QPC} \approx 2$).

tance dip. Fig. 4.4 contrasts the inverted resonances at $T_{\rm QCP}$ equal to 1 (conductance peak) and equal to 2 (conductance dip). The voltage scale in this figure is larger than Fig. 4.3, to show also the higher-lying resonances.

A simple estimate for the width $\delta \simeq \hbar/\tau_{\rm dwell}$ of the conductance peak in the tunneling regime equates it to the inverse of the dwell time $\tau_{\rm dwell}$ of an electron (effective mass $m_{\rm eff}$) in the region (of size $W \times d$) between the point contact and the NS interface. For the relatively large mean free paths in the calculation ($l_{\rm mfp} > W, d$), the dwell time for point contact widths $w \ll W, d$ is given by $\tau_{\rm dwell} \simeq m_{\rm eff} W d/\hbar T_{\rm QPC}$, so we estimate

$$\delta \simeq \frac{\hbar^2 T_{\rm QPC}}{m_{\rm eff} W d} = \frac{l_{\rm so}^2}{W d}\, T_{\rm QPC} E_{\rm so}. \tag{4.5}$$

This formula (without numerical prefactors) qualitatively accounts for the increase of δ with decreasing d and with increasing $T_{\rm QPC}$ in the tunneling regime $T_{\rm QPC} \ll 1$, but for a quantitative description of the ballistic regime, including the switch from peak to dip, a more complete theory is needed.

A similarly different robustness in the tunneling and ballistic regime appears if we consider the effect of a nonzero thermal energy $k_B T$ on

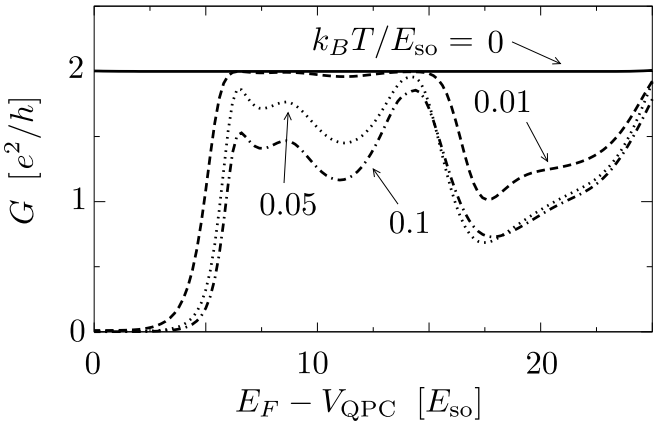

Figure 4.5. Conductance in the topologically nontrivial phase for different values of the thermal energy k_BT. The $2e^2/h$ plateau is suppressed at the smallest temperatures in the tunneling regime, and only for larger temperatures in the ballistic regime.

the $2e^2/h$ conductance plateau. The finite-temperature conductance is calculated from

$$G(k_BT) = \frac{2e^2}{h}\int_{-\infty}^{\infty} dE \sum_n R_n(E)\frac{d}{dE}\frac{-1}{1+e^{E/k_BT}}. \tag{4.6}$$

We show in Fig. 4.5 how raising the temperature suppresses the $2e^2/h$ conductance plateau in the topologically nontrivial phase. The characteristic temperature scale for the suppression is $k_BT \simeq \delta$, so the plateau persists longest for $T_{\rm QPC} \approx 1$, when the line width δ of the resonance is the largest.

4.5 Conclusion

In conclusion, we have presented a model calculation that shows how a quantum point contact can be used to distinguish the topologically trivial and nontrivial phases of a superconducting wire. The $2e^2/h$ conductance resonance in the tunneling regime [9] persists in the ballistic regime, with a greatly reduced sensitivity to finite voltages and temperatures. The characteristic temperature scale (for a typical value $E_{\rm so} = 0.1\,$meV of the spin-orbit coupling energy in InAs) reaches the

100 mK range in the ballistic regime, which is still quite small but within experimental reach.

As more and more modes are opened in the ballistic point contact, new conductance plateaus appear at multiples of $4e^2/h$ which are integer in the trivial and half-integer in the nontrivial phase. This sequence of plateaus is a striking demonstration of the role which the degeneracy of Andreev reflection eigenvalues plays in the classification of topological superconductors [13, 19].

Appendix 4.A Model Hamiltonian

Our model calculations are based on the Hamiltonian of Refs. [14, 15], which describes an InAs nanowire on an Al or Nb substrate.
The Bogoliubov-De Gennes Hamiltonian

$$\begin{aligned}\mathcal{H} &= \begin{pmatrix} 1 & 0 \\ 0 & \sigma_y \end{pmatrix} \begin{pmatrix} H_{\mathrm{R}} - E_F & \Delta \\ \Delta^* & E_F - \sigma_y H_{\mathrm{R}}^* \sigma_y \end{pmatrix} \begin{pmatrix} 1 & 0 \\ 0 & \sigma_y \end{pmatrix} \\ &= \begin{pmatrix} H_{\mathrm{R}} - E_F & \Delta\sigma_y \\ \Delta^*\sigma_y & E_F - H_{\mathrm{R}}^* \end{pmatrix} \end{aligned} \tag{4.7}$$

couples electron and hole excitations near the Fermi energy E_F through an s-wave superconducting order parameter Δ. (We have made a unitary transformation to ensure that the condition for particle-hole symmetry has the form used in App. 4.B.)

The excitations are confined to a wire of width W in the $x-y$ plane of the semiconductor surface inversion layer, where their dynamics is governed by the Rashba Hamiltonian

$$H_{\mathrm{R}} = \frac{\boldsymbol{p}^2}{2m_{\mathrm{eff}}} + U(\boldsymbol{r}) + \frac{\alpha_{\mathrm{so}}}{\hbar}(\sigma_x p_y - \sigma_y p_x) + \tfrac{1}{2} g_{\mathrm{eff}} \mu_B B \sigma_x. \tag{4.8}$$

The spin is coupled to the momentum $\boldsymbol{p} = -i\hbar\partial/\partial\boldsymbol{r}$ by the Rashba effect, and polarized through the Zeeman effect by a magnetic field B parallel to the wire (in the x-direction). Characteristic length and energy scales are $l_{\mathrm{so}} = \hbar^2/m_{\mathrm{eff}}\alpha_{\mathrm{so}}$ and $E_{\mathrm{so}} = m_{\mathrm{eff}}\alpha_{\mathrm{so}}^2/\hbar^2$. Typical values in InAs are $l_{\mathrm{so}} = 100\,\mathrm{nm}$, $E_{\mathrm{so}} = 0.1\,\mathrm{meV}$, $E_Z = \frac{1}{2} g_{\mathrm{eff}} \mu_B B = 1\,\mathrm{meV}$ at $B = 1\,\mathrm{T}$.

The electrostatic potential $U = U_{\mathrm{QPC}} + \delta U$ is the sum of a gate potential U_{QPC} and an impurity potential δU. The impurity potential $\delta U(x, y)$ varies randomly from site to site on a square lattice (lattice constant a), distributed uniformly in the interval $[-U_{\mathrm{disorder}}, U_{\mathrm{disorder}}]$.

The gate potential $U_{\mathrm{QPC}}(x, y)$ (see Fig. 4.6) defines a saddle-shaped constriction of length 2ℓ, containing a potential barrier of height $V_{\mathrm{QPC}} > 0$,

$$\begin{aligned} U_{\mathrm{QPC}} &= \begin{cases} \max\left[0, V_{\mathrm{QPC}} + U_{\mathrm{saddle}}(x, y)\right] & \text{for} |x| > \ell, \\ V_{\mathrm{QPC}} + \frac{1}{2} m_{\mathrm{eff}} \omega_y^2 y^2 & \text{for} |x| < \ell, \end{cases} \\ U_{\mathrm{saddle}} &= -\tfrac{1}{2} m_{\mathrm{eff}} \omega_x^2 (|x| - \ell)^2 + \tfrac{1}{2} m_{\mathrm{eff}} \omega_y^2 y^2. \end{aligned} \tag{4.9}$$

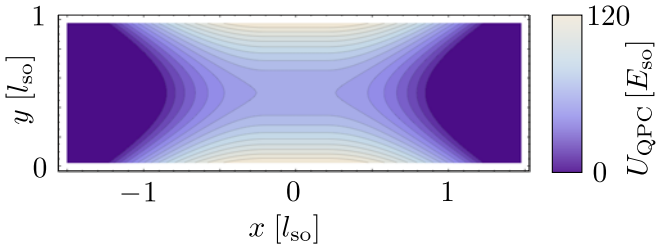

Figure 4.6. Contour plot of the quantum point contact potential (4.9), for the parameters $\ell = 0.2\, l_{\rm so}$, $\hbar\omega_x = 15\, E_{\rm so}$, $\hbar\omega_y = 25\, E_{\rm so}$, $V_{\rm QPC} = 55\, E_{\rm so}$. This is the constriction used in the calculations of the conductance.

The center $(0, 0)$ of the constriction is placed in the normal region at a distance d from the NS interface at $x = d$. The characteristic width w of the constriction at the Fermi energy $E_F > V_{\rm QPC}$ is defined by

$$w = \sqrt{\frac{2(E_F - V_{\rm QPC})}{m_{\rm eff}\omega_y^2}}. \tag{4.10}$$

(This is the separation of classical turning points in the absence of Rashba and Zeeman effects.)

All material parameters have the same value throughout the wire, except the superconducting order parameter Δ, which is set to zero for $x < d$ and $x > L + d$. The length L of the superconducting region if chosen long enough that quasiparticle transmission through it can be neglected (transmission probability $< 10^{-7}$).

Using the algorithm of Ref. [20] we calculate the reflection matrix r of the NS junction, which is unitary in the absence of transmission through the superconductor. Andreev reflection is described by the $N \times N$ subblock r_{he},

$$r = \begin{pmatrix} r_{ee} & r_{eh} \\ r_{he} & r_{hh} \end{pmatrix}. \tag{4.11}$$

The Andreev reflection eigenvalues R_n ($n = 1, 2, \ldots N$) are the eigenvalues of the Hermitian matrix product $r_{he}^\dagger r_{he}$. They are evaluated at the Fermi level for the conductance (4.1) or at an energy eV above the Fermi level for the differential conductance (4.4).

Appendix 4.B Béri degeneracy

We give a self-contained derivation of the degeneracy of the Andreev reflection eigenvalues discovered by Béri [13].

The Hamiltonian (4.7) satisfies the particle-hole symmetry relation

$$\begin{pmatrix} 0 & 1 \\ 1 & 0 \end{pmatrix} \mathcal{H}^* \begin{pmatrix} 0 & 1 \\ 1 & 0 \end{pmatrix} = -\mathcal{H}. \tag{4.12}$$

For the reflection matrix $r(\varepsilon)$ at energy ε (relative to the Fermi level) this implies

$$\begin{pmatrix} 0 & 1 \\ 1 & 0 \end{pmatrix} r(\varepsilon)^* \begin{pmatrix} 0 & 1 \\ 1 & 0 \end{pmatrix} = r(-\varepsilon). \tag{4.13}$$

At the Fermi level ($\varepsilon = 0$) the electron and hole subblocks in Eq. (4.11) are therefore related by

$$r_{hh} = r_{ee}^*, \quad r_{eh} = r_{he}^*. \tag{4.14}$$

Unitarity $r^\dagger r = 1$ requires that $r_{eh}^\dagger r_{ee} + r_{hh}^\dagger r_{he} = 0$, hence at the Fermi level

$$A \equiv r_{ee}^{\mathrm{T}} r_{he} = -A^{\mathrm{T}} \tag{4.15}$$

is an antisymmetric matrix. (The superscript T denotes the transpose.) The Hermitian matrix product

$$A^\dagger A = r_{he}^\dagger r_{he} - (r_{he}^\dagger r_{he})^2 \tag{4.16}$$

has eigenvalues $a_n = R_n(1 - R_n)$, $n = 1, 2, \ldots N$.

Let Ψ be an eigenvector of $A^\dagger A$ with (real, non-negative) eigenvalue a, so $A^\dagger A \Psi = a\Psi$. Then $\Psi' = (A\Psi)^*$ satisfies $A^\dagger A \Psi' = -A^* A A^* \Psi^* = A^*(A^\dagger A \Psi)^* = (aA\Psi)^* = a\Psi'$. The eigenvalue a is therefore twofold degenerate, unless Ψ' and Ψ are linearly dependent.

If $\Psi' = \lambda\Psi$ for some λ, then $a\Psi = A^\dagger A \Psi = -A^*(\lambda\Psi)^* = -|\lambda|^2\Psi$, hence $a = 0$. So any nonzero eigenvalue $R_n(1 - R_n)$ of $A^\dagger A$ is twofold degenerate, which implies that the Andreev reflection eigenvalues R_n are either twofold degenerate or equal to 0 or 1.

Notice that the Béri degeneracy is distinct from the familiar Kramers degeneracy (although the proof goes along similar lines [21]). Kramers degeneracy is a consequence of an anti-unitary symmetry which squares to -1. The particle-hole symmetry operation

$$\mathcal{O}_{\mathrm{ph}} = \begin{pmatrix} 0 & 1 \\ 1 & 0 \end{pmatrix} \times \text{complex conjugation} \tag{4.17}$$

is anti-unitary, but squares to $+1$.

In the absence of time-reversal and spin-rotation symmetry, only the Béri degeneracy of the Andreev reflection eigenvalues is operative. This is the case for the model Hamiltonian (4.7) considered here (with time-reversal symmetry broken by the Zeeman effect and spin-rotation symmetry broken by the Rashba effect). As worked out in Ref. [19], if one or both of these symmetries are present, then all R_n's are twofold degenerate — including those equal to 0 or 1. The Kramers degeneracy then comes in the place of the Béri degeneracy, it is not an additional degeneracy.

Bibliography

[1] J.W. McClure, Phys. Rev. **104**, 666 (1956).

[2] K.S. Novoselov , A.K. Geim, S.V. Morozov, D. Jiang, M.I. Katsnelson, I.V. Grigorieva, S.V. Dubonos, and A.A. Firsov, Nature **438**, 197 (2005).

[3] Y. Zhang, Y.W. Tan, H.L. Stormer, and P. Kim, Nature **438**, 201 (2005).

[4] R. Jackiw and P. Rossi, Nucl. Phys. B **190**, 681 (1981).

[5] L. Fu and C.L. Kane, Phys. Rev. Lett. **100**, 096407 (2008).

[6] M.Z. Hasan and C.L. Kane, Rev. Mod. Phys. **82**, 3045 (2010).

[7] X.-L. Qi and S.-C. Zhang, Rev. Mod. Phys. **83**, 1057 (2011).

[8] C.J. Bolech and E. Demler, Phys. Rev. Lett. **98**, 237002 (2007).

[9] K.T. Law, P.A. Lee, and T.K. Ng, Phys. Rev. Lett. **103**, 237001 (2009).

[10] K. Flensberg, Phys. Rev. B **82**, 180516(R) (2010).

[11] M. Leijnse and K. Flensberg, Phys. Rev. B **84**, 140501(R) (2011)

[12] B. Béri, J.N. Kupferschmidt, C.W.J. Beenakker, and P.W. Brouwer, Phys. Rev. B **79**, 024517 (2009).

[13] B. Béri, Phys. Rev. B **79**, 245315 (2009).

[14] R.M. Lutchyn, J.D. Sau, and S. Das Sarma, Phys. Rev. Lett. **105**, 077001 (2010).

[15] Y. Oreg, G. Refael, and F. von Oppen, Phys. Rev. Lett. **105**, 177002 (2010).

[16] F. Merz and J.T. Chalker, Phys. Rev. B **65**, 054425 (2002).

[17] A.R. Akhmerov, J.P. Dahlhaus, F. Hassler, M. Wimmer and C.W.J. Beenakker, Phys. Rev. Lett. **106**, 057001 (2011).

[18] I.C. Fulga, F. Hassler, A.R. Akhmerov, and C.W.J. Beenakker, Phys. Rev. B **83**, 155429 (2011).

[19] C.W.J. Beenakker, J.P. Dahlhaus, M. Wimmer, and A.R. Akhmerov, Phys. Rev. B **83** 085413 (2011).

[20] M. Wimmer and K. Richter, J. Comput. Phys. **228**, 8548 (2009).

[21] J.H. Bardarson, J. Phys. A **41**, 405203 (2008).

Chapter 5

Scattering theory of topological invariants in nodal superconductors

5.1 Introduction

The topological classification of superconductors relies on the existence of an excitation gap in the bulk of the material, that prevents transitions between topologically distinct phases [1, 2]. The gap of a topological superconductor closes only at the boundary, where propagating states with a linear dispersion appear. The protected boundary states are counted by a topological invariant $\mathcal{Q}$, expressed either in terms of the Hamiltonian of an infinite system [3] or in terms of the scattering matrix for Andreev reflection from the boundary with a normal metal [4].

Nodal superconductors with time-reversal symmetry also have boundary states, forming flat bands in the middle of the bulk gap [5]. The same topological considerations do not apply because the gap vanishes in the bulk for certain momenta $\boldsymbol{k}$ on the Fermi surface (nodal points). Examples include the cuprate superconductors (gap $\propto k_x k_y$) [6], and a variety of superconductors without inversion symmetry [7]. Nodal superconductors may also appear as an intermediate phase in the transition from a topological superconductor to a trivial one [8, 9].

A topological invariant can still be constructed in a nodal superconductor for a translationally invariant boundary [10, 11], conserving the

parallel momentum $\boldsymbol{k}_\parallel$. The value of $\mathcal{Q}(\boldsymbol{k}_\parallel)$ can only change if $\boldsymbol{k}_\parallel$ crosses a nodal point. This topological invariant again counts the boundary states, which are now non-propagating dispersionless states (pinned to $E = 0$ for a range of $\boldsymbol{k}_\parallel$).

In Refs. 10, 11 the topological invariant $\mathcal{Q}(\boldsymbol{k}_\parallel)$ of a nodal superconductor takes the form of a winding number, calculated from the Hamiltonian of a translationally invariant infinite system. Here we present an alternative scattering formulation, which expresses $\mathcal{Q}(\boldsymbol{k}_\parallel)$ as a trace of the Andreev reflection matrix. Since the conductance of a normal-metal–superconductor (NS) interface is expressed in terms of the same Andreev reflection matrix, this alternative formulation allows for a direct connection between the topological invariant and a transport property.

If the NS interface contains a tunnel barrier, the angle-resolved conductance $G(\boldsymbol{k}_\parallel)$ measures the density of states and directly probes the flat surface bands as a zero-bias peak [12]. For a transparent interface the boundary states in the superconductor merge with the continuum in the metal, resulting in a featureless density of states, but the zero-bias peak remains [13]. Here we relate the height of this zero-bias peak to the value of the topological invariant. While in general this relation takes the form of an inequality, a quantized conductance,

$$G(\boldsymbol{k}_\parallel) = |\mathcal{Q}(\boldsymbol{k}_\parallel)| \times 2e^2/h, \tag{5.1}$$

may result under certain conditions which we identify.

The outline of this chapter is as follows. In the next section we formulate the scattering problem and construct the topological invariant from the Andreev reflection matrix. We make contact in Sec. 5.3 with the Hamiltonian formulation, by closing the system and showing that we recover the number of flat bands at the boundary. We then return to the open system and in Sec. 5.4 relate the angle-resolved zero-bias conductance to the topological invariant. So far we only assumed the basic symmetries of time-reversal and charge-conjugation. The effects of additional unitary symmetries are considered in Sec. 5.5. We apply the general theory to a model of a two-dimensional (2D) nodal superconductor in Secs. 5.6 and 5.7, including also the effects of disorder. Effects that are specific to 3D are discussed in Sec. 5.8. We conclude in Sec. 5.9.

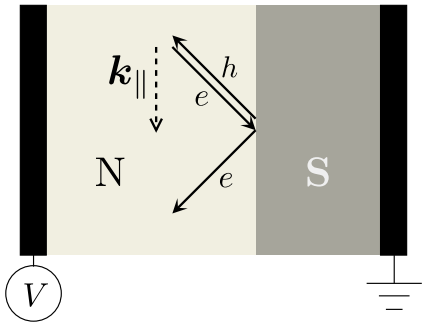

Figure 5.1. Interface between a superconductor (S) and a normal metal (N). The reflection matrix $r(k_\parallel)$ relates the amplitudes of the incident and reflected waves (arrows, both normal reflection and Andreev reflection are indicated). The conductance of the NS interface is measured by applying a voltage difference V between the normal metal and the grounded superconductor.

5.2 Topological invariant for Andreev reflection

5.2.1 Chiral symmetry

We study the Andreev reflection of electrons and holes at the Fermi level from a planar interface between a normal metal (N) and a superconductor (S). (See Fig. 5.1.) The component $k_\parallel$ along the interface of the momentum k is conserved, so we can consider each $k_\parallel$ separately and work with a one-dimensional (1D) reflection matrix $r(k_\parallel)$. For k not in a nodal direction (nonzero excitation gap) this is a unitary matrix,

$$r(k_\parallel)r^\dagger(k_\parallel) = 1. \tag{5.2}$$

The dimension of the reflection matrix is 4×4, with basis states $(\psi_{e\uparrow}, \psi_{e\downarrow}, \psi_{h\uparrow}, \psi_{h\downarrow})$ labeled by the spin $\uparrow, \downarrow$ and the electron-hole e, h degrees of freedom. The e, h grading produces four 2×2 submatrices,

$$r(k_\parallel) = \begin{pmatrix} r_{ee}(k_\parallel) & r_{eh}(k_\parallel) \\ r_{he}(k_\parallel) & r_{hh}(k_\parallel) \end{pmatrix}. \tag{5.3}$$

Normal reflection (from electron to electron or from hole to hole) is described by r_{ee} and r_{hh}, while r_{he} and r_{eh} describe Andreev reflection (from electron to hole or the other way around).

The two fundamental symmetries that we impose are time-reversal and charge-conjugation symmetry. Time-reversal symmetry requires

$$r(k_\parallel) = \sigma_y r^{\mathrm{T}}(-k_\parallel)\sigma_y, \tag{5.4}$$

while charge-conjugation symmetry at the Fermi level requires

$$r(\boldsymbol{k}_\parallel) = \tau_x r^*(-\boldsymbol{k}_\parallel)\tau_x. \tag{5.5}$$

The Pauli matrices σ_i and τ_i act on, respectively, the spin and electron-hole degrees of freedom. (For later use we denote the 2×2 unit matrices by σ_0 and τ_0.)

Taken together, Eqs. (5.4) and (5.5) represent the chiral symmetry relation

$$r(\boldsymbol{k}_\parallel) = (\sigma_y \otimes \tau_x) r^\dagger(\boldsymbol{k}_\parallel)(\sigma_y \otimes \tau_x). \tag{5.6}$$

This is the 1D symmetry class AIII in the periodic table of topological phases [3].

It is convenient to represent the symmetry relations in terms of the matrix $R(\boldsymbol{k}_\parallel) = (\sigma_y \otimes \tau_x) r(\boldsymbol{k}_\parallel)$, which is both Hermitian and unitary,

$$R = R^\dagger, \quad R^2 = 1. \tag{5.7}$$

The submatrices in Eq. (5.3) appear in R as

$$R(\boldsymbol{k}_\parallel) = \begin{pmatrix} R_{he}(\boldsymbol{k}_\parallel) & R_{hh}(\boldsymbol{k}_\parallel) \\ R_{ee}(\boldsymbol{k}_\parallel) & R_{eh}(\boldsymbol{k}_\parallel) \end{pmatrix}, \tag{5.8}$$

where $R_{pq} = \sigma_y r_{pq}$. The two blocks R_{he} and R_{eh} are Hermitian, while $R_{ee} = R_{hh}^\dagger$.

5.2.2 Topological invariant

The $\mathbb{Z}$ topological invariant of 1D reflection matrices in class AIII is given by [14]

$$\begin{aligned} \mathcal{Q}(\boldsymbol{k}_\parallel) &= \tfrac{1}{2} \operatorname{Tr} R(\boldsymbol{k}_\parallel) \\ &= \tfrac{1}{2} \operatorname{Tr} \sigma_y [r_{he}(\boldsymbol{k}_\parallel) + r_{eh}(\boldsymbol{k}_\parallel)]. \end{aligned} \tag{5.9}$$

In view of Eq. (5.7), the 4×4 matrix R has eigenvalues ± 1, so the value of $\mathcal{Q} \in \{-2, -1, 0, 1, 2\}$.[1] This value is $\boldsymbol{k}_\parallel$-independent as long as the reflection matrix remains unitary. For $\boldsymbol{k}$ in a nodal direction, the reflection matrix is sub-unitary and the topological invariant may change.

[1] The topological invariant $\mathcal{Q}$ is restricted to the integers $0, \pm 1, \pm 2$ because we consider only spin and electron-hole degrees of freedom. Further integer values become possible if multiple valleys or layers produce additional internal degrees of freedom, which is why $\mathcal{Q}$ is a called a $\mathbb{Z}$ invariant.

Application of Eq. (5.4) gives the relation

$$R(-\boldsymbol{k}_\parallel) = -\tau_x R^{\mathrm{T}}(\boldsymbol{k}_\parallel)\tau_x, \tag{5.10}$$

which implies that

$$\mathcal{Q}(-\boldsymbol{k}_\parallel) = -\mathcal{Q}(\boldsymbol{k}_\parallel). \tag{5.11}$$

If $\boldsymbol{k}_\parallel = 0$ one necessarily has $\mathcal{Q} = 0$. For this time-reversally invariant momentum the Pfaffian of the antisymmetric matrix $\sigma_y r(0)$ (equal to ± 1) produces a $\mathbb{Z}_2$ topological invariant [14], characteristic of the 1D symmetry class DIII. We write this invariant in the form

$$\mathcal{Q}_0 = 1 + \mathrm{Pf}\,\sigma_y r(0) \in \{0, 2\}, \tag{5.12}$$

so that for $\mathcal{Q}_0$, as well as for $\mathcal{Q}$, the value 0 indicates the topologically trivial phase.

5.3 Topologically protected boundary states

The scattering formulation of topological invariants refers to an open system, without bound states. In the alternative Hamiltonian formulation, the topological invariant counts the number of dispersionless boundary states (flat bands at the Fermi level, consisting of edge states in 2D or surface states in 3D) [10, 11, 15–18]. To relate the two formulations, we close the system by means of an insulating barrier at the NS interface, and show that $|\mathcal{Q}(\boldsymbol{k}_\parallel)|$ boundary states appear.

The calculation closely follows Ref. 14. The number of boundary states at $\boldsymbol{k}_\parallel$ equals the number of independent solutions ψ of

$$\left[1 - r_1(\boldsymbol{k}_\parallel) r(\boldsymbol{k}_\parallel)\right]\psi = 0. \tag{5.13}$$

The unitary matrix r_1 is the reflection matrix of the barrier, approached from the side of the superconductor. We can write this equation in terms of Hermitian and unitary matrices $R_1 = r_1(\sigma_y \otimes \tau_x)$ and $R_2 = (\sigma_y \otimes \tau_x) r$, which we decompose as

$$R_i = U_i D_i U_i^\dagger, \quad D_i = \begin{pmatrix} \mathbb{1}_{2+\mathcal{Q}_i} & 0 \\ 0 & -\mathbb{1}_{2-\mathcal{Q}_i} \end{pmatrix}. \tag{5.14}$$

(The notation $\mathbb{1}_M$ indicates the $M \times M$ unit matrix and U_1, U_2 are unitary matrices.) Eq. (5.13) takes the form

$$(1 - D_1 U D_2 U^\dagger)\psi' = 0, \tag{5.15}$$

with $U = U_1^\dagger U_2$ and $\psi' = U_1^\dagger \psi$.

We decompose U into $N \times M$ submatrices $A_{N,M}$,

$$U = \begin{pmatrix} A_{2+\mathcal{Q}_1,2+\mathcal{Q}_2} & A_{2+\mathcal{Q}_1,2-\mathcal{Q}_2} \\ A_{2-\mathcal{Q}_1,2+\mathcal{Q}_2} & A_{2-\mathcal{Q}_1,2-\mathcal{Q}_2} \end{pmatrix}. \tag{5.16}$$

Since

$$U - D_1 U D_2 = 2 \begin{pmatrix} 0 & A_{2+\mathcal{Q}_1,2-\mathcal{Q}_2} \\ A_{2-\mathcal{Q}_1,2+\mathcal{Q}_2} & 0 \end{pmatrix}, \tag{5.17}$$

we can rewrite Eq. (5.15) as

$$\begin{pmatrix} 0 & A_{2+\mathcal{Q}_1,2-\mathcal{Q}_2} \\ A_{2-\mathcal{Q}_1,2+\mathcal{Q}_2} & 0 \end{pmatrix} \psi'' = 0, \tag{5.18}$$

with $\psi'' = U_2^\dagger \psi$.

For any matrix $A_{N,M}$ with $N < M$ there exist at least $M - N$ independent vectors $\boldsymbol{v}$ of rank M such that $A_{N,M}\boldsymbol{v} = 0$. Therefore Eq. (5.18) has at least $|\mathcal{Q}_1 + \mathcal{Q}_2|$ independent solutions. These are the topologically protected boundary states.

Because the insulating barrier is topologically trivial, $\mathcal{Q}_1 = 0$, while $\mathcal{Q}_2 = \mathcal{Q}$ is the topological invariant of the superconductor, so it all works out as expected: The topological invariant of the open system counts the number of boundary states that would appear if we would close it.

Both values $\mathcal{Q}$ and $-\mathcal{Q}$ of the topological invariant produce the same number $\mathcal{N} = |\mathcal{Q}|$ of boundary states if the superconductor is terminated by a topologically trivial barrier (an insulator or vacuum). The sign of the topological invariant matters if we consider the interface between two topologically nontrivial superconductors 1, 2. The combined number of boundary states $\mathcal{N}_{\text{total}} = |\mathcal{Q}_1 + \mathcal{Q}_2| = |\mathcal{N}_1 \pm \mathcal{N}_2|$ is the sum or difference of the individual numbers depending on whether the topological invariants have the same or opposite sign.

5.4 Relation between conductance and topological invariant

By considering an open system when formulating the topological invariant, we can make direct contact to transport properties. The angle-resolved zero-bias conductance of the NS interface is given by

$$G(\boldsymbol{k}_\parallel) = G_0 \operatorname{Tr} r_{he}(\boldsymbol{k}_\parallel) r_{he}^\dagger(\boldsymbol{k}_\parallel), \tag{5.19}$$

with $G_0 = 2e^2/h$ the Andreev conductance quantum. We wish to relate this transport property to the topological invariant (5.9).

For that purpose it is convenient to work with the matrices $R_{he} = \sigma_y r_{he}$ and $R_{eh} = \sigma_y r_{eh}$, since these are Hermitian (unlike the r_{he} and r_{eh} themselves). For brevity we omit the label $\boldsymbol{k}_\parallel$. The squares R_{he}^2 and R_{eh}^2 have the same set of Andreev reflection eigenvalues $\rho_n \in [0, 1]$, which are also the eigenvalues of $r_{he} r_{he}^\dagger$.

On the one hand we have the conductance

$$G/G_0 = \mathrm{Tr}\, R_{he}^2 = \mathrm{Tr}\, R_{eh}^2, \tag{5.20}$$

and on the other hand the topological invariant

$$\mathcal{Q} = \tfrac{1}{2}\,\mathrm{Tr}\,(R_{he} + R_{eh}). \tag{5.21}$$

In App. 5.A we prove that at least $|\mathcal{Q}|$ of the ρ_n's are equal to unity. This immediately implies the inequality

$$G/G_0 \geq |\mathcal{Q}|. \tag{5.22}$$

For $\boldsymbol{k}_\parallel = 0$ we have, additionally,

$$G/G_0 \geq \mathcal{Q}_0, \quad \text{for} \quad \boldsymbol{k}_\parallel = 0. \tag{5.23}$$

In a topologically trivial system, with $\mathcal{Q}, \mathcal{Q}_0 = 0$, these inequalities are ineffective, while for $|\mathcal{Q}|, \mathcal{Q}_0 = 2$ the inequalities are saturated (since G cannot become larger than $2G_0$). Scattering events in the normal or superconducting region that conserve $\boldsymbol{k}_\parallel$, such as spin mixing, cannot change the conductance once it is saturated.

5.5 Effects of additional unitary symmetries

Further unitary symmetries may enforce restrictions on both the topological invariant and the angle-resolved conductance, or even introduce new topological invariants. In the first subsection we consider spatial symmetries that invert $\boldsymbol{k}_\parallel \mapsto -\boldsymbol{k}_\parallel$, whereas in the second subsection we address symmetries that conserve $\boldsymbol{k}_\parallel$.

a, b	x, x or z, x or $0, y$	$x, 0$ or $z, 0$ or y, z	x, z or y, x or z, z or $y, 0$	y, y or $0, z$	x, y or z, y or $0, x$	$0, 0$
$\mathcal{T}_{ab}^2$	$+1$	$+1$	$+1$	-1	-1	-1
$\mathcal{C}_{ab}^2$	$+1$	$+1$	-1	-1	$+1$	$+1$
class	BDI	BDI	CI	CII	DIII	DIII
$\mathcal{Q}_{ab}$	$0, \pm 1, \pm 2$	$0, \pm 1, \pm 2$	0	$0, \pm 2$	$0, 2$	$0, 2$
G/G_0	$\geq \lvert\mathcal{Q}_{ab}\rvert$	$= \lvert\mathcal{Q}_{ab}\rvert$	$\times$	$= \lvert\mathcal{Q}_{ab}\rvert$	$\times$	$= \lvert\mathcal{Q}_{ab}\rvert$

Table 5.1. The first row lists the spatial symmetry (5.24); the second and third rows give the square of the anti-unitary operators (5.25) and (5.26); the fourth and fifth rows show the corresponding symmetry class and the values taken by the topological invariant; finally, the last row gives the relation between conductance and invariant for a topologically *nontrivial* system (so for $\mathcal{Q}_{ab} \neq 0$, with $\times$ indicating the absence of a relation).

5.5.1 Spatial symmetries

We consider a spatial symmetry of the form

$$r(\boldsymbol{k}_\parallel) = (\sigma_a \otimes \tau_b) r(-\boldsymbol{k}_\parallel)(\sigma_a \otimes \tau_b). \tag{5.24}$$

Combined with time-reversal symmetry (5.4) and charge-conjugation symmetry (5.5), this produces the two symmetry relations

$$r(\boldsymbol{k}_\parallel) = \mathcal{T}_{ab} r^\dagger(\boldsymbol{k}_\parallel) \mathcal{T}_{ab}^{-1}, \quad \mathcal{T}_{ab} = (\sigma_a \cdot \sigma_y) \otimes \tau_b \mathcal{K}, \tag{5.25}$$

$$r(\boldsymbol{k}_\parallel) = \mathcal{C}_{ab} r(\boldsymbol{k}_\parallel) \mathcal{C}_{ab}^{-1}, \quad \mathcal{C}_{ab} = \sigma_a \otimes (\tau_b \cdot \tau_x)\mathcal{K}, \tag{5.26}$$

where $\mathcal{K}$ is the operator of complex conjugation. The product of $\mathcal{T}_{ab}$ and $\mathcal{C}_{ab}$ brings us back to the chiral symmetry (5.6).

Topological invariant

Depending on whether the anti-unitary operators $\mathcal{T}_{ab}$ and $\mathcal{C}_{ab}$ square to $+1$ or -1, the reflection matrix falls in one of the four Altland-Zirnbauer symmetry classes BDI, CI, CII, DIII [19]. The various cases are listed in Table 5.1. These all have a higher symmetry than the class AIII from which we started (with only chiral symmetry). The additional symmetry may restrict the topological invariant to a smaller range of values. In class DIII a new $\mathbb{Z}_2$ topological invariant appears, that can be nonzero even if the $\mathbb{Z}$ invariant vanishes.

We denote the modified topological invariant by $\mathcal{Q}_{ab}(\boldsymbol{k}_\parallel)$. In class CI only topologically trivial systems exist [3], meaning that the spatial

symmetry allows only for $\mathcal{Q}_{ab} = 0$. For the other three symmetry classes the topological invariants are given by [14]

$$\mathcal{Q}_{ab} = \tfrac{1}{2} \operatorname{Tr} R \in \{-2, -1, 0, 1, 2\}, \quad \text{for BDI,} \tag{5.27}$$

$$\mathcal{Q}_{ab} = \tfrac{1}{2} \operatorname{Tr} R \in \{-2, 0, 2\}, \quad \text{for CII,} \tag{5.28}$$

$$\mathcal{Q}_{ab} = 1 + \operatorname{Pf}(\sigma_a \otimes \tau_b)(\sigma_y r) \in \{0, 2\}, \quad \text{for DIII.} \tag{5.29}$$

The restriction to even integers in class CII (a $2\mathbb{Z}$ invariant) is a consequence of the Kramers degeneracy of the eigenvalues of the Hermitian matrix $R = (\sigma_y \otimes \tau_x)r$. Symmetry class DIII has a $\mathbb{Z}_2$ invariant.

Conductance

The expressions (5.27) and (5.28) for $\mathcal{Q}_{ab}$ in class BDI and CII are the same as the expression (5.9) for $\mathcal{Q}$ in class AIII, so the topological invariant still provides a lower bound on the angle-resolved conductance,

$$G/G_0 \geq |\mathcal{Q}_{ab}|, \quad \text{for BDI and CII.} \tag{5.30}$$

In symmetry class DIII the invariants $\mathcal{Q}_{00}$ in Eq. (5.29) and $\mathcal{Q}_0$ in Eq. (5.12) also have the same expression, so the inequality (5.23) still applies,

$$G/G_0 \geq \mathcal{Q}_{00}. \tag{5.31}$$

No relation with the conductance exists for the other invariants in class DIII, so $\mathcal{Q}_{0x}$, $\mathcal{Q}_{xy}$, and $\mathcal{Q}_{zy}$ provide no restriction on the conductance.[2]

The inequality (5.30) can be sharpened further in class BDI, so that it becomes an equality not only for $|\mathcal{Q}_{ab}| = 2$ but also for $|\mathcal{Q}_{ab}| = 1$ [20]. As we show in App. 5.C, this equality is enforced by the spatial symmetry (5.24) for $(a, b) \in \{(y, z), (x, 0), (z, 0)\}$, so for three out of the six symmetries in class BDI.

The last row of Table 5.1 summarizes the relation between the topological invariant and the conductance for a topologically nontrivial system ($\mathcal{Q}_{ab} \neq 0$). It is an equality for all symmetries in class CII and for some symmetries in classes BDI and DIII.

[2] To see that $\mathcal{Q}_{0x} = 1 + \operatorname{Pf} R$ is independent of G, note that the transformation $R \mapsto ORO$ with $O = \operatorname{diag}(1, 1, 1, -1)$ switches the sign of the Pfaffian — while leaving the conductance unchanged. In a similar way one can show that also the DIII invariants $\mathcal{Q}_{xy}$ and $\mathcal{Q}_{zy}$ are independent of G.

5.5.2 Symmetries that preserve $k_\parallel$

A different type of unitary symmetry preserves parallel momentum,

$$r(\boldsymbol{k}_\parallel) = (\sigma_a \otimes \tau_b) r(\boldsymbol{k}_\parallel)(\sigma_a \otimes \tau_b). \tag{5.32}$$

Combined with the chiral symmetry relation (5.6) and unitarity of r, this symmetry ensures that the matrix $\tilde{R} = (\sigma_a \otimes \tau_b)R$ is a unitary matrix that squares to ± 1. We can thus define a new $\mathbb{Z}$ invariant

$$\tilde{\mathcal{Q}}(\boldsymbol{k}_\parallel) = \begin{cases} \frac{1}{2} \operatorname{Tr} \tilde{R}(\boldsymbol{k}_\parallel) & \text{if } \tilde{R}^2 = 1, \\ \frac{1}{2} i \operatorname{Tr} \tilde{R}(\boldsymbol{k}_\parallel) & \text{if } \tilde{R}^2 = -1. \end{cases} \tag{5.33}$$

In general, $\tilde{\mathcal{Q}}$ and $\mathcal{Q}$ are distinct, and in particular $\tilde{\mathcal{Q}}$ can be an even function of $\boldsymbol{k}_\parallel$. The coexistence of two distinct topological invariants is quite unusual, and as we will see, it has observable consequences in the conductance.

For $b \in \{0, z\}$ nonzero values of $\tilde{\mathcal{Q}}$ constrain the conductance in the same way that $\mathcal{Q}$ does in Eq. (5.22). For $b \in \{x, y\}$ one has instead the constraint

$$G/G_0 \leq 2 - |\tilde{\mathcal{Q}}|, \tag{5.34}$$

as we show in App. 5.B.

5.6 Application: 2D Rashba superconductor

As a first application of our general scattering theory we consider a two-dimensional superconductor with spin-singlet and spin-triplet pairing mixed by Rashba spin-orbit coupling. The topologically protected edge states for this Rashba superconductor have been studied in Refs. 10, 21, 22 using the Hamiltonian formulation. We summarize those results in the next subsection, before proceeding to the scattering formulation and the calculation of the conductance.

5.6.1 Hamiltonian and edge states

The superconductor has the Bogoliubov-de Gennes Hamiltonian

$$H(\boldsymbol{k}) = \begin{pmatrix} \epsilon(\boldsymbol{k}) + \boldsymbol{g}(\boldsymbol{k}) \cdot \boldsymbol{\sigma} & \Delta(\boldsymbol{k}) \\ \Delta^\dagger(\boldsymbol{k}) & -\epsilon(\boldsymbol{k}) + \boldsymbol{g}(\boldsymbol{k}) \cdot \boldsymbol{\sigma}^* \end{pmatrix}, \tag{5.35}$$

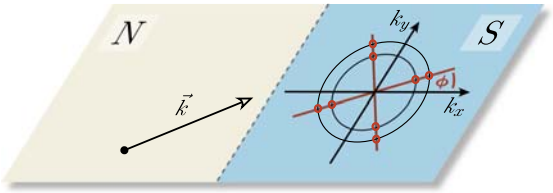

Figure 5.2. Interface between a normal metal and a 2D Rashba superconductor. The Fermi surface is split into two circles, which intersect the nodal lines (red) of the superconducting pair potential in eight nodal points.

with free electron part $\epsilon(\boldsymbol{k}) = |\boldsymbol{k}|^2/2m - \mu$, at Fermi energy μ, and Rashba spin-orbit coupling $\boldsymbol{g}(\boldsymbol{k}) = \lambda(k_y, -k_x, 0)$. We have set $\hbar = 1$ and have collected the three Pauli matrices in a vector $\boldsymbol{\sigma} = (\sigma_x, \sigma_y, \sigma_z)$. The Fermi surface consists of two concentric circles at momenta

$$k_\pm = [(m\lambda)^2 + 2m\mu]^{1/2} \pm m\lambda. \tag{5.36}$$

For later use we give the spin orbit energy $E_{\rm so} = m\lambda^2$ and the spin-orbit momentum and length $k_{\rm so} = m\lambda = 1/l_{\rm so}$.

The mixed singlet-triplet pair potential is given by

$$\Delta(\boldsymbol{k}) = f(\boldsymbol{k}) \left(\Delta_{\rm s} + \Delta_{\rm t} \frac{\boldsymbol{g}(\boldsymbol{k}) \cdot \boldsymbol{\sigma}}{\lambda(2m\mu)^{1/2}} \right) i\sigma_y, \tag{5.37}$$

$$f(\boldsymbol{k}) = \frac{1}{2m\mu} \left[k_x k_y \cos 2\phi + \tfrac{1}{2}(k_y^2 - k_x^2) \sin 2\phi \right], \tag{5.38}$$

The strength of the singlet and triplet pairing is parameterized by the energies $\Delta_{\rm s}$ and $\Delta_{\rm t}$. The nodal lines of vanishing pair potential are oriented at an angle ϕ with the NS interface (see Fig. 5.2). The intersection of the nodal lines with the Fermi surface defines 8 nodal points, in each of which $\mathrm{Det}\, H = 0$.

The chiral symmetry

$$H(\boldsymbol{k}) = -(\sigma_y \otimes \tau_x) H(\boldsymbol{k}) (\sigma_y \otimes \tau_x) \tag{5.39}$$

ensures that H can be brought in the off-diagonal form

$$\mathcal{U}^\dagger H(\boldsymbol{k}) \mathcal{U} = \begin{pmatrix} 0 & q(\boldsymbol{k}) \\ q^\dagger(\boldsymbol{k}) & 0 \end{pmatrix}. \tag{5.40}$$

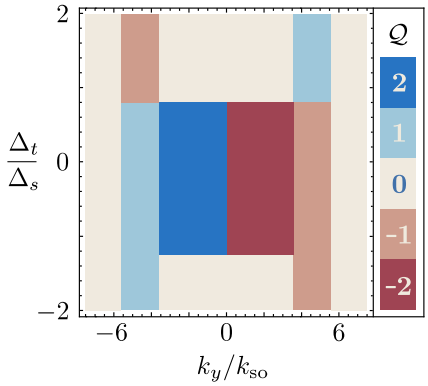

Figure 5.3. Topological invariant $\mathcal{Q} = -\mathcal{W}$ of the 2D Rashba superconductor ($\phi = 0$, $\mu = 10\, E_{\rm so}$), as a function of momentum k_y along the NS interface and ratio $\Delta_{\rm t}/\Delta_{\rm s}$ of triplet and singlet pairing energies.

The $\mathbb{Z}$ topological invariant is then defined by the winding number [10]

$$\mathcal{W}(k_y) = \frac{1}{2\pi}\mathrm{Im}\int dk_x\, \frac{\partial}{\partial k_x} \ln \mathrm{Det}\, q(k_x, k_y), \tag{5.41}$$

for any k_y that is not equal to the projection of one of the nodal points on the y-axis.

As analysed in Refs. 10, 21, 22, the termination of the superconductor at $x = 0$ by an insulator (or by vacuum) produces $|\mathcal{W}(k_y)|$ dispersionless edge states (flat bands). A simple example occurs for $\phi = 0$ and $\Delta_{\rm t} = 0$, corresponding to d_{xy}-wave spin-singlet pairing. Then

$$\mathcal{W}(k_y) = \begin{cases} 2\,\mathrm{sign}\,(k_y) & \text{if } |k_y| < k_-, \\ \mathrm{sign}\,(k_y) & \text{if } k_- < |k_y| < k_+, \\ 0 & \text{if } |k_y| > k_+, \end{cases} \tag{5.42}$$

so there are two topologically protected edge states for $|k_y| < k_-$ and a single one for $k_- < |k_y| < k_+$.

For nonzero $\Delta_{\rm t}$ the phase boundaries (5.42) remain unaffected in the interval

$$-\sqrt{2m\mu}/k_- < \Delta_{\rm t}/\Delta_{\rm s} < \sqrt{2m\mu}/k_+,$$

see Fig. 5.3. To contrast the spin-singlet and spin-triplet dominated regimes, we will in what follows focus on the two limits $\Delta_{\rm t} \to 0$ and $\Delta_{\rm s} \to 0$.

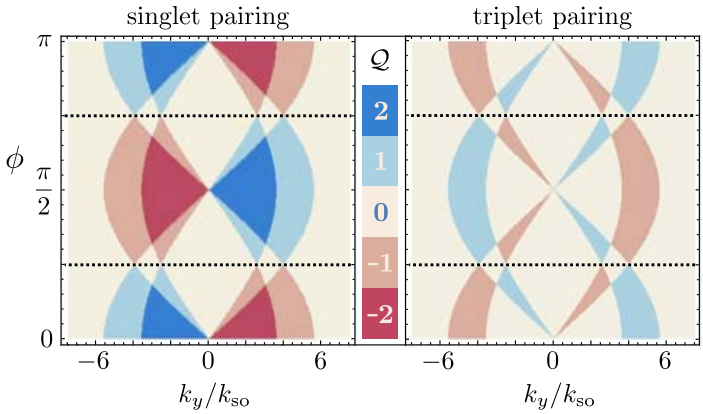

Figure 5.4. Topological invariant $\mathcal{Q}$ of the reflection matrix from the 2D Rashba superconductor, as a function of momentum k_y along the NS interface and angle ϕ between the interface and the nodal line. The left panel shows results for spin-singlet pairing ($\Delta_{\mathrm{s}} = E_{\mathrm{so}}$, $\Delta_{\mathrm{t}} = 0$) and the right panel for spin-triplet pairing ($\Delta_{\mathrm{t}} = E_{\mathrm{so}}$, $\Delta_{\mathrm{s}} = 0$). In both panels $\mu = 10\,E_{\mathrm{so}}$ and $\mu_{\mathrm{N}} = 30\,E_{\mathrm{so}}$. The dotted lines indicate a topologically trivial system in class CI, as a consequence of the spatial symmetry (5.43).

5.6.2 Reflection matrix and conductance

If the superconductor is not terminated at $x = 0$ but connected to a normal metal, the edge states hybridize with the continuum of the metallic bands. The topological signature then shows up in the conductance rather than in the density of states. To reveal these signatures we construct the reflection matrix of the NS interface and calculate both the topological invariant (5.9) and the angle-resolved conductance (5.19).

We used either an analytical method of calculation (matching wave functions at the NS interface), or a numerical method (discretizing the Hamiltonian (5.35) on a square lattice and calculating the Green function). We made sure that the lattice constant was sufficiently small that the two methods gave equivalent results. In the normal metal we set both the pair potential and the spin-orbit coupling to zero, so that there is a single Fermi circle with momentum $k_{\mathrm{N}} = (2m\mu_{\mathrm{N}})^{1/2}$. Because of a potential step at the NS interface, the chemical potential μ_{N} in the normal metal ($x < 0$) can differ from the value μ in the superconductor ($x > 0$).

Results are collected in Figs. 5.4 and 5.5. As a first check, we note

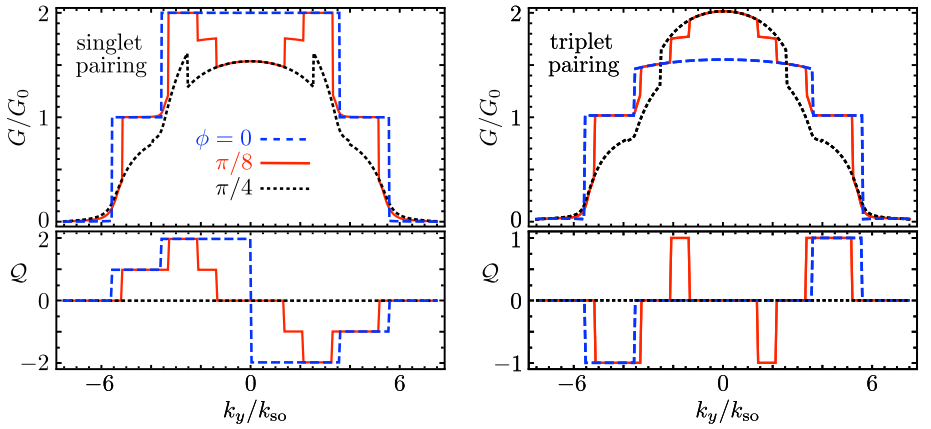

Figure 5.5. Electrical conductance and $\mathbb{Z}$ topological invariant for three of the angles ϕ from Fig. 5.4. A nonzero $\mathbb{Z}_2$ invariant appears in the spin-triplet case: $\mathcal{Q}_0 = 2$ for $k_y = 0$, $\phi \neq 0$.

that for $\phi = 0$, $\Delta_t = 0$, we recover Eq. (5.42) — up to an irrelevant minus sign, $\mathcal{Q} = -\mathcal{W}$. For $\phi = (n + 1/2)\pi/2$, the system is topologically trivial, $\mathcal{Q}(k_y) \equiv 0$, regardless of the choice of Δ_s, Δ_t (black dotted lines in Figs. 5.4 and 5.5). This can be understood as a consequence of spatial symmetry: For $\cos 2\phi = 0$ the system fulfills

$$H(k_x, k_y) = \sigma_y H(k_x, -k_y)\sigma_y \Rightarrow r(k_y) = \sigma_y r(-k_y)\sigma_y. \tag{5.43}$$

This is a symmetry condition of the type (5.24), with $a = y, b = 0$, forcing the reflection matrix into the topologically trivial symmetry class CI (see Table 5.1). At $k_y = 0$ the $\mathbb{Z}$ invariant $\mathcal{Q}$ vanishes, but the $\mathbb{Z}_2$ invariant $\mathcal{Q}_0$ can be nonzero. This happens for $\Delta_s = 0$, $\phi \neq 0 \pmod{\pi/2}$, when $\mathcal{Q}_0 = 2$.

Fig. 5.5 shows how the topological invariant enforces the quantization of the angle-resolved conductance. First of all, $G/G_0 = 2$ whenever $|\mathcal{Q}| = 2$ or $\mathcal{Q}_0 = 2$. For $\phi = 0$ quantized plateaus at $G/G_0 = 1$ appear because of the spatial symmetry

$$r(k_y) = (\sigma_y \otimes \tau_z) r(-k_y)(\sigma_y \otimes \tau_z), \tag{5.44}$$

which is a symmetry of the type (5.24) with $a, b = y, z$. This forces the reflection matrix into class BDI and ensures that the conductance is quantized for any nonzero $\mathcal{Q}$ (see Table 5.1).

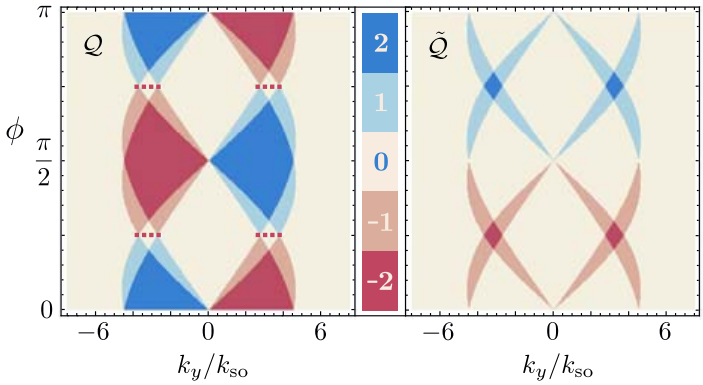

Figure 5.6. Topological invariants $\mathcal{Q}$ (left panel) and $\tilde{\mathcal{Q}}$ (right panel) for an NS junction between a normal metal and the anisotropic Rashba superconductor of Sec. 5.6.3. The parameters chosen are: $\Delta_{\rm s} = E_{\rm so}$, $\Delta_{\rm t} = 0$, $\mu = 10\,E_{\rm so}$, $\mu_{\rm N} = 30\,E_{\rm so}$. The $\mathbb{Z}_2$ invariant $\mathcal{Q}_{00} = 2$ on the dotted red lines in the left panel.

5.6.3 Anisotropic spin-orbit coupling

A strongly anisotropic dispersion, $m_x \gg m_y$, can produce an anisotropic spin-orbit coupling term of the form [23] $\boldsymbol{g}(\boldsymbol{k}) = \lambda(0, -k_x, 0)$. Topological invariants and conductance are plotted for the spin-singlet regime ($\Delta_{\rm t} = 0$) in Figs. 5.6 and 5.7. There are two qualitative differences with the isotropic case of the previous subsections.

First of all, for $\phi = n\pi/2$ the regions with $|\mathcal{Q}(k_y)| = 1$ are missing. This can be explained by the spatial symmetry

$$r(k_y) = \tau_z r(-k_y)\tau_z, \tag{5.45}$$

of the type (5.24) with $a, b = 0, z$. As a consequence, see Table 5.1, the topological invariant $\mathcal{Q}(k_y)$ becomes a $2\mathbb{Z}$ invariant of class CII, excluding $|\mathcal{Q}(k_y)| = 1$.

Secondly, there is a unitary symmetry $\sigma_y r(k_y)\sigma_y = r(k_y)$ that holds for all ϕ. This allows us to define an additional topological invariant,

$$\tilde{\mathcal{Q}} = \tfrac{1}{2}\mathrm{Tr}\,\sigma_y R = \tfrac{1}{2}\mathrm{Tr}\,\tau_x r, \tag{5.46}$$

following Sec. 5.5.2. The topological invariants $\mathcal{Q}$ and $\tilde{\mathcal{Q}}$ are independent, in particular, $\tilde{\mathcal{Q}}(k_y) = \tilde{\mathcal{Q}}(-k_y)$ while $\mathcal{Q}(k_y) = -\mathcal{Q}(-k_y)$. Each topological invariant $\mathcal{Q}$ and $\tilde{\mathcal{Q}}$ gives a lower bound on the conductance.

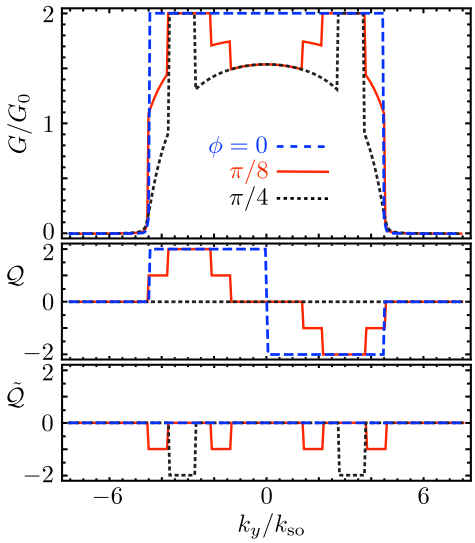

Figure 5.7. Electrical conductance and $\mathbb{Z}$ topological invariants for three of the angles ϕ from Fig. 5.6.

This explains the diamond-shaped regions in the phase diagram with a quantized conductance $G/G_0 = 2$, enforced by $|\tilde{\mathcal{Q}}| = 2$.

There is a third invariant: At $\phi = (n + 1/2)\pi/2$ the spatial symmetry $r(k_y) = r(-k_y)$ places the reflection matrix in symmetry class DIII. According to Eq. (5.29), the corresponding $\mathbb{Z}_2$ invariant $\mathcal{Q}_{00} = 2$ on the dotted red lines in the phase diagram.

This third invariant does not lead to additional constraints on the conductance, since we already have $\tilde{\mathcal{Q}} = 2$ when $\mathcal{Q}_{00} = 2$. But the two invariants $\mathcal{Q}$ and $\tilde{\mathcal{Q}}$ are both needed to explain the quantized conductance. The coexistence of two topological invariants is an unusual feature of this system.

5.7 Effects of angular averaging and disorder

It may be possible to measure the angle-resolved conductance $G(\boldsymbol{k}_\parallel)$ [24], but one typically measures the angular average. Moreover, disorder is detrimental for the conductance quantization if it mixes parallel momenta with different values of the topological invariant. In this section we investigate whether signatures of the conductance quantization

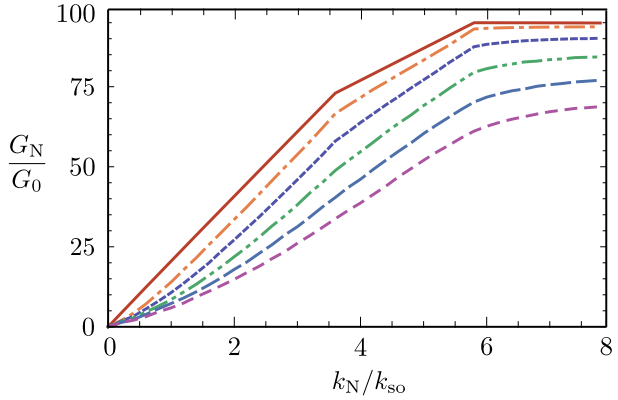

Figure 5.8. Average conductance (5.47) of the NS junction as a function of the Fermi momentum k_N in the normal region, for various disorder strengths. The 2D Rashba superconductor has a d_{xy}-wave pair potential ($\phi = 0$, $\Delta_t = 0$, $\Delta_s = E_{so}$, $\mu = 10\,E_{so}$). Disorder strengths from top to bottom curve: $U_0/E_{so} = 0, 1, 2, 3, 4, 5$.

can survive the effects of angular averaging and disorder.

We focus on the 2D Rashba superconductor of Sec. 5.6, for $\Delta_t = 0$, $\phi = 0$, when the topological invariant is given by Eq. (5.42). The angular average of the conductance for an interface of width W is given by

$$G_{NS} = \frac{W}{2\pi} \int_{-k_N}^{k_N} dk_y\, G(k_y). \tag{5.47}$$

The reflection matrix, which determines $G(k_y)$ via Eq. (5.19), is calculated numerically using the square lattice discretization of the Hamiltonian (5.35) (lattice constant $a = 0.2\,l_{so}$, $W = 32\,l_{so}$). Disorder is added to a strip $-L < x < 0$ ($L = 31.6\,l_{so}$) of the normal region by means of a random on-site potential, distributed uniformly in $(-U_0/2, U_0/2)$. Results are averaged over 100 disorder realizations.

In Fig. 5.8 we show the dependence of G_{NS} on the Fermi momentum k_N in the normal region. This is relevant if the normal region is a semiconductor, where one can vary k_N by a gate voltage. The quantization of $G(k_y)$ manifests itself as a quantized slope of G_{NS} versus k_N: the steep slope for $k_N < k_-$ (where $|\mathcal{Q}| = 2$) is reduced by a factor of two in the interval $k_- < k_N < k_+$ (where $|\mathcal{Q}| = 1$), and then is strongly suppressed for $k_N > k_+$. This signature of the topological invariant gradually disappears with increasing disorder.

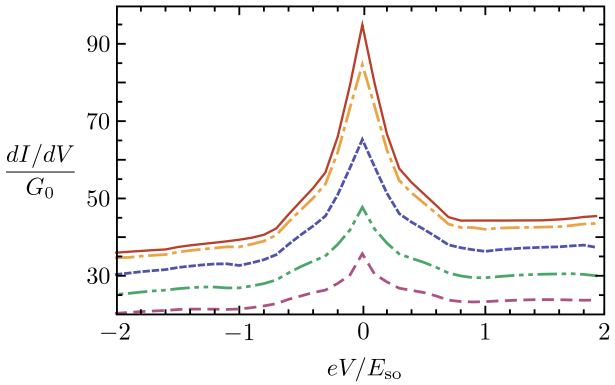

Figure 5.9. Differential conductance of the NS junction for various disorder strengths. The parameters for the superconductor are the same as in Fig. 5.8. In the normal region we have fixed $\mu_{\mathrm{N}} = 25\,E_{\mathrm{so}}$. Disorder strengths from top to bottom curve: $U_0/E_{\mathrm{so}} = 0, 2.5, 5, 7.5, 10$.

Another signature can be seen for fixed k_{N} in the dependence of the differential conductance dI/dV on the applied voltage V. As shown in Fig. 5.9, the peak in dI/dV around $V = 0$ is a superposition of two peaks with different widths, the narrower one originating from parallel momenta in the $|\mathcal{Q}| = 2$ regions and the broader one from the $|\mathcal{Q}| = 1$ regions. The single edge state of the latter regions couples more strongly to the continuum of the metal and thus has a larger width.

5.8 Three-dimensional superconductors

5.8.1 Topological invariant for arc surface states

The topological invariants considered so far, and the resulting constraints on the angle-resolved conductance, apply both to 2D and 3D nodal superconductors. In this section we discuss features that are specific for 3D superconductors. The topological invariant $\mathcal{Q}(\boldsymbol{k}_\parallel)$ of Sec. 5.2.2 then counts dispersionless surface states, pinned to zero energy (the Fermi level) in a 2D region of parallel momentum $\boldsymbol{k}_\parallel = (k_1, k_2)$. The boundary of this flat band region is formed by nodal rings, closed contours of $\boldsymbol{k}_\parallel$ on which transmission through the superconductor is possible — in other words, the superconducting gap vanishes for $\boldsymbol{k} = (k_\perp, \boldsymbol{k}_\parallel)$.

The new feature that appears in a 3D superconductor is the possibil-

ity of zero-energy boundary states along a 1D arc connecting two nodal rings. Some aspects of their topological nature have been discussed in the Hamiltonian formulation of Ref. 18. Here we consider the alternative scattering formulation, and use it to obtain topological constraints on the conductance.

We consider a spatial symmetry on the 2D surface of a 3D superconductor, in which only one of the two components of parallel momentum is inverted:

$$r(k_1, k_2) = (\sigma_a \otimes \tau_b) r(-k_1, k_2)(\sigma_a \otimes \tau_b). \tag{5.48}$$

Along the line $k_2 = 0$, this is a symmetry of the type (5.24), so we can follow Sec. 5.5.1 to introduce topological invariants $\mathcal{Q}_{ab}(k_1)$. The resulting constraints on the angle-resolved conductance $G(k_1, 0)$ are summarized in Table 5.1.

Alternatively, for $k_1 = 0$, the symmetry (5.48) is of the type (5.32) with topological invariant $\tilde{\mathcal{Q}}(k_2)$ from Eq. (5.33). The corresponding constraints on the conductance are discussed in Sec. 5.5.2.

5.8.2 Example

As an example, we apply these general considerations to the same Rashba Hamiltonian (5.35), but now with a 3D dispersion,

$$\epsilon(\boldsymbol{k}) = (k_x^2 + k_y^2 + k_z^2)/2m - \mu. \tag{5.49}$$

In the pair potential (5.37) we set $f(\boldsymbol{k}) \equiv 1$. This Hamiltonian applies to non-centrosymmetric s+p-wave superconductors of point group C_{4v}. As described in Ref. 18, these superconductors have arc surface states connecting two nodal rings. They appear for example for the (011) surface orientation that we will consider in the following. The two components of parallel momentum on the surface are $k_1 = k_x$ and $k_2 = (k_y - k_z)/\sqrt{2}$.

We can obtain two topological invariants from the reflection matrix $r(k_1, k_2)$, plotted in the left panel of Fig. 5.10. The first invariant

$$\mathcal{Q}(k_1, k_2) = \tfrac{1}{2}\mathrm{Tr}\, R(k_1, k_2) = \tfrac{1}{2}\mathrm{Tr}\,(\sigma_y \otimes \tau_x) r(k_1, k_2) \tag{5.50}$$

follows from chiral symmetry, see Sec. 5.2, and is defined on the entire 2D plane of parallel momenta. This $\mathbb{Z}$ invariant is nonzero inside the regions bounded by the nodal rings, where it identifies a surface flat band.

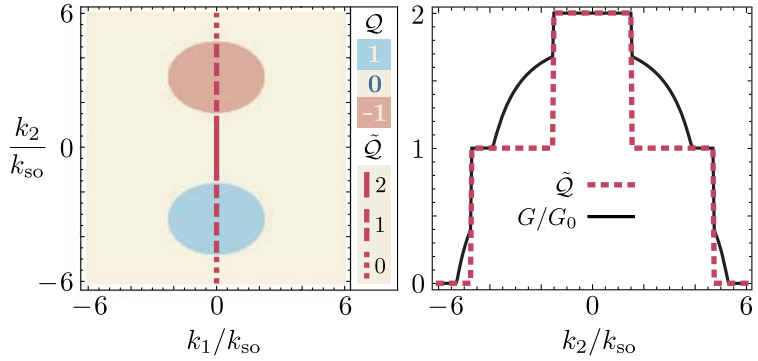

Figure 5.10. Topological invariants and electrical conductance of an NS junction between a normal metal and an s+p-wave superconductor of point group C_{4v}. The invariants $\mathcal{Q}$ and $\tilde{\mathcal{Q}}$ are plotted in the left panel. The right panel shows the conductance (black curve) and invariant $\tilde{\mathcal{Q}}$ (red dotted curve) along the line $k_1 = 0$. Parameters chosen are $\Delta_s = 0.1\,E_{so}$, $\Delta_t = 0.2\,E_{so}$, $\mu = 10\,E_{so}$ and $\mu_N = 30\,E_{so}$.

A second $\mathbb{Z}$ invariant appears as a consequence of the spatial symmetry

$$\begin{aligned} H(k_x, k_y, k_z) &= (\sigma_x \otimes \tau_z) H(-k_x, k_y, k_z)(\sigma_x \otimes \tau_z) \Rightarrow \\ r(k_1, k_2) &= (\sigma_x \otimes \tau_z) r(-k_1, k_2)(\sigma_x \otimes \tau_z). \end{aligned} \tag{5.51}$$

The line $k_1 = 0$ connects the two nodal rings and on this line the invariant

$$\tilde{\mathcal{Q}}(k_2) = \tfrac{1}{2}\mathrm{Tr}\,(\sigma_x \otimes \tau_z) R(0, k_2) = -\tfrac{1}{2}\mathrm{Tr}\,(\sigma_z \otimes \tau_y) r(0, k_2) \tag{5.52}$$

can take on a nonzero value.

The non-trivial invariants enforce a lower bound on the conductance, as is illustrated in the right panel of Fig. 5.10. This leads to a quantized conductance $G/G_0 = 2$ along the line $k_1 = 0$.

The symmetry (5.51) produces arc surface states on all surfaces parallel to the x-direction. For the (010) surface analyzed in Ref. 18 there is an additional spatial symmetry, $r(k_x, k_z) = r(k_x, -k_z)$. For $k_x = 0$ this additional symmetry allows for the $\mathbb{Z}_2$ invariant $\mathcal{Q}_{00} = 1 + \mathrm{Pf}\,\sigma_y r(0, k_z)$, in addition to the $\mathbb{Z}$ invariant (5.52). For other surface orientations $(0nm)$ only the $\mathbb{Z}$ invariant is responsible for the arc states.

5.9 Conclusion

In conclusion, we have constructed a topological invariant $\mathcal{Q}(\boldsymbol{k}_\parallel)$ of the Andreev reflection matrix at the interface between a time-reversal symmetric nodal superconductor and a normal metal. In the absence of a tunnel barrier, this interface has no zero-energy boundary states, but the topologically nontrivial phase can still be detected in the angle-resolved conductance $G(\boldsymbol{k}_\parallel)$. A variety of symmetry classes can be realized (AIII, BDI, CI, CII, DIII), by allowing for additional unitary symmetries. The corresponding topological invariants are given by a trace or Pfaffian of the reflection matrix.

Many of these topological invariants have been studied before in the Hamiltonian formulation for an infinite system [10, 11, 15–18]. The scattering formulation presented here makes it possible to directly relate $\mathcal{Q}(\boldsymbol{k}_\parallel)$ to $G(\boldsymbol{k}_\parallel)$. We have systematically examined when a nontrivial topological invariant enforces a quantized conductance, and when it only provides a lower bound. This approach can identify surface flat bands (within nodal rings) as well as arc states (connecting nodal rings), even when these zero-energy boundary states have merged with the continuum of states in the normal metal.

We have applied the general theory to 2D and 3D superconductors with spin-singlet and spin-triplet pairing mixed by Rashba spin-orbit coupling. The appearance of a quantized conductance has allowed us to verify known topological invariants and to identify new ones. In particular, in the 2D case of a strongly anisotropic spin-orbit coupling, we have shown the coexistence of two topological invariants — which provide independent constraints on the conductance.

To make contact with experiments, the effects of angular averaging and impurity scattering on the conductance quantization have been investigated by numerical simulation of a disordered NS interface.

Appendix 5.A Topological invariant counts number of unit Andreev reflection eigenvalues

5.A.1 Proof for the $\mathbb{Z}$ invariant

The Hermitian matrix R_{eh}^2 has eigenvalues $\rho_n \in [0,1]$. We wish to prove that at least $|\mathcal{Q}|$ of these Andreev reflection eigenvalues are equal to unity.

Let ϕ be an eigenvector of R_{eh} with eigenvalue λ. Assume $\lambda \neq \pm 1$ (so $\rho = \lambda^2 < 1$). Since $R_{eh}^2 = 1 - R_{hh}^\dagger R_{hh}$, the vector $\phi' = R_{hh}\phi$ cannot vanish. Since $R_{he}R_{hh} = -R_{hh}R_{eh}$, it then follows that ϕ' is an eigenvector of R_{he} with eigenvalue $\mu = -\lambda$.

Now consider the $\mathbb{Z}$ topological invariant $\mathcal{Q} = \frac{1}{2}\sum_n(\lambda_n + \mu_n)$ in symmetry class AIII. The eigenvalues $\lambda_n \neq \pm 1$ of R_{eh} are cancelled by an eigenvalue $\mu_n = -\lambda_n$ of R_{he}. The cancellation can only be avoided for the M eigenvalues λ_n equal to ± 1, resulting in $|\mathcal{Q}| \leq M$ — as we set out to prove.

5.A.2 Proof for the $\mathbb{Z}_2$ invariant

For any 4×4 antisymmetric matrix A with a block structure,

$$A = \begin{pmatrix} A_{11} & A_{12} \\ A_{21} & A_{22} \end{pmatrix} = -A^{\mathrm{T}}, \tag{5.53}$$

the Pfaffian is given by

$$\mathrm{Pf}\, A = -\mathrm{Det}\, A_{12} - \tfrac{1}{2}\,\mathrm{Tr}\, A_{11}A_{22}. \tag{5.54}$$

We apply this identity to the antisymmetric matrix $\sigma_y r$ at $\boldsymbol{k}_\parallel = 0$, to obtain the $\mathbb{Z}_2$ topological invariant in symmetry class DIII,

$$\begin{aligned} \mathcal{Q}_0 &= 1 - \mathrm{Det}\, R_{eh} - \tfrac{1}{2}\,\mathrm{Tr}\, R_{ee}R_{hh} \\ &= 1 - \mathrm{Det}\, R_{eh} - \tfrac{1}{2}\,\mathrm{Tr}\,(1 - R_{eh}^2). \end{aligned} \tag{5.55}$$

In terms of the two eigenvalues $\lambda_1, \lambda_2 \in [-1,1]$ of R_{eh} this reduces to

$$\mathcal{Q}_0 = \tfrac{1}{2}(\lambda_1 - \lambda_2)^2. \tag{5.56}$$

Since by construction $\mathcal{Q}_0$ equals either 0 or 2, we have either $\mathcal{Q}_0 = 0 \Leftrightarrow \lambda_1 = \lambda_2$ or $\mathcal{Q}_0 = 2 \Leftrightarrow \lambda_1 = -\lambda_2 = \pm 1$. This shows that at least $\mathcal{Q}_0$ of the Andreev reflection eigenvalues $\rho_n = \lambda_n^2$ are equal to unity.

Appendix 5.B Proof of Eq. (5.34)

We consider the topological invariant (5.33), constructed from the matrix $\tilde{R} = (\sigma_a \otimes \tau_b)R$ with $b \in \{x, y\}$, and wish to proof the constraint (5.34) on the conductance. This amounts to a proof that at least $|\tilde{\mathcal{Q}}|$ of the Andreev reflection eigenvalues are equal to zero.

We define the Hermitian matrix

$$\bar{R} = \begin{pmatrix} \bar{R}_{ee} & \bar{R}_{eh} \\ \bar{R}_{he} & \bar{R}_{hh} \end{pmatrix} \equiv \begin{cases} \tilde{R}(\boldsymbol{k}_\parallel) & \text{if } \tilde{R}^2 = 1, \\ i\tilde{R}(\boldsymbol{k}_\parallel) & \text{if } \tilde{R}^2 = -1. \end{cases} \tag{5.57}$$

Let ϕ be an eigenvector of $\bar{R}_{ee}$ with eigenvalue λ. Assume $\lambda \neq \pm 1$. Since $\bar{R}_{ee}^2 = 1 - \bar{R}_{he}^\dagger \bar{R}_{he}$, the vector $\phi' = \bar{R}_{he}\phi$ cannot vanish. With $\bar{R}_{he}\bar{R}_{ee} = -\bar{R}_{hh}\bar{R}_{he}$, it then follows that ϕ' is an eigenvector of $\bar{R}_{hh}$ with eigenvalue $\mu = -\lambda$.

Now since $\tilde{\mathcal{Q}} = \frac{1}{2}\operatorname{Tr}(\bar{R}_{ee} + \bar{R}_{hh}) = \frac{1}{2}\sum_n(\lambda_n + \mu_n)$, the eigenvalues $\lambda_n \neq \pm 1$ of R_{ee} are cancelled by eigenvalues $\mu_n = -\lambda_n$ of R_{hh} in the expression for the topological invariant. The cancellation can only be avoided for the M eigenvalues λ_n equal to ± 1, resulting in $|\tilde{\mathcal{Q}}| \leq M$. The existence of at least $|\tilde{\mathcal{Q}}|$ unit eigenvalues of $\bar{R}_{ee}^\dagger \bar{R}_{ee} = \bar{R}_{ee}^2$ is equivalent to the existence of at least $|\tilde{\mathcal{Q}}|$ zero Andreev reflection eigenvalues and thereby proves Eq. (5.34).

Appendix 5.C Equality of conductance and topological invariant in class BDI

A topologically nontrivial 4×4 reflection matrix in class BDI has either $|\mathcal{Q}_{ab}| = 2$ or $|\mathcal{Q}_{ab}| = 1$. In the former case the inequality (5.30) is saturated, because $G/G_0 \leq 2$, but in the latter case it provides only a lower bound on the conductance. We now wish to show that the inequality can be sharpened to an equality for three of the six spatial symmetries (5.24) in class BDI. More precisely, we will show that $|\mathcal{Q}_{ab}| = 1$ implies $G/G_0 = 1$ for $(a, b) \in \{(y, z), (x, 0), (z, 0)\}$.

For each of these three cases the symmetry relation (5.25) implies that $R_{he} = \sigma_a R_{eh}^{\mathrm{T}} \sigma_a$, so $\operatorname{Tr} R_{he} = \operatorname{Tr} R_{eh}$. Denote the eigenvalues of R_{eh} and R_{he} by λ_1, λ_2 and μ_1, μ_2, respectively. (All are real numbers in the interval $[-1, 1]$.) The equality of the traces gives $\lambda_1 + \lambda_2 = \mu_1 + \mu_2$. The topological invariant (5.27) determines the sum $\lambda_1 + \lambda_2 + \mu_1 + \mu_2 = 2\mathcal{Q}_{ab}$, hence $\lambda_1 + \lambda_2 = \mathcal{Q}_{ab}$.

Because classes BDI and AIII have the same expression for the topological invariant, we may apply the result of App. 5.A.1 that at least $|\mathcal{Q}_{ab}|$ of the λ_n's equal ± 1. If we take $|\mathcal{Q}_{ab}| = 1$, $|\lambda_1| = 1$, then necessarily $\lambda_2 = 0$. The dimensionless conductance $G/G_0 = \lambda_1^2 + \lambda_2^2$ thus equals unity, as we set out to prove.

Our finding can be seen in a broader context as a manifestation of Béri degeneracy of Andreev reflection eigenvalues [25]: the charge-conjugation symmetry (5.26), with $(a, b) \in \{(y, z), (x, 0), (z, 0)\}$, enforces a twofold degeneracy of the Andreev reflection eigenvalues $\rho_n = \lambda_n^2$ that can only be avoided if ρ_n equals 0 or 1.

Bibliography

[1] M. Z. Hasan and C. L. Kane, Rev. Mod. Phys. **82**, 3045 (2010).

[2] X.-L. Qi and S.-C. Zhang, Rev. Mod. Phys. **83**, 1057 (2011).

[3] S. Ryu, A. Schnyder, A. Furusaki, and A. Ludwig, New J. Phys. **12**, 065010 (2010).

[4] I. C. Fulga, F. Hassler, and A. R. Akhmerov, Phys. Rev. B **85**, 165409 (2012).

[5] S. Kashiwaya and Y. Tanaka, Rep. Prog. Phys. **63**, 1641 (2000).

[6] C. C. Tsuei and J. R. Kirtley, Rev. Mod. Phys. **72**, 969 (2000).

[7] E. Bauer and M. Sigrist, *Non-Centrosymmetric Superconductors* (Springer, Berlin, 2012).

[8] B. Béri, Phys. Rev. B **81**, 134515 (2010).

[9] A. P. Schnyder, P. M. R. Brydon, D. Manske, and C. Timm, Phys. Rev. B **82**, 184508 (2010).

[10] M. Sato, Y. Tanaka, K. Yada, and T. Yokoyama, Phys. Rev. B **83**, 224511 (2011).

[11] A. P. Schnyder and S. Ryu, Phys. Rev. B **84**, 060504(R) (2011).

[12] M. Eschrig, C. Iniotakis, and Y. Tanaka, Lect. Notes Phys. **847**, 313 (2012) [arXiv:1001.2486].

[13] K. Sengupta, I. Žutić, H.-J. Kwon, V. M. Yakovenko, and S. Das Sarma, Phys. Rev. B **63**, 144531 (2001).

[14] I. C. Fulga, F. Hassler, A. R. Akhmerov, and C. W. J. Beenakker, Phys. Rev. B **83**, 155429 (2011).

[15] M. Sato, Phys. Rev. B **73**, 214502 (2006).

[16] Y. Tanaka, T. Yokoyama, A. V. Balatsky, and N. Nagaosa, Phys. Rev. B **79**, 060505(R) (2009).

[17] P. M. R. Brydon, A. P. Schnyder, and C. Timm, Phys. Rev. B **84**, 020501(R) (2011).

[18] A. P. Schnyder, P. M. R. Brydon, and C. Timm, Phys. Rev. B **85**, 024522 (2012).

[19] A. Altland and M. R. Zirnbauer, Phys. Rev. B **55**, 1142 (1997).

[20] M. Diez, J. P. Dahlhaus, M. Wimmer, and C. W. J. Beenakker, Phys. Rev. B **86**, 094501 (2012).

[21] Y. Tanaka, Y. Mizuno, T. Yokoyama, K. Yada, and M. Sato, Phys. Rev. Lett. **105**, 097002 (2010).

[22] K. Yada, M. Sato, Y. Tanaka, and T. Yokoyama, Phys. Rev. B **83**, 064505 (2011).

[23] J. Alicea, Phys. Rev. B **81**, 125318 (2011).

[24] N. A. Mortensen, K. Flensberg, and A.-P. Jauho, Phys. Rev. B **59**, 10176 (1999).

[25] B. Béri, Phys. Rev. B **79**, 245315 (2009).

Chapter 6

Quantum Hall effect in a one-dimensional dynamical system

6.1 Introduction

The disorder-induced localization-delocalization transition in the quantum Hall effect is the oldest and best-known example of a topological phase transition [1, 2]. The transition is called topological because it is associated with a change in a topological invariant, the Chern number, which counts the number of edge states and the quantized value of the Hall conductance [3]. Since there is still no analytical theory for the quantum Hall phase transition, computer simulations are needed to calculate the scaling law and critical exponent associated with the diverging localization length at the transition. The two-dimensional (2D) network model of Chalker and Coddington has been the primary tool for these studies for more than two decades [4–6].

In this chapter we introduce an alternative *one-dimensional* (1D) model of the quantum Hall phase transition. The model is stroboscopic, with a Hamiltonian that is driven quasiperiodically with two incommensurate driving frequencies. It is a variation on the quantum kicked rotator [7–9], used to study the 3D Anderson metal-insulator transition of atomic matter waves in a 1D optical lattice [10–14]. Stroboscopic models of quantum phase transitions have received much attention recently [15–20], but the dimensional reduction considered here has not yet been

explored.

Usually the quantum Hall effect is due to the quantization of cyclotron orbits in Landau levels. It is possible to simulate a Lorentz force acting on neutral atoms in a 2D optical lattice [21–23], but in a 1D lattice we need a quantum Hall effect without Landau levels [24]. This socalled quantum *anomalous* Hall effect appears in the Qi-Wu-Zhang (QWZ) model of a spin-1/2 coupled to orbit and to a uniform magnetization. While the topological invariant in this model takes on only the three values $0, \pm 1$, the phase transitions are in the same $\mathbb{Z}$ universality class as the usual quantum Hall effect.

In the next two sections we formulate the stroboscopic model of the quantum Hall effect, first in 2D (Sec. 6.2) and then reduced to 1D (Sec. 6.3). We obtain the model by starting from the QWZ Hamiltonian, but we also show how it is related to the quantum kicked rotator (upon exchange of position and momentum).

In Sec. 6.4 we perform numerical simulations of the spreading of a 1D wave packet to identify the localization-delocalization transitions. While the translationally invariant QWZ model has three quantum Hall transitions, we find four transitions because one is split by disorder. We verify one-parameter scaling of the time-dependent diffusion coefficient and calculate the critical exponent. The result is consistent with the most accurate value obtained from the Chalker-Coddington model [6].

To further support that these are topological phase transitions in the quantum Hall universality class we calculate the Hall conductance as well as the $\mathbb{Z}$ topological invariant in Sec. 6.5. We conclude by discussing the possibilities for the realization of the quantum Hall effect in a 1D optical lattice.

6.2 Formulation of the 2D stroboscopic model

6.2.1 Quantum anomalous Hall effect

In this subsection we summarize the QWZ model [25] of the quantum anomalous Hall effect, on which we base the stroboscopic model described in the next subsection.

The QWZ model describes two spin bands of a magnetic insulator on a two-dimensional (2D) square lattice. The crystal momentum $\boldsymbol{p} = (p_1, p_2)$ varies over the Brillouin zone $-\pi\hbar/a < p_1, p_2 < \pi\hbar/a$. The

Hamiltonian has the form $\boldsymbol{u}\cdot\boldsymbol{\sigma}$, with $\boldsymbol{\sigma}=(\sigma_x,\sigma_y,\sigma_z)$ a vector of Pauli matrices and

$$\boldsymbol{u}(\boldsymbol{p})=K\big(\sin p_1,\sin p_2,\beta[\mu-\cos p_1-\cos p_2]\big) \tag{6.1}$$

a momentum-dependent vector that couples the spin bands. (We have set $\hbar$ and a both equal to unity.) The dispersion relation is $E_\pm(\boldsymbol{p})=\pm u(\boldsymbol{p})$, with $u=|\boldsymbol{u}|$ the norm of the vector $\boldsymbol{u}$. We fix the Fermi level at zero, in the middle of the energy gap.

Eq. (6.1) contains three parameters, K,β,μ. The parameter K sets the strength of the spin-orbit coupling. Time-reversal symmetry is broken by a nonzero β, representing a magnetization perpendicular to the 2D plane. The Hall conductance $G_{\rm H}$ is quantized at [25]

$$G_{\rm H}=\frac{e^2}{h}\times\begin{cases}\ \mathrm{sign}\,(\beta\,\mu) & \text{if }\ |\mu|<2,\\ \ 0 & \text{if }\ |\mu|>2.\end{cases} \tag{6.2}$$

This quantum Hall effect is called "anomalous", because it does not originate from Landau level quantization.

The value of $G_{\rm H}$ is a topological invariant [25], meaning that it is insensitive to variations of the Hamiltonian that do not close the energy gap. Since the gap can only close if $u(\boldsymbol{p})$ vanishes for some $\boldsymbol{p}$, the Hamiltonian

$$H_0(\boldsymbol{p})=\mathcal{T}(u)\,\boldsymbol{u}\cdot\boldsymbol{\sigma} \tag{6.3}$$

has the same quantized Hall conductance (6.2) if the function $\mathcal{T}(u)$ is positive definite. We will make use of this freedom in order to flatten the spin bands, by choosing a function $\mathcal{T}(u)$ which decays for large u.

The Hamiltonian $H_0(\boldsymbol{p})$ describes a clean system. The effects of electrostatic disorder are included by adding the scalar potential $V(\boldsymbol{x})$. The 2D coordinate $\boldsymbol{x}=(x_1,x_2)$ is measured in units of a, while momentum $\boldsymbol{p}=(p_1,p_2)$ is measured in units of $\hbar/a$, so their commutator is $[x_n,p_m]=i\delta_{nm}$.

6.2.2 Stroboscopic Hamiltonian

This completes the description of the QWZ model. We now introduce a periodic time dependence by multiplying H_0 with the stroboscopic function $\tau\sum_n\delta(t-n\tau)$, while keeping the scalar potential time-independent.

We thus arrive at the stroboscopic Hamiltonian

$$\mathcal{H}(t) = V(\boldsymbol{x}) + H_0(\boldsymbol{p}) \sum_{n=-\infty}^{\infty} \delta(t-n), \tag{6.4}$$

where we have set the period τ equal to unity.

For the choice of $\mathcal{T}(u)$ and $V(\boldsymbol{x})$ we are guided by the tight-binding representation given in App. 6.A. We use

$$\mathcal{T}(u) = \frac{2\arctan u}{u}, \tag{6.5}$$

which has a tight-binding representation with nearest-neighbor hopping. For the scalar potential $V(\boldsymbol{x})$ we take a separable form,

$$V(\boldsymbol{x}) = \sum_{i=1}^{2} V_i(x_i), \tag{6.6}$$

with $V_i(x_i)$ a low-order polynomial in x_i. Such a simple potential produces quasi-random on-site disorder in the tight-binding representation.

6.2.3 Relation to quantum kicked rotator

The quantum kicked rotator is a particle moving freely along a circle, with moment of inertia I, being subjected periodically (with period τ) to a kick whose strength depends $\propto \cos\theta$ on the angular coordinate θ. The quantum mechanical Hamiltonian is [7, 26]

$$H(t) = -\frac{\hbar^2}{2I}\frac{\partial^2}{\partial\theta^2} + \frac{KI}{\tau}\cos\theta \sum_{n=-\infty}^{\infty} \delta(t-n\tau). \tag{6.7}$$

The stroboscopic Hamiltonian (6.4) has the same general form, upon substitution of $\theta \mapsto \boldsymbol{p}$, with the extension from 1D to 2D and with the addition of a spin degree of freedom in the kicking term.

A 1D spinful kicked rotator has been used to study the effects of spin-orbit coupling on quantum localization [27–32]. (Because in the kicked rotator the variable which localizes is momentum rather than position, one speaks of *dynamical* localization.) In these 1D studies there was only a topologically trivial phase, while — as we shall see — the present 2D model exhibits a topological phase transition.

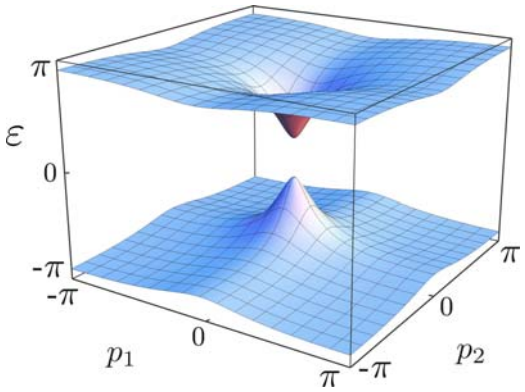

Figure 6.1. Momentum dependence of the quasi-energy (6.9) for zero disorder potential, calculated from Eqs. (6.1) and (6.5) for $K = 2$, $\beta = 0.8$, $\mu = 1.9$. At the center of the Brillouin zone the Dirac cone emerges, which will be fully formed when the gap closes at $\mu = 2$.

6.2.4 Floquet operator

The evolution $\Psi(t+1) = \mathcal{F}\Psi(t)$ of the wave function $\Psi(t)$ over one period is described by the Floquet operator $\mathcal{F}$. Integration of the Schrödinger equation $i\partial\Psi/\partial t = \mathcal{H}(t)\Psi(t)$ gives the Floquet operator as the product

$$\mathcal{F} = e^{-iH_0(\boldsymbol{p})}e^{-iV(i\partial_{\boldsymbol{p}})}, \tag{6.8}$$

with $i\partial_{\boldsymbol{p}} \equiv i\partial/\partial\boldsymbol{p}$ the position operator $\boldsymbol{x}$ in momentum representation.

The eigenvalues of the unitary operator $\mathcal{F}$ are phase factors $e^{-i\varepsilon}$. The phase shift $\varepsilon \in [-\pi, \pi)$ plays the role of energy (in units of $\hbar/\tau$), and is therefore called a quasi-energy. For $V \equiv 0$ the quasi-energy is an eigenvalue of H_0, hence

$$\varepsilon = \pm u\mathcal{T}(u), \quad \text{for} \quad V \equiv 0. \tag{6.9}$$

The $\boldsymbol{p}$-dependence of the two bands is plotted in Fig. 6.1. The emerging Dirac cone is clearly visible. Away from the cone the bands are quite flat, which is a convenient feature of our choice (6.5) of $\mathcal{T}(u)$.

More generally, for nonzero V, the 2π-periodicity of $H_0(\boldsymbol{p})$ implies that the eigenstates

$$\Psi_{\boldsymbol{q}}(\boldsymbol{p}) = e^{-i\boldsymbol{p}\cdot\boldsymbol{q}}\chi_{\boldsymbol{q}}(\boldsymbol{p}) \tag{6.10}$$

of $\mathcal{F}$ are labeled by a Bloch vector $\boldsymbol{q}$ in the Brillouin zone $-\pi < q_1, q_2 < \pi$. The function $\chi_{\boldsymbol{q}}(\boldsymbol{p})$ is a 2π-periodic eigenstate of

$$\mathcal{F}_{\boldsymbol{q}} = e^{-iH_0(\boldsymbol{p})} e^{-iV(i\partial_{\boldsymbol{p}}+\boldsymbol{q})}. \tag{6.11}$$

A convenient basis for the functions $\chi_{\boldsymbol{q}}(\boldsymbol{p})$ is formed by the eigenfunctions $\exp(-i\boldsymbol{m}\cdot\boldsymbol{p})$ of $\boldsymbol{x}$. The 2π-periodicity of $\chi_{\boldsymbol{q}}$ requires that the vector $\boldsymbol{m} = (m_1, m_2)$ contains integers.

6.3 Mapping onto a 1D model

The quantum kicked rotator in d dimensions can be simulated in one single dimension by means of d incommensurate driving frequencies [9, 33]. We apply this dimensional reduction to our stroboscopic model of the quantum Hall effect.

We take a linear potential in the variable x_2,

$$V(\boldsymbol{x}) = V_1(x_1) - \omega x_2, \tag{6.12}$$

with $\omega/2\pi$ an irrational number $\in (0, 1)$. During one period the momentum p_2 is incremented to $p_2 + \omega$ (modulo 2π), so ω is an incommensurate driving frequency. An initial state

$$\Psi(p_1, p_2, t = 0) = \psi(p_1, t = 0)\delta(p_2 - \alpha). \tag{6.13}$$

evolves as

$$\begin{aligned}\Psi(p_1, p_2, t) = e^{-iH_0(p_1,\omega t+\alpha)} e^{-iV_1(x_1)} \psi(p_1, t-1) \\ \times \delta(p_2 - \omega t - \alpha).\end{aligned} \tag{6.14}$$

We may therefore replace the 2D dynamics by a 1D dynamics with a time-dependent Floquet operator

$$\mathcal{F}(t) = e^{-iH_0(p_1,\omega t+\alpha)} e^{-iV_1(i\partial_{p_1})}, \tag{6.15}$$

$$\mathcal{F}_q(t) = e^{-iH_0(p_1,\omega t+\alpha)} e^{-iV_1(i\partial_{p_1}+q)}. \tag{6.16}$$

This reduction from two dimensions to one dimension greatly simplifies the numerical simulation of the quantum Hall effect.

For the potential in the remaining dimension we take a quadratic form,

$$V_1(x_1) = \tfrac{1}{2}\lambda(x_1 - x_0)^2, \tag{6.17}$$

with x_0 an arbitrary offset and $\lambda, \omega, 2\pi$ an incommensurate triplet. (We take $\lambda = 2$, $\omega = 2\pi/\sqrt{5}$.) From studies of the d-dimensional quantum kicked rotator it is known that such a simple potential, which is linear in $d-1$ dimensions and nonlinear in one single dimension, provides sufficient randomness for localization [34].

6.4 Localization in the quantum Hall effect

6.4.1 Numerical simulation

We base our numerical simulation on the 1D stroboscopic model with two incommensurate frequencies of Sec. 6.3. We introduce a Bloch number q and seek the time dependence of the state $\psi(p_1, t) = e^{-iqp_1}\chi_q(p_1, t)$. The state $\chi_q(p_1, t)$ is a 2π-periodic function of p_1, so it is a superposition of a discrete set of eigenstates e^{-imp_1} of x_1. For numerical purposes this infinite set is truncated to M states, $m \in \{1, 2, \ldots M\}$, with periodic boundary conditions at the end points.

Fourier transformation from eigenstates of x_1, with eigenvalue m, to eigenstates of p_1, with eigenvalue $2\pi n/M$, amounts to multiplication with the unitary matrix

$$U_{nm} = M^{-1/2} e^{2\pi i n m/M}, \quad n, m \in \{1, 2, \ldots M\}. \tag{6.18}$$

Calculation of the state $\chi_q(x_1, t)$, for t an integer multiple of $\tau \equiv 1$, requires $2t$ Fourier transformations,

$$\chi_q(x_1, t) = \left(\prod_{t'=0}^{t-1} \mathcal{F}_q(t') \right) \chi_q(x_1, 0), \tag{6.19}$$

$$\left[\mathcal{F}_q(t)\right]_{nm} = \sum_{k=1}^{M} U^*_{kn} e^{-iH_0(2\pi k/M, \omega t+\alpha)} U_{km} e^{-iV_1(m+q)}. \tag{6.20}$$

These operations can be carried out with high efficiency using the fast-Fourier-transform algorithm [35].

As initial state we choose

$$\chi_q(x_1, 0) = \delta_{x_0, x_1} \left[e^{-i\phi_0/2} \cos(\theta_0/2) \begin{pmatrix} 0 \\ 1 \end{pmatrix} \right. \tag{6.21}$$

$$\left. + e^{i\phi_0/2} \sin(\theta_0/2) \begin{pmatrix} 1 \\ 0 \end{pmatrix} \right], \tag{6.22}$$

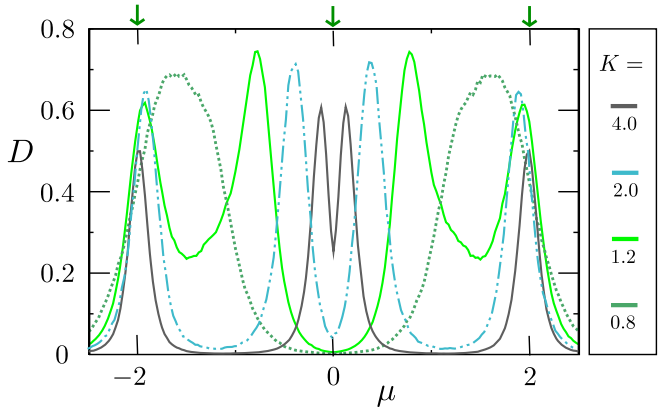

Figure 6.2. Time-dependent diffusion coefficient (6.25) at $t = 3000$ as a function of μ for $M = 1024$. The different values of K range from weak disorder ($K = 4$) to strong disorder ($K = 0.8$). The peaks signal a localization-delocalization transition. Compared to the three quantum Hall transitions in a clean system (indicated by arrows on the top), the two outer transitions are displaced inwards by disorder, while the central transition is split. The splitting of the two central peaks becomes larger and larger with increasing disorder, until they merge with the outer peaks.

spatially localized at $x_1 = x_0 = M/2$ (for even M). The angles ϕ_0, θ_0 of the initial spin direction are chosen randomly on the unit sphere.

6.4.2 Localization-delocalization transition

To search for localization we calculate the expectation value

$$\left\langle \big(x_1(t) - x_0\big)^2 \right\rangle = \sum_{m=1}^{M} (m - M/2)^2 |\chi_q(x_1 = m, t)|^2, \tag{6.23}$$

and obtain the mean squared displacement

$$\Delta^2(t) = \overline{\left\langle \big(x_1(t) - x_0\big)^2 \right\rangle} \tag{6.24}$$

by averaging over some 10^2–10^3 values of the random parameters $\alpha, q \in \{0, 1\}$. We fix $K = 2$, $\beta = 0.8$ and vary the parameter μ.

The system is localized if the time-dependent diffusion coefficient

$$D(t) = \frac{\Delta^2(t)}{t} \tag{6.25}$$

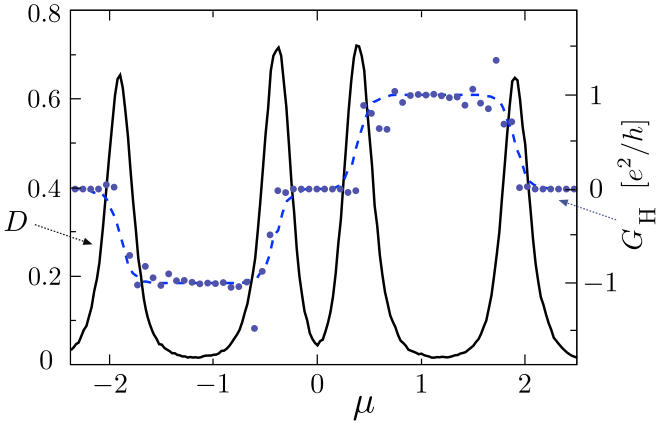

Figure 6.3. Left axis: Time-dependent diffusion coefficient for $K = 2$ (solid curve, same data as in Fig. 6.2), showing the four localization-delocalization transitions. Right axis: Four-terminal Hall conductance G_{H} (data points) and topological invariant $\mathcal{I}$ (dashed curve), calculated in Sec. 6.5, to demonstrate that these are *topological* phase transitions.

vanishes in the large-t limit. Delocalization with diffusive propagation corresponds to a non-zero large-time limit of $D(t)$. The quantum Hall phase transition is a localization-delocalization transition, so we would expect a peak in $D(t)$ as a function of μ at the critical points μ_c where the topological invariant switches from one value to another. In a clean system these values are $\mu_c = 0, \pm 2$, see Eq. (6.2).

The data in Fig. 6.2 shows that disorder has two effects: It shifts the outer transitions inwards and splits the central transition, resulting in a total of four peaks. We will demonstrate in Sec. 6.5 that these are *topological* phase transitions, by calculating the topological invariant — which as we can see in Fig. 6.3 switches at each of the transitions.

6.4.3 Scaling and critical exponent

In the single-parameter scaling theory of localization all microscopic parameters enter only through a single length scale ξ (the localization length) and the associated energy scale $\delta_\xi = (\xi^d \rho_c)^{-1}$ (being the mean level spacing in a d-dimensional box of size ξ, obtained from the density of states ρ_c at the critical energy) [36–38]. The corresponding scaling law

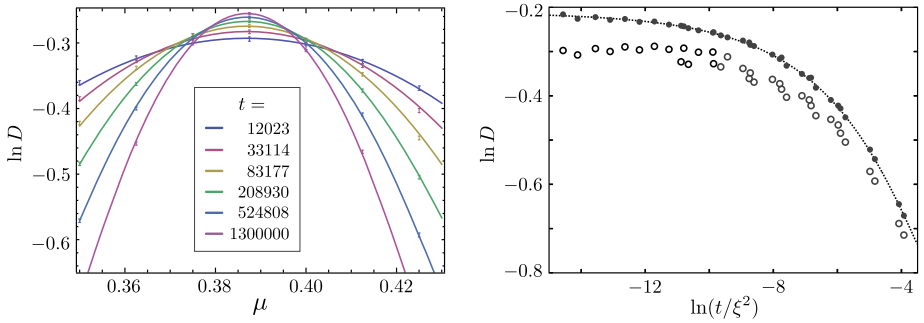

Figure 6.4. Left panel: Time-dependent diffusion coefficient for different times as a function of μ. The curves are a least-squares fit, used to extract the localization length $\xi(\mu)$ and the critical exponent (see App. 6.B). In the right panel time is rescaled, to test the scaling form $D(t,\mu) = F(t/\xi^2)$ [see Eq. (6.26)]. The open data points do not fully collapse onto a single scaling curve, due to finite-time corrections to scaling. The filled data points include the leading-order correction (see App. 6.B).

for dynamical localization has the form [39]

$$D(t) = \xi^{2-d} F(\xi^{-d} t), \tag{6.26}$$

in the large-time limit near the critical point μ_c. The localization length ξ diverges as a power law with critical exponent ν on approaching the transition,

$$\xi \propto |\mu - \mu_c|^{-\nu}. \tag{6.27}$$

The limiting behavior of the function $F(z)$ is $F(z) \propto 1/z$ for $z \to \infty$ and $F(z) \propto z^{2/d-1}$ for $z \to 0$. The first limit ensures that the mean squared displacement $\Delta^2 = tD(t) \to \xi^2$ becomes time independent in the limit $t \to \infty$ at fixed $\mu - \mu_c$. The second limit ensures that, if we send $\mu \to \mu_c$ at fixed t, the diffusion coefficient $D(t) \to t^{2/d-1}$ tends to a finite value. For $d = 2$, this value is also time independent, which implies regular diffusion ($D =$ constant) at criticality in two dimensions.

We have performed a finite-time scaling analysis of $D(t)$, similar to Refs. 6, 39, to obtain the localization length ξ and extract the value of the critical exponent. (See App. 6.B for details.) We considered times up to $t = 1.3 \cdot 10^6$ for system size $M = 2^{13} = 8192$. In Fig. 6.4 we show both the unscaled and the scaled data. For the two independent transitions we find $\nu = 2.576 \pm 0.03$ at $\mu_c = 0.387$ and $\nu = 2.565 \pm 0.03$ at

$\mu_c = 1.903$. Both results agree with $\nu_{\rm QHE} = 2.593$, the critical exponent for the quantum Hall phase transition [6].

6.5 Hall conductance and topological invariant

The quantum anomalous Hall effect in the absence of disorder ($V \equiv 0$) is characterized by the topological invariant [25]

$$\mathcal{I} = -\frac{1}{4\pi}\int_{-\pi}^{\pi} dp_1 \int_{-\pi}^{\pi} dp_2 \left[\frac{\partial \hat{\boldsymbol{u}}(\boldsymbol{p})}{\partial p_1} \times \frac{\partial \hat{\boldsymbol{u}}(\boldsymbol{p})}{\partial p_2}\right] \cdot \hat{\boldsymbol{u}}(\boldsymbol{p}), \tag{6.28}$$

with $\hat{\boldsymbol{u}} = \boldsymbol{u}/|\boldsymbol{u}|$. This socalled Skyrmion number does not apply for nonzero disorder potential, when momentum $\boldsymbol{p}$ is no longer a good quantum number.

We calculate the topological invariant for nonzero V from the winding number of the reflection matrix $r(\phi)$ in a cylinder geometry [40, 41],

$$\mathcal{I} = -\frac{1}{2\pi i}\int_0^{2\pi} d\phi\, \frac{d}{d\phi} \ln \mathrm{Det}\, r(\phi), \tag{6.29}$$

where $\Phi = \phi\hbar/e$ is the flux enclosed by the cylinder and $r(\phi)$ is evaluated at $\varepsilon = 0$. (We explain in App. 6.C how to construct the quasi-energy dependent reflection matrix from the Floquet operator [42, 43].) Since this is a 2D system, the sizes $M \times M$ for which we can calculate $\mathcal{I}$ are much smaller than in the 1D reduction used to calculate $D(t)$.

The results in Fig. 6.5 are for $M \times M = 40 \times 40$. This is data for a single sample ($\boldsymbol{q} = 0$), at fixed $K = 2$ as a function of β, μ. The disorder-averaged μ-dependence of $\mathcal{I}$ is plotted in Fig. 6.3 (dashed curve, for $\beta = 0.8$).

Comparing with the phase boundaries (6.2) for the clean system ($V \equiv 0$), we see that disorder introduces topologically trivial regions along clean phase boundaries. In the disordered system transitions between two different topologically nontrivial phases (with $\mathcal{I} = \pm 1$) go via a topologically trivial region ($\mathcal{I} = 0$). A similarly disruptive effect of disorder (but with a metallic gapless region replacing the topologically trivial phase) has been observed in computer simulations of the quantum *spin* Hall effect [44].

We have also calculated the Hall conductance $G_{\rm H}$, which unlike the topological invariant is a directly measurable quantity. The results shown

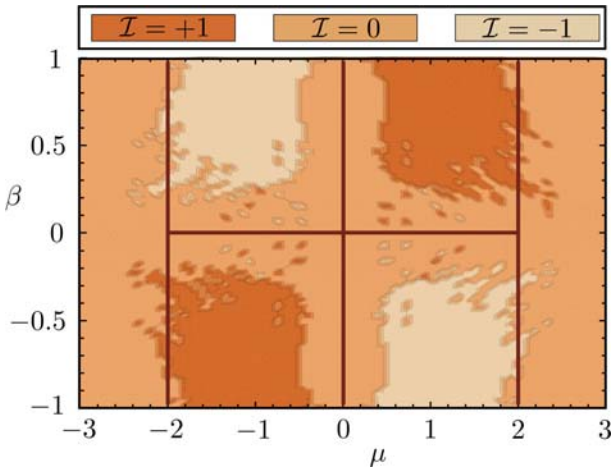

Figure 6.5. Phase diagram of the topological invariant $\mathcal{I}$ in a cylinder of size 40×40, calculated from Eq. (6.29) for a single disorder realization. The solid lines are the phase boundaries (6.2) in the clean system.

in Fig. 6.3 (data points) were obtained in a single four-terminal sample of dimensions $M \times M = 70 \times 70$, directly taken from the scattering matrix expression for the Hall conductance [45]. The Hall plateaus are at the values expected from the topological invariant, $G_{\mathrm{H}} \approx \mathcal{I} \times e^2/h$, with deviations from exact quantization due to the relatively small size of the 2D system.

6.6 Discussion

We have shown how the quantum Hall effect can be modeled in a 1D dynamical system, by using a pair of incommensurate driving frequencies to simulate the effect of a second spatial dimension. This 1D stroboscopic model could become a competitive alternative to the 2D network model for numerical studies of the quantum Hall phase transition [4], similarly to how the 1D quantum kicked rotator is an alternative to the 3D Anderson model of the metal-insulator transition [9].

Since quantum kicked rotators can be realized using cold atoms [10, 11, 39, 46], the stroboscopic model might also provide a way to study the quantum Hall effect using atomic matter waves. Cold atoms represent clean and controllable experimental quantum systems, owing

to the ability to tune interaction strengths and external potentials [47]. Due to the absence of impurities they have long phase coherence times, so their quantum dynamics can be followed over long time scales. These properties make cold atoms ideally suited for the experimental study of quantum phase transitions.

There is a particular need for a new physical system to investigate the quantum Hall phase transition, because currently the theory disagrees with semiconductor experiments on the value of the critical exponent [6]. This might be an effect of Coulomb interactions between the electrons in a semiconductor, and a system with controllable interactions could shed light on this question.

For cold atomic gases prepared in a magneto-optical trap a quasi-periodically modulated 1D standing wave, created by two overlapping laser beams, simulates the quasi-periodic driving of the kicked rotator [46]. The momentum distribution is accessible through an absorption measurement, following the release of the atomic gas from the trap [47]. Since in the kicked rotator momentum plays the role of coordinate, in this way the diffusion coefficient could be measured and the critical exponent of the metal-insulator transition was obtained from its time dependence [10, 11, 39].

To realize the stroboscopic model of the quantum Hall effect, a controllable spin-1/2 degree of freedom is needed. Hyperfine levels in alkali or earth alkali atoms can be used for that purpose [47], and arbitrary rotations of this pseudospin have been demonstrated in Cs [48]. Two overlapping standing waves would produce a purely sinusoidal kicking potential (corresponding to $\mathcal{T}(u) \equiv 1$), while for flat spin bands higher harmonics are desirable. Fortunately, the topological nature of the phase transition ensures that there is considerable freedom in the choice of the potentials.

Continuing on the path of dimensional reduction proposed here, it is conceivable that the hypothetical 4D quantum Hall effect [49] might also be realized in the laboratory, by adding two more incommensurate driving frequencies.

Appendix 6.A Tight-binding representation

To gain further insight into the stroboscopic model, we give a tight-binding representation. This will motivate the specific form (6.5) for the function $\mathcal{T}(u)$ and it will also guide us in the choice (6.6) for the scalar potential $V(\boldsymbol{x})$. The derivation follows the same steps as for the quantum kicked rotator [8, 27].

Including the spin degree of freedom ($s = \pm 1$), we denote the coordinate basis states by $|\boldsymbol{m}, s\rangle$, such that $x_i|\boldsymbol{m}, s\rangle = m_i|\boldsymbol{m}, s\rangle$ and $\sigma_z|\boldsymbol{m}, s\rangle = s|\boldsymbol{m}, s\rangle$. The two states $|a_\pm\rangle$ defined by

$$\mathcal{F}_{\boldsymbol{q}}|a_+\rangle = e^{-i\varepsilon}|a_+\rangle, \tag{6.30a}$$

$$|a_-\rangle = e^{iH_0}|a_+\rangle = e^{i\varepsilon - iV_{\boldsymbol{q}}}|a_+\rangle \tag{6.30b}$$

are evaluated just after and just before the kick. [We have abbreviated $V_{\boldsymbol{q}} = V(i\partial_{\boldsymbol{p}} + \boldsymbol{q})$.] Both states evolve with a phase factor $e^{-i\varepsilon}$ in one period $\tau \equiv 1$. The tight-binding representation is expressed in terms of the average

$$|b\rangle = \tfrac{1}{2}\big(|a_+\rangle + |a_-\rangle\big). \tag{6.31}$$

The Hermitian operator

$$W = i\frac{1 - e^{iH_0}}{1 + e^{iH_0}} = \frac{1}{u}\tan\big[\tfrac{1}{2}u\mathcal{T}(u)\big]\boldsymbol{u}\cdot\boldsymbol{\sigma} \tag{6.32}$$

allows to relate $|b\rangle$ to $|a_\pm\rangle$ separately,

$$|b\rangle = \frac{1}{1 + iW}|a_-\rangle = \frac{1}{1 - iW}|a_+\rangle. \tag{6.33}$$

Substitution into Eq. (6.30b) gives

$$(1 + iW)|b\rangle = e^{i\varepsilon - iV_{\boldsymbol{q}}}(1 - iW)|b\rangle \tag{6.34a}$$

$$\Rightarrow i\frac{1 - e^{i\varepsilon - iV_{\boldsymbol{q}}}}{1 + e^{i\varepsilon - iV_{\boldsymbol{q}}}}|b\rangle = W|b\rangle \tag{6.34b}$$

$$\Rightarrow \tan[(\varepsilon - V_{\boldsymbol{q}})/2]|b\rangle = W|b\rangle. \tag{6.34c}$$

In coordinate representation this gives the tight-binding equations

$$\sum_{\boldsymbol{n}}\sum_{s'} W_{\boldsymbol{n}}^{ss'} b_{\boldsymbol{m}+\boldsymbol{n}}^{s'} + \tan\left[\tfrac{1}{2}V(\boldsymbol{m} + \boldsymbol{q}) - \tfrac{1}{2}\varepsilon\right] b_{\boldsymbol{m}}^{s} = 0, \tag{6.35}$$

with hopping matrix elements

$$W_{\boldsymbol{n}}^{ss'} = \langle \boldsymbol{m}, s | W(\boldsymbol{p}) | \boldsymbol{m} + \boldsymbol{n}, s' \rangle, \tag{6.36a}$$

$$W(\boldsymbol{p}) = \frac{1}{u} \tan\left[\tfrac{1}{2} u \mathcal{T}(u)\right] \boldsymbol{u} \cdot \boldsymbol{\sigma}. \tag{6.36b}$$

The tangent term in Eq. (6.35) provides a pseudo-random on-site potential, provided that $V(\boldsymbol{m} + \boldsymbol{q})$ changes from site to site in a way which is incommensurate with the periodicity π of the tangent. This is why a simple polynomial $V(\boldsymbol{x})$ suffices to produce the localizing effect of a disorder potential [8].

The role of the Bloch vector $\boldsymbol{q}$ is to provide different realizations of the disorder potential, so that a disorder average is effectively an average of $\boldsymbol{q}$ over the Brillouin zone. The strength of the disorder potential is varied by varying the parameter K, which determines the relative magnitude of kinetic and potential energies: *small* K corresponds to *strong* disorder.

From Eq. (6.36) we see that different choices for $\mathcal{T}(u)$ lead to different hopping matrix elements, leaving the on-site disorder unaffected. The arctangent form in Eq. (6.5) has the simplifying effect of excluding hopping between sites that are not nearest neighbors. For this choice $\frac{1}{u}\tan[\frac{1}{2}u\mathcal{T}(u)] \equiv 1$ the hopping matrix elements are given by

$$\begin{aligned} W_{\boldsymbol{n}} = {} & 2\pi K \beta \mu \sigma_z \delta_{n_1,0} \delta_{n_2,0} \\ & + \pi K (\pm i\sigma_y - \beta\sigma_z) \delta_{n_1,0} \delta_{n_2,\pm 1} \\ & + \pi K (\pm i\sigma_x - \beta\sigma_z) \delta_{n_1,\pm 1} \delta_{n_2,0}. \end{aligned} \tag{6.37}$$

Appendix 6.B Finite-time scaling

Following Refs. 6, 39, we extract the critical exponent ν from finite-time numerical data by fitting the diffusion coefficient (or, more conveniently, its logarithm) to the scaling law $D(t) = F(t/\xi^2)$. For finite t the diffusion coefficient is an analytic function of μ. In view of Eq. (6.27) the variable $(t/\xi^2)^{1/2\nu} = t^{1/2\nu} u$ is an analytic function of μ, vanishing at μ_c.

We therefore have the two power series

$$\ln D(t) = \ln D_c + \sum_{k=1}^{N_1} c_k^{(1)} \left(t^{1/2\nu} u \right)^k + c_0 t^{-y}, \tag{6.38}$$

$$u = \mu - \mu_c + \sum_{k=2}^{N_2} c_k^{(2)} (\mu - \mu_c)^k. \tag{6.39}$$

The term $c_0 t^{-y}$, with $y > 0$, accounts for finite-time corrections to single-parameter scaling at the transition point. We put $c_1 = 0$, $c_2 < 0$, to ensure that $D(t)$ as a function of μ has a maximum at μ_c. We then choose integers N_1, N_2 and fit the parameters D_c, ν, c_0, y with $c_k^{(i)}$ ($i \in \{1,2\}$, $2 \leq k \leq N_i$) to the t and μ-dependence of $D(t)$, for a given 1D system size M.

For the transition around $\mu = 0.38$ we took times $t = 1.2 \cdot 10^4$, $3.3 \cdot 10^4$, $8.3 \cdot 10^4$, $2.1 \cdot 10^5$, $5.2 \cdot 10^5$, and $1.3 \cdot 10^6$, with $M = 2^{13} = 8192$. We averaged over 1000 samples. The quality of the fit is quantified by the chi-square-value per degree of freedom (χ^2/ndf). We systematically increased N_1, N_2 until we arrived at $\chi^2/\mathrm{ndf} \approx 1$. Only the leading order term in Eq. (6.39) was needed for a good fit, so we simply took $u = \mu - \mu_c$. The expansion (6.38) did need higher order terms, up to $N_1 = 6$. We thus obtained $\nu = 2.576 \pm 0.03$ at $\mu_c = 0.387$ with $\chi^2/ndf = 1.2$. A similar analysis was performed for the outer peak in fig. 6.3, resulting in $\nu = 2.565 \pm 0.03$ at $\mu_c = 1.903$ with $\chi^2/ndf = 1.01$.

Appendix 6.C Scattering matrix from Floquet operator

To calculate the topological invariant (6.29) we need the reflection matrix $r(\phi)$ in a cylinder geometry, at quasi-energy $\varepsilon = 0$ as a function of the flux $\Phi = \phi\hbar/e$ enclosed by the cylinder. This can be obtained from a four-terminal scattering matrix S, which relates the wave amplitudes of incoming and outgoing states at the four edges of an $M \times M$ square lattice of sites $(x_1, x_2) = (m_1, m_2)$, $m_i = 1, 2, \ldots M$. The dimensionality of S is $8M \times 8M$, with the factor of 8 accounting for four terminals and a twofold spin degree of freedom. The Floquet operator $\mathcal{F}_q$ is a $2M^2 \times 2M^2$ matrix describing the stroboscopic time evolution of states on the 2D lattice. (We do not make the dimensional reduction to 1D for this calculation.)

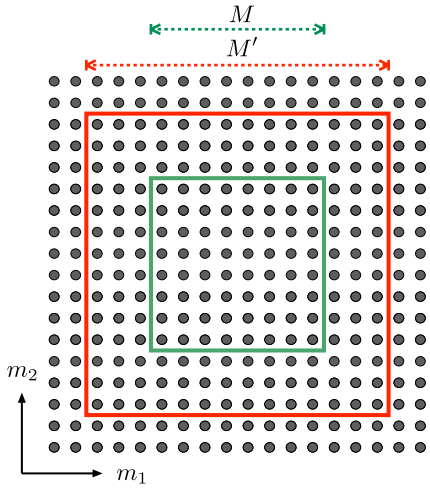

Figure 6.6. Truncation of the lattice used to construct a four-terminal scattering matrix, as described in the text.

When the square is folded into a cylinder, incoming and outgoing states at the left and right edge are related by a phase factor $e^{i\phi}$. This relation can be used to reduce the four-terminal scattering matrix to a two-terminal scattering matrix $\tilde{S}(\phi)$ (which now has dimension $4M \times 4M$). The reflection matrix $r(\phi)$ is a $2M \times 2M$ subblock of $\tilde{S}(\phi)$, relating incoming and outgoing states at the lower edge. We refer to Ref. 41 for a computationally efficient way to carry out this general procedure.

What we discuss in this Appendix is how to obtain S from $\mathcal{F}_q$. We are faced with the complication that the truncation of the coordinates to a finite range M introduces spurious hopping matrix elements that couple sites near opposite edges (typically within 5–10 sites from the edge). We cannot directly delete these matrix elements from the Floquet matrix without losing unitarity.

Our solution (illustrated in Fig. 6.6) is to start from a larger $M' \times M'$ system (red square), with Floquet matrix $\mathcal{F}'_q = e^{-iH'_0}e^{-iV'_q}$. We then go back to the $M \times M$ system (green square) by deleting rows and columns in the coordinate representation of $H'_0 \mapsto H_0$ and $V'_q \mapsto V_q$. The resulting Floquet matrix $\mathcal{F}_q = e^{-iH_0}e^{-iV_q}$ remains unitary. By choosing M' sufficiently larger than M (typically $M' = M + 10$ suffices), we effectively eliminate the spurious hopping matrix elements.

For a four-terminal scattering matrix we introduce absorbing termi-

nals at the four edges of the $M \times M$ lattice. The $8M \times 2M^2$ matrix P projects onto these terminals,

$$P^{ss'}_{\boldsymbol{m}\boldsymbol{m}'} = \delta_{ss'}\delta_{m_1 m_1'}\delta_{m_2 m_2'} \times \begin{cases} 1 & \text{if } m_1 \in \{1, M\}, \\ 1 & \text{if } m_2 \in \{1, M\}, \\ 0 & \text{otherwise.} \end{cases} \tag{6.40}$$

The ε-dependent scattering matrix S is obtained from the Floquet matrix $\mathcal{F}_q$ through the formula [42, 43]

$$S = P\left[1 - e^{i\varepsilon}\mathcal{F}_q(1 - P^T P)\right]^{-1} e^{i\varepsilon}\mathcal{F}_q P^T, \tag{6.41}$$

where the superscript T indicates the transpose of the matrix. The quasi-energy ε is set to zero for the calculation of the topological invariant (6.28). The integral over ϕ is evaluated analytically[41] by contour integration over complex $z = e^{i\phi}$. Results for $M = 40$ are shown in Figs. 6.3 and 6.5.

To calculate the Hall conductance G_{H} we directly use the four-terminal scattering matrix S, without rolling up the system into a cylinder. The geometry is still that of Fig. 6.6, but the four absorbing terminals are point contacts, covering a single site at the center of each edge. The dimensionality of the scattering matrix, including spin, is thus 8×8. A current I_{13} flows from terminal 1 to terminal 3 and the voltage V_{24} is measured between terminals 2 and 4 (which draw no current). The Hall conductance $G_{\mathrm{H}} = I_{13}/V_{24}$ is obtained from the scattering matrix elements using Büttiker's formulas [45]. Results for $M = 70$ are shown in Fig. 6.3.

Bibliography

[1] K. von Klitzing, G. Dorda, and M. Pepper, Phys. Rev. Lett. **45**, 494 (1980).

[2] B. Huckestein, Rev. Mod. Phys. **67**, 357 (1995).

[3] D. J. Thouless, M. Kohmoto, M. P. Nightingale, and M. Nijs, Phys. Rev. Lett. **49**, 405 (1982).

[4] J. T. Chalker and P. D. Coddington, J. Phys. C **21**, 2665 (1988).

[5] B. Kramer, T. Ohtsuki, and S. Kettemann, Phys. Rep. **417**, 211 (2005).

[6] K. Slevin and T. Ohtsuki, Phys. Rev. B **80**, 041304 (2009).

[7] G. Casati, B. V. Chirikov, F. M. Izrailev, and J. Ford, Lect. Notes Phys. **93**, 334 (1979).

[8] S. Fishman, D. Grempel, and R. Prange, Phys. Rev. Lett. **49**, 509 (1982).

[9] D. L. Shepelyansky, Physica D **8**, 208 (1983).

[10] J. Chabé, G. Lemarié, B. Grémaud, D. Delande, P. Szriftgiser, and J. Garreau, Phys. Rev. Lett. **101**, 255702 (2008).

[11] G. Lemarié, H. Lignier, D. Delande, P. Szriftgiser, and J. Garreau, Phys. Rev. Lett. **105**, 090601 (2010).

[12] M. Sadgrove, Physics **1**, 41 (2008).

[13] C. Tian, A. Altland, and M. Garst, Phys. Rev. Lett. **107**, 074101 (2011)

[14] D. L. Shepelyansky, arXiv:1102.4450

[15] T. Kitagawa, M. Rudner, E. Berg, and E. Demler, Phys. Rev. A **82**, 033429 (2010).

[16] T. Kitagawa, E. Berg, M. Rudner, and E. Demler, Phys. Rev. B **82**, 235114 (2010).

[17] J. Inoue and A. Tanaka, Phys. Rev. Lett. **105**, 017401 (2010).

[18] N. H. Lindner, G. Refael, V. Galitski, Nature Phys. **7**, 490 (2011).

[19] L. Jiang, T. Kitagawa, J. Alicea, A. R. Akhmerov, D. Pekker, G. Refael, J. I. Cirac, E. Demler, M. D. Lukin, and P. Zoller, Phys. Rev. Lett. **106**, 220402 (2011).

[20] H. Obuse and N. Kawakami, Phys. Rev. B **84**, 195139 (2011).

[21] N. R. Cooper, Adv. Phys. **57**, 539 (2008).

[22] Y.-J. Lin, R. L. Compton, K. Jiménez-García, J. V. Porto, and I. B. Spielman, Nature, **662**, 628 (2009).

[23] J. Dalibard, F. Gerbier, G. Juzeliūnas, and P. Öhberg, Rev. Mod. Phys. 83, 1523 (2011) .

[24] F. D. M. Haldane, Phys. Rev. Lett. **61**, 2015 (1988).

[25] X.-L. Qi, Y.-S. Wu, and S.-C. Zhang, Phys. Rev. B **74**, 085308 (2006).

[26] F. M. Izrailev, Phys. Rep. **196**, 299 (1990).

[27] R. Scharf, J. Phys. A **22**, 4223 (1989).

[28] M. Thaha and R. Blümel, Phys. Rev. Lett. **72**, 72 (1994).

[29] D. R. Mašović and A. R. Tančić, Phys. Lett. A **191**, 384 (1994).

[30] A. Ossipov, D. M. Basko, and V. E. Kravtsov, Eur. Phys. J. B **42**, 457 (2004).

[31] J. H. Bardarson, J. Tworzydło, and C. W. J. Beenakker, Phys. Rev. B **72**, 235305 (2005).

[32] J. H. Bardarson, I. Adagideli, and Ph. Jacquod, Phys. Rev. Lett. **98**, 196601 (2007).

[33] G. Casati, I. Guarneri, and D. L. Shepelyansky, Phys. Rev. Lett. **62**, 345 (1989).

[34] F. Borgonovi and D. L. Shepelyansky, Physica D **109**, 24 (1997).

[35] R. Ketzmerick, K. Kruse, and T. Geisel, Physica D **131**, 247 (1999).

[36] J. T. Chalker, Physica A **167**, 253 (1990).

[37] T. Brandes, B. Huckestein, and L. Schweitzer, Ann. Phys. (Leibzig) **8**, 633 (1996).

[38] B. Huckestein and R. Klesse, Phil. Mag. B **77**, 1181 (1998).

[39] G. Lemarié, J. Chabé, P. Szriftgiser, J. Garreau, B. Grémaud, and D. Delande, Phys. Rev. A **80**, 043626 (2009).

[40] G. Bräunlich, G. M. Graf, and G. Ortelli, Com. Math. Phys. **295**, 243 (2009).

[41] I. C. Fulga, F. Hassler, and A. R. Akhmerov, Phys. Rev. B **85**, 165409 (2012).

[42] Y. V. Fyodorov and H.-J. Sommers, JETP Lett. **72**, 422 (2000).

[43] A. Ossipov, T. Kottos, and T. Geisel, Phys. Rev. E **65**, 055209 (2002).

[44] A. Yamakage, K. Nomura, K.-I. Imura, and Y. Kuramoto, J. Phys. Soc. Japan **80**, 053703 (2011).

[45] M. Büttiker, Phys. Rev. Lett. **57**, 1761 (1986).

[46] F. L. Moore, J. C. Robinson, C. F. Bharucha, B. Sundaram, and M. G. Raizen, Phys. Rev. Lett. **75**, 4598 (1995).

[47] I. Bloch, J. Dalibard, and W. Zwerger, Rev. Mod. Phys. **80**, 885 (2008).

[48] M. Karski, L. Förster, J.-M. Choi, A. Steffen, W. Alt, D. Meschede, and A. Widera, Science **325**, 174 (2009).

[49] S.-C. Zhang and J. Hu, Science **294**, 823 (2001).

Chapter 7

Metal–topological-insulator transition in the quantum kicked rotator with $\mathbb{Z}_2$ symmetry

7.1 Introduction

The spin of an electron moving in an electric field experiences a torque, which can be understood as arising from the magnetic field in its rest frame. In a two-dimensional electron gas this velocity-dependent magnetic field produces the quantum spin Hall effect [1, 2], reminiscent of the quantum Hall effect but without time-reversal symmetry breaking [3]. The difference manifests itself in the integer quantized values Q of the dimensionless conductance. While there is no restriction on $Q \in \mathbb{Z}$ in the quantum Hall effect (QHE), only the two values $Q = 0, 1 \in \mathbb{Z}_2$ appear in the quantum spin Hall effect (QSHE). In both effects the current is carried by edge states, separated by an insulating bulk. The insulator in the QSHE is called a topological insulator [4, 5] if the topological quantum number $Q = 1$ and a trivial insulator if $Q = 0$.

Bulk states delocalize when the conductance switches between quantized values. A distinguishing feature of the QSHE is that the delocalized states can support metallic conduction (conductance $\gg e^2/h$), while in the QHE the conductance remains $\lesssim e^2/h$. The metallic conduction

appears in extended regions of phase space, separated by a quantum phase transition (Anderson transition) from the regions with a quantized conductance and an insulating bulk. For a trivial insulator this is the familiar metal-insulator transition in a two-dimensional (2D) electron gas with spin-orbit scattering [6, 7].

A fundamental question raised by the discovery of the QSHE was whether the phase transition would depend on the topological quantum number. Specifically, is the critical exponent ν_Q of the diverging localization length different if the phase boundary separates a metal from a topological insulator, rather than a trivial insulator? A numerical simulation [8] of the Kane-Mele model [1] of the QSHE gave an affirmative answer, finding a value $\nu_1 \approx 1.6$ substantially below the established result[9, 10] for the metal–trivial-insulator transition. In contrast, studies of the network model in the QSHE universality class gave $\nu_1 = \nu_0 \approx 2.7$ within numerical accuracy [11, 12], consistent with analytical considerations from the nonlinear sigma model [13] why the critical exponent should be Q-independent.

In this chapter we study the metal-insulator transition in the QSHE by means of an altogether different, *stroboscopic* model — the periodically driven system known as the quantum kicked rotator [14–16]. A key feature of this dynamical system is that spatial dimensions can be exchanged for incommensurate driving frequencies [17, 18], allowing for the study of metal-insulator transitions in one spatial dimension [19, 20]. This proved very effective in the QHE [21], and also made it possible to experimentally study the 3D Anderson transition in a 1D optical lattice [22]. In the present chapter we apply the same strategy to study the 2D QSHE in a 1D system.

In the next section we show how the quantum kicked rotator can be extended to include the topological $Q = 1$ phase of the QSHE. We first construct this $\mathbb{Z}_2$ quantum kicked rotator in 2D and then carry out the mapping to 1D. We calculate the phase diagram in Sec. 7.3, using a scattering formula for the topological quantum number valid for disordered systems [23, 24]. In Sec. 7.4 we determine the scaling law at the metal-insulator phase transition and compare the critical exponents ν_Q for $Q = 0$ and $Q = 1$. We conclude in Sec. 7.5.

7.2 Construction of the $\mathbb{Z}_2$ quantum kicked rotator

7.2.1 Stationary model without disorder

We start from a translationally invariant 2D system and will add disorder later. The minimal model Hamiltonian $H_0(\boldsymbol{p})$ of the QSHE has four bands at each momentum $\boldsymbol{p} = (p_1, p_2)$, distinguished by indices σ (up and down spins) and τ (s and p orbitals). The Pauli matrices σ_i and τ_i ($i = 0, x, y, z$) act on the spin and orbital degrees of freedom, respectively. Time-reversal symmetry is essential:

$$\sigma_y H^*(-\boldsymbol{p})\sigma_y = H(\boldsymbol{p}). \tag{7.1}$$

Inversion symmetry is not essential (and will be broken anyway once we add disorder), but is assumed for convenience:

$$\tau_z H(-\boldsymbol{p})\tau_z = H(\boldsymbol{p}). \tag{7.2}$$

The generic Hamiltonian that satisfies the symmetries (7.1) and (7.2) has the form [25]

$$H(\boldsymbol{p}) = E_0(\boldsymbol{p}) + \sum_{\alpha=1}^{5} f_\alpha(\boldsymbol{p})\Gamma_\alpha, \tag{7.3}$$

$$\boldsymbol{\Gamma} = \big(\tau_x\sigma_z,\ \tau_y\sigma_0,\ \tau_z\sigma_0,\ \tau_x\sigma_x,\ \tau_x\sigma_y\big). \tag{7.4}$$

The real functions E_0, f_3 are even under inversion of $\boldsymbol{p}$, while the functions f_1, f_2, f_4, f_5 are odd. Because the Γ-matrices anticommute, $\{\Gamma_\alpha, \Gamma_\beta\} = 2\delta_{\alpha\beta}$, the band structure is given by

$$\varepsilon_\pm(\boldsymbol{p}) = E_0(\boldsymbol{p}) \pm \sqrt{\textstyle\sum_\alpha f_\alpha^2(\boldsymbol{p})}. \tag{7.5}$$

Each band is twofold degenerate.

The band gap can close upon variation of a single control parameter at high-symmetry points $\boldsymbol{\Lambda}_a$ in the first Brillouin zone, which satisfy $\boldsymbol{\Lambda}_a = -\boldsymbol{\Lambda}_a$ modulo a reciprocal lattice vector. At these time-reversally invariant momenta the Bloch wave function $u_-(\boldsymbol{\Lambda}_a)$ of the lower band has a definite parity $\pi_a = \pm 1$ under inversion, $\tau_z u_-(\boldsymbol{\Lambda}_a) = \pi_a u_-(\boldsymbol{\Lambda}_a)$. The $\mathbb{Z}_2$ topological quantum number Q follows from the Fu-Kane formula [26],

$$(-1)^Q = \prod_a \pi_a. \tag{7.6}$$

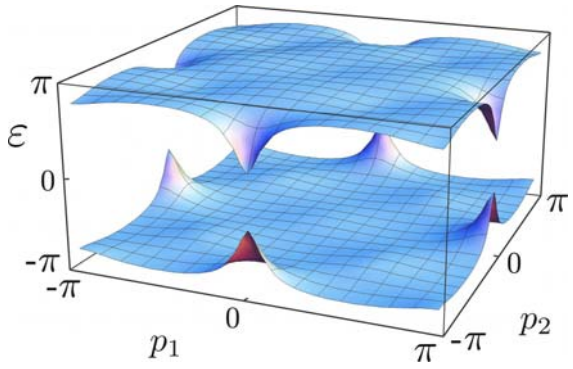

Figure 7.1. Band structure for the clean Hamiltonian $H(\mathbf{p})$, as calculated from Eqs. (7.5), (7.7), and (7.8), for parameter values $K = 2$, $\beta = 0.8$, $\gamma = 2$, $\mu = -0.3$. The Dirac cones emerging at the time-reversally invariant points in the Brillouin zone will touch when $\mu = 0$.

A gap closing and reopening can switch the parity of the lower and upper bands, inducing a change in Q (a topological phase transition).

The specific choice for the functions $f_\alpha(\boldsymbol{p})$ which we will study in the following is based on experience with the stroboscopic model of the QHE [21]. We take

$$E_0 \equiv 0, \quad f_\alpha = T(u)u_\alpha, \quad T(u) = (2/u)\arctan u, \tag{7.7}$$

where the vector $\boldsymbol{u}$ (of length $u = |\boldsymbol{u}|$) has components

$$\begin{aligned}\boldsymbol{u}(\boldsymbol{p}) = \Big(&K\sin p_1,\ K\sin p_2,\ \beta K(\mu - \cos p_1 - \cos p_2),\\ &\gamma K\cos p_1 \sin p_2,\ \gamma K\cos p_2 \sin p_1\Big).\end{aligned} \tag{7.8}$$

For $\gamma = 0$ this is the Bernevig-Hughes-Zhang model of the QSHE [27], up to a function $T(u) > 0$ which flattens the bands without closing the band gap (hence without affecting the topological quantum number). Without the γ-term the spin degree of freedom σ is conserved and the QSHE Hamiltonian is identical to two copies of the QHE Hamiltonian (with opposite magnetic fields, to restore time-reversal symmetry). When $\gamma \neq 0$ spin-orbit coupling mixes the spin-up and spin-down blocks of the Hamiltonian.

The band structure for one set of parameters is shown in Fig. 7.1. The time-reversally invariant momenta $\boldsymbol{\Lambda}_a$ in the first Brillouin zone

$-\pi < p_1, p_2 \leq \pi$ are at the four points $(0,0)$, (π,π), $(0,\pi)$, $(\pi,0)$. (We have set both $\hbar$ and the lattice constant a equal to unity.) The topological quantum number (7.6) depends only on the parameter μ,

$$Q = \begin{cases} 0 & \text{if } |\mu| > 2, \\ 1 & \text{if } |\mu| < 2. \end{cases} \tag{7.9}$$

For $\mu = 2$ or -2 the band gap closes at $(0,0)$ or (π,π), with a switch in parity and a change of Q. For $\mu = 0$ the gap closes at both points $(0,\pi)$ and $(\pi,0)$ — at constant Q since the two parity switches cancel.

7.2.2 Time-dependent model with disorder

The time-dependent model is based on the quantum kicked rotator [14], which is a dynamical system designed to study the localization by disorder with great nuerical efficiency [15, 16, 20]. The time dependent Hamiltonian $\mathcal{H}(t)$ contains a disorder potential $V(\boldsymbol{x})$ and a stroboscopic kinetic energy $H(\boldsymbol{p})$,

$$\mathcal{H}(t) = V(\mathbf{x}) + H(\mathbf{p}) \sum_{n=-\infty}^{\infty} \delta(t-n). \tag{7.10}$$

(The stroboscopic period τ has been set equal to unity.) We take $H(\boldsymbol{p})$ of the form (7.3) and will specify $V(\boldsymbol{x})$ later. The disorder strength is set by the relative importance of $V(\boldsymbol{x})$ and $H(\boldsymbol{p})$. The Floquet operator $\mathcal{F}$ describes the time evolution of the wavefunction over one period,

$$\Psi(t+1) = \mathcal{F}\Psi(t), \quad \mathcal{F} = e^{-iH(p)} e^{-iV(i\partial_p)}. \tag{7.11}$$

Here $i\partial_{\mathbf{p}}$ is the operator $\mathbf{x}$ in the momentum representation. The eigenvalues $e^{-i\varepsilon}$ of the unitary operator $\mathcal{F}$ define the quasi-energies $\varepsilon \in (-\pi, \pi)$.

We use the 2π-periodicity of $H(\boldsymbol{p})$ to label the eigenstates $\Psi_{\boldsymbol{q}}(\boldsymbol{p})$ of $\mathcal{F}$ by a Bloch vector $\boldsymbol{q}$ in the Brillouin zone $-\pi < q_1, q_2 \leq \pi$. By construction,

$$\Psi_{\boldsymbol{q}}(\boldsymbol{p}) = e^{-ip\cdot q} \chi_{\boldsymbol{q}}(\boldsymbol{p}), \tag{7.12}$$

with $\chi_{\boldsymbol{q}}(\boldsymbol{p})$ a 2π-periodic eigenstate of

$$\mathcal{F}_{\boldsymbol{q}} = e^{-iH(p)} e^{-iV(i\partial_p + q)}. \tag{7.13}$$

This is the quantum kicked rotator with $\mathbb{Z}_2$ symmetry.

7.2.3 Mapping from 2D to 1D

By adding an incommensurate driving frequency to the quantum kicked rotator in two spatial dimensions, it is possible to simulate the system in one single dimension [17, 18]. For that purpose we take a potential of the form

$$V(\boldsymbol{x}) = V_1(x_1) - \omega x_2, \tag{7.14}$$

with $\omega/2\pi$ an irrational number $\in (0,1)$. We consider states which at $t = 0$ are plane waves in the x_2-direction, having a well-defined initial momentum $p_2 = \alpha$. In the Floquet operator the term linear in x_2 has the effect of shifting p_2 to $p_2 + \omega$, so that the 2D operator $\mathcal{F}_q$ can be replaced at the n-th time step by the 1D operator

$$\mathcal{F}_q^{(n)} = e^{-iH(p_1,\, n\omega+\alpha)} e^{-iV_1(i\partial_{p_1}+q)}. \tag{7.15}$$

There is considerable freedom in the choice of the potential V_1 in the remaining dimension. The simple quadratic form

$$V_1(x_1) = \lambda(x_1 - x_0)^2 \tag{7.16}$$

provides sufficient randomness if $\{\omega, \lambda, 2\pi\}$ form an incommensurate triplet [28]. We take $\lambda = 1$, $\omega = 2\pi/\sqrt{5}$.

The numerical simulation is performed by subsequent multiplication of the state $\chi_q(x_1, t)$ with the series of Floquet operators $\mathcal{F}_q^{(n)}$, $n = 0, 1, 2, \ldots$, in the plane wave basis e^{-imp_1} (eigenstates of x_1). The integer m is restricted to the values $1, 2, \ldots M$, with M an even integer that sets the system size. As initial condition we choose

$$\chi_q(x_1, 0) = \delta_{x_1,x_0}\boldsymbol{\Sigma}, \tag{7.17}$$

spatially localized at $x_0 = M/2$. The vector $\boldsymbol{\Sigma}$ is a normalized vector of rank 4 with random components denoting the spin and orbital degrees of freedom.

The multiplication with the Floquet operators, represented by $M \times M$ unitary matrices, can be done very efficiently by means of the Fast Fourier Transform algorithm. (See the analogous calculation in the QHE for a more detailed exposition [21].) The calculation is repeated for different values of α and q, to simulate a disorder average. The disorder strength can be varied by varying K, with *small* K corresponding to *strong* disorder.

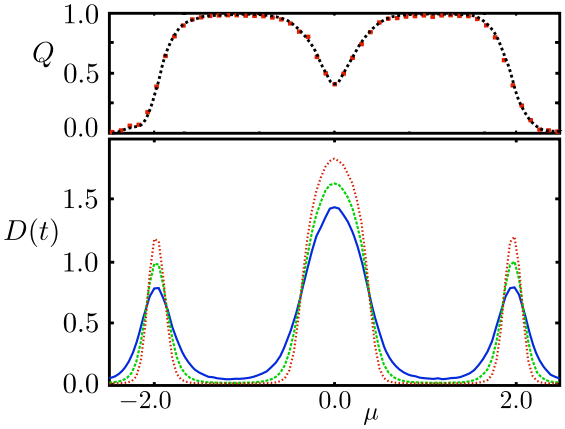

Figure 7.2. *Bottom panel:* Time-dependent diffusion coefficient (7.19) as a function of μ for $K = 2$, $\beta = 0.8$, $\gamma = 2$, shown for times $t = 10^6$ (red), $t = 10^5$ (green) and $t = 10^4$ (blue). The points of intersection of these curves locate the metal-insulator transition. *Top panel:* Topological quantum number (7.20) for the same parameter values, used to distinguish the topologically trivial ($Q = 0$) and nontrivial ($Q = 1$) insulators. In the metallic regions Q is not quantized.

7.3 Phase diagram with disorder

Before embarking on a calculation of the scaling law and critical exponents, we first locate the metal-insulator transitions and identify the topological phases.

To find the metal-insulator transitions, we calculate the time dependent diffusion coefficient

$$D(t) = \frac{\Delta^2(t)}{t} \tag{7.18}$$

from the mean squared displacement

$$\Delta^2(t) = \overline{\langle \big(x_1(t) - x_0\big)^2 \rangle}. \tag{7.19}$$

The brackets $\langle \cdots \rangle$ denote the expectation value in the state $\chi_q(x_1, t)$ and the overline indicates the ensemble average over α and q. We typically average over 10^3 samples of size $M = 4 \cdot 10^3$.

A representative series of scans of D versus μ for different values of t is shown in Fig. 7.2 (bottom panel). In Fig. 7.3 we show D versus t for different μ. In the insulating phase $D(t) \propto 1/t$ decays with

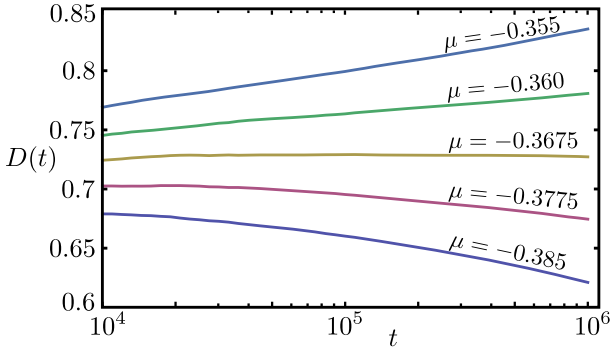

Figure 7.3. Time-dependent diffusion coefficient as a function of t for several values of μ near the metal–topological-insulator transition. (Same parameters as in Fig. 7.2.) The slope vanishes at the transition point $\mu_c \approx -0.368$.

increasing time, while in the metallic phase $D(t) \propto \ln t$ grows with increasing time [29]. The metal-insulator transition at $\mu = \mu_c$ is signaled by a t-independent $D(t)$ (corresponding to a scale invariant diffusion coefficient).

In this way we can locate the phase boundaries, but we cannot yet distinguish topologically trivial and nontrivial insulators. For that purpose we need the topological quantum number. The formula (7.6) for the topological quantum number of the translationally invariant system does not apply for nonzero disorder potential. The scattering formulation [23, 24] continues to apply and is what we will use. An alternative Hamiltonian formulation for disordered systems has been given by Prodan [30, 31].

The topological invariant is computed using the formalism described in Ref. 21. From the Floquet operator we can construct a reflection matrix $r(\varepsilon, \phi)$ for a cylindrical system enclosing a flux $\Phi = \phi\hbar/e$. The topological invariant then follows from the following combination of determinants and Pfaffians, evaluated at $\varepsilon = 0$ and $\phi = 0, \pi$,

$$(-1)^Q = \frac{\mathrm{Pf}\,[\sigma_y r(0,\pi)]}{\mathrm{Pf}\,[\sigma_y r(0,0)]} \frac{\sqrt{\det r(0,0)}}{\sqrt{\det r(0,\pi)}}. \tag{7.20}$$

The results in Fig. 7.2 (top panel) show the disorder-averaged μ-dependence of Q for a system of size $M \times M = 30 \times 30$. The value of Q is only quantized $\in \{0, 1\}$ in the insulating regions. In the metallic

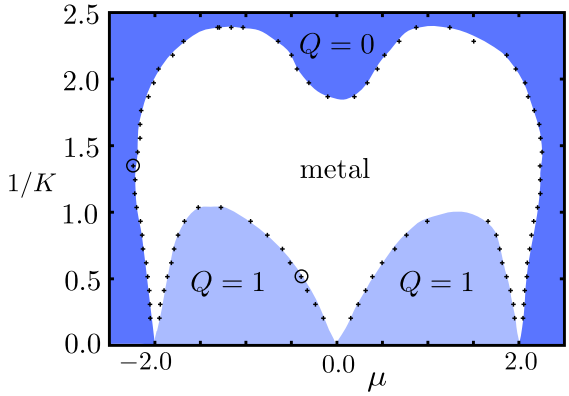

Figure 7.4. Phase diagram of the $\mathbb{Z}_2$ quantum kicked rotator in the μ–$1/K$ plane for fixed $\beta = 0.8$ and $\gamma = 2$. The topological quantum number $Q = 0, 1$ distinguishes the topologically trivial and nontrivial insulating phases. The metallic phase between the insulating phases disappears in the clean limit $1/K \to 0$. The two circles indicate the metal–trivial-insulator and metal–topological-insulator transitions that were studied to compare the critical exponents.

regions Q averages to $1/2$ for a sufficiently large system [23, 31], which is not quite observed for our system sizes.

The phase diagram obtained in this way is shown in Figs. 7.4 and 7.5. Without disorder, the topological invariant (7.9) gives a topological insulator for $|\mu| < 2$ and a trivial insulator for $|\mu| > 2$. With disorder a metallic phase appears between the insulating phases, provided that $\gamma/\beta \neq 0$. For small γ we find an additional trivial insulating phase around $\mu = 0$, consistent with what was found in the quantum Hall system in the presence of disorder [21].

In some other models of the QSHE a reentrant behavior $Q = 0 \mapsto 1 \mapsto 0$ with increasing disorder is observed in some regions of parameter space [31–34]. In our model a system which starts out topologically trivial in the clean limit stays trivial with disorder.

7.4 Scaling law and critical exponent

The premise of one-parameter scaling is expressed by the equation [35]

$$\ln D(t) = \mathcal{F}(\xi^{-2} t), \tag{7.21}$$

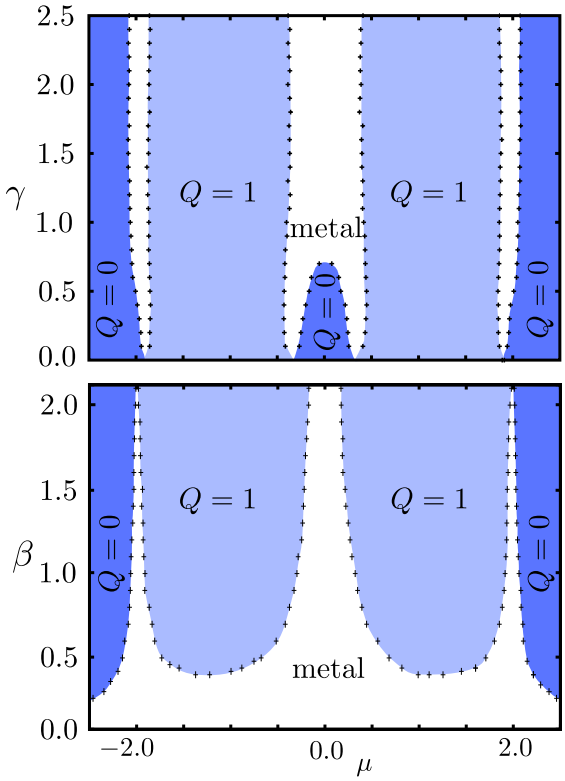

Figure 7.5. Phase diagram for fixed disorder strength ($K = 2$), in the μ–γ plane for $\beta = 0.8$ (top panel) and in the μ–β plane for $\gamma = 2$ (bottom panel). The metallic phase is stabilized by increasing the spin-orbit coupling strength γ or by decreasing β.

where $\mathcal{F}$ is a universal scaling function. The localization length ξ has a power law divergence $\propto |\mu - \mu_c|^{-\nu}$ at the metal-insulator transition, with critical exponent ν.

We follow the established method of finite-size (here: finite-time) scaling to extract ν from the numerical data [36]. We rewrite the scaling law (7.21) as

$$\ln D(t) = F(ut^{1/2\nu}), \tag{7.22}$$

$$u = (\mu - \mu_c) + \sum_{k=2}^{N_u} c_k \, (\mu - \mu_c)^k , \tag{7.23}$$

where $F(z)$ is an analytic function of $z = ut^{1/2\nu}$. By fitting the free

	N_u	N_F	N_s	ν	χ^2/ndf
ν_0	2	3	2	2.67 ± 0.09	0.97
ν_1	2	1	2	2.69 ± 0.06	0.92

Table 7.1. Results of the finite-time scaling analysis described in the text.

parameters of the series expansion

$$\ln D(t) = \ln D_c + \sum_{k=1}^{N_F} d_k \left(u t^{1/2\nu} \right)^k + S(t) \tag{7.24}$$

to the data for D as a function of μ and t, the critical exponent ν is obtained. The extra term $S(t)$ accounts for finite-time corrections to single-parameter scaling, of the form

$$S(t) = t^{-y} \sum_{k=0}^{N_s} g_k \left((\mu - \mu_c) t^{1/2\nu} \right)^k . \tag{7.25}$$

We have considered times up to $t = 10^6$ for system sizes up to $M = 10^4$. The number of terms N_u, N_F, and N_s in the series expansions (7.23)–(7.25) are systematically increased until the chi-square-value per degree of freedom (χ^2/ndf) is approximately unity, see Table 7.1. The calculation is carried out at the two points indicated by circles in Fig. 7.4, one a metal–trivial-insulator transition (giving $\nu_0 = 2.67 \pm 0.09$) and the other a metal–topological-insulator transition (giving $\nu_1 = 2.69 \pm 0.06$).

7.5 Conclusion

In conclusion, we have presented a numerical method to study the metal-insulator transition in the quantum spin Hall effect (QSHE), based on the incorporation of $\mathbb{Z}_2$ topological symmetry into the quantum kicked rotator. We find that the critical exponent ν_Q of the diverging localization length is the same whether the metal is approached from the topologically trivial insulator ($Q = 0$) or from the topologically nontrivial insulator ($Q = 1$). Our results $\nu_0 = \nu_1 \approx 2.7$ are in agreement with Refs. 11, 12, but not with Ref. 8 (which found a much smaller $\nu_1 \approx 1.6$ for the topologically nontrivial insulator). Since our stroboscopic model is fully

independent of the network model used in Refs. 11, 12, this is significant support for the insensitivity of ν to the topological quantum number Q.

A special feature of the quantum kicked rotator is that it allows the study of the QSHE, as well as the QHE [21], in one spatial dimension, by exchanging a dimension for an incommensurate driving frequency [17, 18]. There is much interest in such one-dimensional models of topological phases [37–40], because they might be more easily realized in optical lattices of cold atoms than the original two-dimensional models. Critical exponents were not studied in these earlier investigations, which focused on the QSHE in clean systems without disorder.

An interesting direction for future research is to study the edge states in the $\mathbb{Z}_2$ quantum kicked rotator, by replacing the periodic boundary condition used in this chapter by a zero-current boundary condition. While the localization length exponent ν does not depend on the topological quantum number, the edge state structure does depend on Q, with a characteristic multifractality at the metal-insulator transition [11].

Bibliography

[1] C. L. Kane and E. J. Mele, Phys. Rev. Lett. **95**, 146802 (2005); **95**, 226801 (2005).

[2] M. König, S. Wiedmann, C. Brüne, A. Roth, H. Buhmann, L. W. Molenkamp, X.-L. Qi, and S.-C. Zhang, Science **318**, 766 (2007)

[3] J. Maciejko, T. L. Hughes, and S.-C. Zhang, Ann. Rev. Cond. Mat. Phys. **2**, 31 (2011).

[4] M. Z. Hasan and C. L. Kane, Rev. Mod. Phys. **82**, 3045 (2010).

[5] X.-L. Qi and S.-C. Zhang, Rev. Mod. Phys. **83**, 1057 (2011).

[6] S. Hikami, A. I. Larkin, and Y. Nagaoka, Prog. Theor. Phys. **63**, 707 (1980).

[7] F. Evers and A. D. Mirlin, Rev. Mod. Phys. **80**, 1355 (2008).

[8] M. Onoda, Y. Avishai, and N. Nagaosa, Phys. Rev. Lett. **98**, 076802 (2007).

[9] Y. Asada, K. Slevin, and T. Ohtsuki, Phys. Rev. B **70**, 035115 (2004).

[10] P. Markoš, and L. Schweitzer, J. Phys. A **39**, 3221 (2006).

[11] H. Obuse, A. Furusaki, S. Ryu, and C. Mudry, Phys. Rev. B **76**, 075301 (2007); **78**, 115301 (2008).

[12] K. Kobayashi, T. Ohtsuki, and K. Slevin, arXiv:1201.0244.

[13] S. Ryu, C. Mudry, H. Obuse, and A. Furusaki, New J. Phys. **12**, 065005 (2010).

[14] G. Casati, B. V. Chirikov, F. M. Izrailev, and J. Ford, Lect. Notes Phys. **93**, 334 (1979).

[15] S. Fishman, D. R. Grempel, and R. E. Prange, Phys. Rev. Lett. **49**, 509 (1982).

[16] R. Scharf, J. Phys. A **22**, 4223 (1989)

[17] D. L. Shepelyansky, Physica D **8**, 208 (1983).

[18] G. Casati, I. Guarneri, and D. L. Shepelyansky, Phys. Rev. Lett. **62**, 345 (1989).

[19] G. Lemarié, H. Lignier, D. Delande, P. Szriftgiser, and J. C. Garreau, Phys. Rev. Lett. **105**, 090601 (2010).

[20] C. Tian, A. Altland, and M. Garst, Phys. Rev. Lett. **107**, 074101 (2011).

[21] J. P. Dahlhaus, J. M. Edge, J. Tworzydło, and C. W. J. Beenakker, Phys. Rev. B **84**, 115133 (2011).

[22] J. Chabé, G. Lemarié, B. Grémaud, D. Delande, P. Szriftgiser, and J. C. Garreau, Phys. Rev. Lett. **101**, 255702 (2008).

[23] I. C. Fulga, F. Hassler, and A. R. Akhmerov, Phys. Rev. B **85**, 165409 (2012).

[24] D. Meidan, T. Micklitz, and P. W. Brouwer, Phys. Rev. B **84**, 195410 (2011).

[25] S. Murakami, S. Iso, Y. Avishai, M. Onoda, and N. Nagaosa, Phys. Rev. B **76**, 205304 (2007).

[26] L. Fu and C. L. Kane, Phys. Rev. B **76**, 045302 (2007).

[27] B. A. Bernevig, T. L. Hughes, and S.-C. Zhang, Science **314**, 1757 (2006).

[28] F. Borgonovi and D.L. Shepelyansky, Physica D **109**, 24 (1997).

[29] Y. Asada, K. Slevin, and T. Ohtsuki, Physica E **34**, 228 (2006).

[30] E. Prodan, J. Phys. A **44**, 113001 (2011).

[31] E. Prodan, Phys. Rev. B **83**, 195119 (2011).

[32] J. Li, R.-L. Chu, J. K. Jain, and S.-Q. Shen, Phys. Rev. Lett. **102**, 136806 (2009).

[33] C. W. Groth, M. Wimmer, A. R. Akhmerov, J. Tworzydło, and C. W. J. Beenakker, Phys. Rev. Lett. **103**, 196805 (2009).

[34] A. Yamakage, K. Nomura, K. Imura, and Y. Kuramoto, J. Phys. Soc. Jpn. **80**, 053703 (2011).

[35] A. MacKinnon and B. Kramer, Z. Phys. B **53**, 1 (1983).

[36] K. Slevin and T. Ohtsuki, Phys. Rev. B **80**, 041304 (2009).

[37] T. Kitagawa, M. S. Rudner, E. Berg, and E. Demler, Phys. Rev. A **82**, 033429 (2010).

[38] N. H. Lindner, G. Refael, and V. Galitski, Nature Phys. **7**, 490 (2011).

[39] Y. E. Kraus, Y. Lahini, Z. Ringel, M. Verbin, and O. Zilberberg, Phys. Rev. Lett. **109**, 106402 (2012).

[40] F. Mei, S.-L. Zhu, Z.-M. Zhang, C. H. Oh, and N. Goldman, Phys. Rev. A **85**, 013638 (2012).

Chapter 8

Geodesic scattering by surface deformations of a topological insulator

8.1 Introduction

Topological insulators such as Bi_2Se_3 form a new class of materials, characterized by an insulating bulk and a conducting surface [1, 2]. The surface states are massless Dirac fermions with spin tied to momentum by spin-orbit coupling. Time-reversal symmetry prohibits backscattering and prevents disorder from localizing the surface states. The surface conductivity can therefore be unusually large, offering potential applications for electronics. The limitations on the conductivity of Dirac fermions imposed by random potential fluctuations are well understood (mostly from extensive studies of graphene [3]). Here we study an altogether different non-electrostatic scattering mechanism, originating from random surface deformations.

The epitaxial growth of Bi_2Se_3 films is known to produce random variations in the height profile $z = \zeta(x, y)$ of the surface [4]. These surface deformations correspond to terraces of additional layers of the material (of typical height $H = 2\,\text{nm}$ and width $W = 10\,\text{nm}$). Since the Dirac fermions are bound to the surface, they are forced to follow its geometry. Like photons in curved space-time, the electrons follow the geodesic or shortest path between two points, although here the curvature is purely spatial [5]. (The metric tensor of the surface does

not couple space to time.) The geodesic motion around deformations constitutes a scattering mechanism that by its very nature is energy independent, and which therefore is qualitatively different from potential scattering.

Our problem has no direct analogue in the context of graphene. Ripples of a graphene sheet do scatter the electrons, but this is not geodesic scattering: Ripples in graphene are described by gauge fields and scalar potentials in a *flat* space [3]. Space curvature effects may appear around conical defects (pentagon and heptagon rings), but these are rare in graphene [6]. An early study of geodesic scattering in condensed matter that we have found in the literature is by Dugaev and Petrov [7], with possible applications to intercalated layered crystals. The present work goes beyond their analysis by including the effects of an anisotropic dispersion relation, which is a major complication but relevant for topological insulators.

The chapter is organized as follows. In Sec. 8.2 we investigate the classical motion of the surface electrons in the presence of surface deformations. The geodesic equation is solved in the regime $H/W \ll 1$ of shallow deformations, to obtain the differential scattering cross section $\mathcal{S}$. In Sec. 8.3 we use the linearized Boltzmann integral equation to compute the conductivity tensor σ from $\mathcal{S}$. This is a notoriously difficult problem for an anisotropic dispersion relation [8]. In the regime $H/W \ll 1$ we are able to find a closed-form solution, by converting the integral equation into a differential equation. Results are given in Sec. 8.4 and in Sec. 8.5 we discuss the experimental signatures that distinguish geodesic scattering from potential scattering.

8.2 Geodesic scattering

8.2.1 Geodesic motion

We consider the surface of a topological insulator in the $x-y$ plane, deformed by a locally varying height $z = \zeta(x, y)$. The dispersion relation of a locally flat surface is an elliptical hyperboloid,

$$E = \sqrt{v_x^2 p_x^2 + v_y^2 p_y^2 + v_z^2 p_z^2 + \epsilon^2}, \tag{8.1}$$

where we have taken the x, y, z axes as the principal axes of the elliptical cone. In general, all three velocity components v_x, v_y, v_z may be

different. For an isotropic dispersion relation in the $x-y$ plane we have in-plane velocities $v_x = v_y = v_F$, but the out-of-plane velocity v_z may still differ.

We have included a mass term ϵ in Eq. (8.1) in order to have a nonzero Lagrangian,

$$L = \sum_i \dot{x}_i p_i - E = -\epsilon \sqrt{1 - \sum_i (\dot{x}_i / v_i)^2}, \tag{8.2}$$

with $\dot{x}_i = dx_i/dt = \partial E/\partial p_i$ and $i = x, y, z$. In the final equation of motion ϵ will drop out. The constraint that the motion follows the surface implies $\dot{z} = (\partial\zeta/\partial x)\dot{x} + (\partial\zeta/\partial y)\dot{y}$, which can be used to eliminate $\dot{z}$ from the Lagrangian. The result can be written in the form

$$L = -\epsilon \sqrt{1 - v_x^{-2} g_{\mu\nu} \dot{x}^\mu \dot{x}^\nu}, \tag{8.3}$$

with $g_{\mu\nu}$ the metric tensor (made dimensionless by pulling out a factor v_x^2). Summation over repeated indices $\mu, \nu = 1, 2 = x, y$ is implied and upper or lower indices distinguish contravariant or covariant vectors.

Explicitly, we find

$$g_{xx} = 1 + (\partial\zeta/\partial x)^2 v_{xz}^2, \tag{8.4a}$$
$$g_{yy} = v_{xy}^2 + (\partial\zeta/\partial y)^2 v_{xz}^2, \tag{8.4b}$$
$$g_{xy} = g_{yx} = (\partial\zeta/\partial x)(\partial\zeta/\partial y) v_{xz}^2, \tag{8.4c}$$

where we have abbreviated $v_{ij} = v_i/v_j$. The inverse of the tensor $g_{\mu\nu}$, denoted by $g^{\mu\nu}$, has elements

$$g^{xx} = D^{-1}[1 + (\partial\zeta/\partial y)^2 v_{yz}^2], \tag{8.5a}$$
$$g^{yy} = D^{-1}[v_{yx}^2 + (\partial\zeta/\partial x)^2 v_{yz}^2], \tag{8.5b}$$
$$g^{xy} = g^{yx} = -D^{-1}(\partial\zeta/\partial x)(\partial\zeta/\partial y) v_{yz}^2, \tag{8.5c}$$
$$D = 1 + (\partial\zeta/\partial x)^2 v_{xz}^2 + (\partial\zeta/\partial y)^2 v_{yz}^2. \tag{8.5d}$$

The Euler-Lagrange equation $\partial L/\partial x^\mu = (d/dt)\partial L/\partial \dot{x}^\mu$ gives the inhomogeneous geodesic equation [9, 10]

$$\ddot{x}^\lambda + \Gamma^\lambda_{\mu\nu} \dot{x}^\mu \dot{x}^\nu = \dot{x}^\lambda \frac{1}{L} \frac{dL}{dt}. \tag{8.6}$$

The coefficients $\Gamma^\lambda_{\mu\nu}$ are the Christoffel symbols,

$$\Gamma^\lambda_{\mu\nu} \equiv \frac{g^{\lambda\delta}}{2}\left(\frac{\partial}{\partial x^\nu}g_{\delta\mu} + \frac{\partial}{\partial x^\mu}g_{\delta\nu} - \frac{\partial}{\partial x^\delta}g_{\mu\nu}\right). \tag{8.7}$$

The nonzero right-hand-side in Eq. (8.6) may be eliminated by a reparameterization of time, from t to τ such that $d\tau/dt = -L(t)/\epsilon$. We thus arrive at the homogeneous geodesic equation

$$\frac{d^2x^\lambda}{d\tau^2} + \Gamma^\lambda_{\mu\nu}\frac{dx^\mu}{d\tau}\frac{dx^\nu}{d\tau} = 0. \tag{8.8}$$

Since ϵ does not appear in this equation of motion, it holds also in the limit of massless electrons.

8.2.2 Scattering angle

We consider the scattering from a surface deformation $\zeta(x, y)$ of characteristic width W and height H large compared to the Fermi wave length λ_F. The scattering may then be described by the classical equation of motion, which is the geodesic equation (8.8).

An electron with wave vector $\boldsymbol{k}$ incident on the deformation with impact parameter b at an angle $\theta_{\boldsymbol{k}}$ with the x-axis is scattered by an angle $\theta(\theta_{\boldsymbol{k}}, b)$, resulting in a differential scattering cross section $\mathcal{S}(\theta_{\boldsymbol{k}}, \theta) = |db/d\theta|$. Multiple trajectories may lead to the same scattering angle so that $\theta(\theta_{\boldsymbol{k}}, b)$ cannot be inverted. Then the function has to be split into several invertable branches i and the cross section becomes $\mathcal{S}(\theta_{\boldsymbol{k}}, \theta) = \sum_i |db_i(\theta_{\boldsymbol{k}}, \theta)/d\theta|$.

These quantities may be calculated by numerically solving the geodesic equation. Analytical progress is possible in the physically relevant regime $H/W \ll 1$ of shallow deformations. As shown in App. 8.A.2, the scattering angle is then given by

$$\theta(\theta_{\boldsymbol{k}}, b) = -\int_{-\infty}^{\infty} \tilde{\Gamma}^y_{xx}(\tilde{x}, b)d\tilde{x}. \tag{8.9}$$

Here $\tilde{\Gamma}^\lambda_{\mu\nu}(\tilde{x}, \tilde{y})$ is obtained from $\Gamma^\lambda_{\mu\nu}(x, y)$ by a rotation of the coordinate axes over an angle $\theta_{\boldsymbol{k}}$ (so that the electron is incident parallel to the $\tilde{x}$-axis). To leading order in H/W and b/W the scattering angle scales as $\theta = \mathcal{O}(H^2 b/W^3)$.

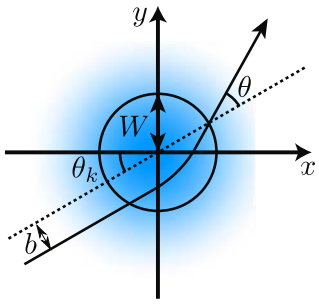

Figure 8.1. Geodesic trajectory of an electron deflected by a circularly symmetric deformation (characteristic width W). The impact parameter b, incident angle θ_k, and scattering angle θ are indicated. The blue background shows the height profile of the Gaussian deformation (8.10).

One simple example is the case of a Gaussian deformation,

$$\zeta(x,y) = H\exp[-(x^2+y^2)/2W^2], \tag{8.10}$$

which yields (see App. 8.A.3)

$$\begin{aligned}\theta(\theta_{\boldsymbol{k}},b) = &-\frac{\sqrt{\pi}}{2}\frac{H^2 v_{yz}}{W^3} b e^{-b^2/W^2} \\ &\times(\cos^2\theta_{\boldsymbol{k}} + v_{yx}^2\sin^2\theta_{\boldsymbol{k}}),\end{aligned} \tag{8.11}$$

in the shallow deformation limit. The geometry is depicted in Fig. 8.1. We will use this example throughout the chapter to illustrate our general results.

8.3 Calculation of the conductivity

8.3.1 Linearized Boltzmann equation

We investigate how geodesic scattering influences the surface conductivity σ of the topological insulator. We assume $\sigma \gg e^2/h$, so that we may use a semiclassical Boltzmann equation approach. In the presence of an external electric field $\boldsymbol{E}$, the occupation $f_{\boldsymbol{k}} = f_0(E_{\boldsymbol{k}}) + g_{\boldsymbol{k}}$ of the electron states deviates to first order in $\boldsymbol{E}$ according to the linearized Boltzmann equation,

$$\frac{\partial f_0}{\partial E_{\boldsymbol{k}}} e\boldsymbol{v}_{\boldsymbol{k}}\cdot\boldsymbol{E} = \sum_{\boldsymbol{k}'} Q(\boldsymbol{k},\boldsymbol{k}')(g_{\boldsymbol{k}} - g_{\boldsymbol{k}'}). \tag{8.12}$$

Here, $\boldsymbol{v}_{\boldsymbol{k}} = \partial\mathcal{E}_{\boldsymbol{k}}/\hbar\partial\boldsymbol{k}$ is the velocity and $Q(\boldsymbol{k},\boldsymbol{k}')$ the scattering rate from $\boldsymbol{k}$ to $\boldsymbol{k}'$ (equal to $Q(\boldsymbol{k}',\boldsymbol{k})$ because of detailed balance). The sum over $\boldsymbol{k}'$ runs over all states of the (d-dimensional) momentum space. In the continuum limit, $\sum_{\boldsymbol{k}} \to V\int d\boldsymbol{k}/(2\pi)^d$, where V is the d-dimensional volume ($d = 2$ in our case). Spin degrees of freedom do not contribute to the sum since the helical surface states have definite spin direction. Particle conservation leads to the normalization condition

$$\sum_{\boldsymbol{k}} g_{\boldsymbol{k}} = 0. \tag{8.13}$$

The electric field can be eliminated from Eq. (8.12) by means of the vector mean free path $\Lambda_{\boldsymbol{k}}$, defined by [8, 11]

$$g_{\boldsymbol{k}} = \frac{\partial f_0}{\partial E_{\boldsymbol{k}}} e\boldsymbol{E}\cdot\boldsymbol{\Lambda}_{\boldsymbol{k}}, \tag{8.14}$$

$$\sum_{\boldsymbol{k}'} Q(\boldsymbol{k},\boldsymbol{k}')(\boldsymbol{\Lambda}_{\boldsymbol{k}} - \boldsymbol{\Lambda}_{\boldsymbol{k}'}) = \boldsymbol{v}_{\boldsymbol{k}}. \tag{8.15}$$

For elastic scattering, $Q(\boldsymbol{k},\boldsymbol{k}') = \delta(\mathcal{E}_{\boldsymbol{k}} - \mathcal{E}_{\boldsymbol{k}'})q(\boldsymbol{k},\boldsymbol{k}')$. Using $d\boldsymbol{k} = dk_\perp\, dS_F = d\mathcal{E}_{\boldsymbol{k}} dS_F/|\hbar v_{\boldsymbol{k}}|$, with dS_F a Fermi surface element, Eq. (8.15) can be rewritten in terms of the density of states $N(\mathcal{E}_{\mathcal{F}})$ at the Fermi energy,

$$N(\mathcal{E}_F) = (2\pi)^{-d}\oint dS_F\,|\hbar\boldsymbol{v}_{\boldsymbol{k}}|^{-1}. \tag{8.16}$$

The integral $\oint dS_F$ extends over the Fermi surface. The result is

$$VN(\mathcal{E}_F)\langle q(\boldsymbol{k},\boldsymbol{k}')(\boldsymbol{\Lambda}_{\boldsymbol{k}} - \boldsymbol{\Lambda}_{\boldsymbol{k}'})\rangle_{\boldsymbol{k}'} = \boldsymbol{v}_{\boldsymbol{k}}, \tag{8.17}$$

with $\langle\cdots\rangle_{\boldsymbol{k}}$ denoting the weighted average over the Fermi surface,

$$\langle f(\boldsymbol{k})\rangle_{\boldsymbol{k}} = \frac{\oint dS_F\, f(\boldsymbol{k})|\hbar\boldsymbol{v}_{\boldsymbol{k}}|^{-1}}{\oint dS_F\,|\hbar\boldsymbol{v}_{\boldsymbol{k}}|^{-1}}. \tag{8.18}$$

The normalization condition (8.13) becomes $\langle\Lambda_{\boldsymbol{k}}\rangle_{\boldsymbol{k}} = 0$.

At zero temperature, the conductivity tensor is given by

$$\begin{aligned}\boldsymbol{\sigma} &= \frac{e^2}{V}\sum_{\boldsymbol{k}}\delta(\mathcal{E}_{\boldsymbol{k}} - \mathcal{E}_F)\,\boldsymbol{v}_{\boldsymbol{k}}\otimes\Lambda_{\boldsymbol{k}} \\ &= e^2 N(\mathcal{E}_F)\langle\boldsymbol{v}_{\boldsymbol{k}}\otimes\Lambda_{\boldsymbol{k}}\rangle_{\boldsymbol{k}}.\end{aligned} \tag{8.19}$$

The direct product $\otimes$ indicates the dyadic tensor with elements $[\boldsymbol{v}_k]_i[\boldsymbol{\Lambda}_k]_j$. Substitution of Eq. (8.17) for $\boldsymbol{v}_k$ and the use of $q(\boldsymbol{k},\boldsymbol{k}') = q(\boldsymbol{k}',\boldsymbol{k})$ shows that σ is a symmetric tensor.

For a low density $\mathcal{N}$ of scatterers, the scattering rate $q(\boldsymbol{k},\boldsymbol{k}')$ can be related to the differential cross section $\mathcal{S}$ of a single scatterer (averaged over all scatterers). In the two-dimensional case of interest here, the relation is

$$\mathcal{N}|\boldsymbol{v}_k|\mathcal{S}(\theta_k,\theta_{k'})d\theta_{k'} = q(\boldsymbol{k},\boldsymbol{k}')\frac{V}{(2\pi)^2}\frac{dS'_F}{|\hbar\boldsymbol{v}_{k'}|}, \tag{8.20}$$

where θ_k is the angle between $\boldsymbol{v}_k$ and the x-axis. The Eq. (8.17) which determines the vector mean free path then takes the form

$$\mathcal{N}|\boldsymbol{v}_k|\int_0^{2\pi} d\theta_{k'}\,\mathcal{S}(\theta_k,\theta_{k'})(\boldsymbol{\Lambda}_k - \boldsymbol{\Lambda}_{k'}) = \boldsymbol{v}_k. \tag{8.21}$$

For the solution of this equation (and the interpretation of the results), it is convenient to follow Ziman [8, 12] and define an anisotropic relaxation time $\tau(\boldsymbol{k})$ by

$$\frac{1}{\tau(\boldsymbol{k})} = V\,N(\mathcal{E}_F)\langle(1-\hat{v}_k\cdot\hat{v}_{k'})q(\boldsymbol{k},\boldsymbol{k}')\rangle_{k'}. \tag{8.22}$$

Using Eq. (8.20) this can be rewritten as

$$\frac{1}{\tau(\boldsymbol{k})} = \mathcal{N}|\boldsymbol{v}_k|\int_0^{2\pi} d\theta_{k'}\,\mathcal{S}(\theta_k,\theta_{k'})[1-\cos(\theta_{k'}-\theta_k)]. \tag{8.23}$$

8.3.2 Isotropic dispersion relation

For isotropic dispersion relations (when E_k depends only on $|\boldsymbol{k}|$, so that the velocity $\boldsymbol{v} = v_F\hat{k}$ is aligned with the wave vector), the linearized Boltzmann equation can be solved exactly [8]. This applies, for example, to surfaces perpendicular to the [111] direction of Bi_2Se_3. We consider this simplest case first.

Since the deformations do not have a preferred orientation and the dispersion is isotropic, the average scattering cross section $\mathcal{S}(\theta_k,\theta_{k'})$ only depends on the scattering angle $\theta = \theta_k - \theta_{k'}$, independently of the incident direction. The solution to Eq. (8.17) is then $\boldsymbol{\Lambda}_k = \tau\boldsymbol{v}_k$ with a relaxation time τ given by

$$\frac{1}{\tau} = \mathcal{N}v_F\int_0^{2\pi} d\theta\,\mathcal{S}(\theta)(1-\cos\theta). \tag{8.24}$$

Substitution into Eq. (8.19) leads to a scalar conductivity σ given by the Drude formula,

$$\sigma = e^2 N(\mathcal{E}_F) v_F^2 \frac{\tau}{d} = \frac{e^2}{h} \frac{\mathcal{E}_F}{\hbar} \frac{\tau}{2}. \tag{8.25}$$

In the second equality the density of states $N(\mathcal{E}_F) = \mathcal{E}_F / (2\pi\hbar^2 v_F^2)$ of a Dirac cone with a circular cross section was inserted.

The regime $H/W \ll 1$ of shallow surface deformations is characterized by predominantly forward scattering ($|\theta| \ll 1$). Then the relaxation time (8.24) is given by the second moment of the scattering angle,

$$\frac{1}{\tau} = \tfrac{1}{2} \mathcal{N} v_F \int d\theta \, \mathcal{S}(\theta) \theta^2. \tag{8.26}$$

We substitute the relation $\mathcal{S}(\theta) = \langle |d\theta(b)/db|^{-1} \rangle$, where $\langle \cdots \rangle$ indicates an average over the (randomly oriented) scatterers. The integration over scattering angles θ becomes an integration over impact parameters b,

$$\frac{1}{\tau} = \tfrac{1}{2} \mathcal{N} v_F \left\langle \int db \, \theta^2(b) \right\rangle. \tag{8.27}$$

From Eq. (8.9) we infer the scaling $1/\tau \propto W \times (H/W)^4$ of the relaxation rate with the characteristic height and width of the surface deformations. (The additional factor of W comes from the integral over b.) This scaling was first obtained by Dugaev and Petrov [7]. Eq. (8.25) then gives the scaling of the conductivity

$$\sigma = \text{constant} \times \frac{e^2}{h} \frac{\mathcal{E}_F}{\hbar} \frac{1}{\mathcal{N} v_F} \frac{W^3}{H^4}. \tag{8.28}$$

8.3.3 Anisotropic dispersion relation

We now turn to the case of an anisotropic dispersion relation. There is then, in general, no closed-form solution of the linearized Boltzmann equation [13]. One widely used approximation for the conductivity, due to Ziman [12], has the form

$$\boldsymbol{\sigma}_{\text{Ziman}} = e^2 N(\mathcal{E}_F) \langle \boldsymbol{v}_{\boldsymbol{k}} \otimes \boldsymbol{v}_{\boldsymbol{k}} \tau(\boldsymbol{k}) \rangle_{\boldsymbol{k}}, \tag{8.29}$$

with $\tau(\boldsymbol{k})$ the anisotropic relaxation time (8.22). As we will show in the following, this is a poor approximation for our problem, but fortunately

it is not needed: In the relevant limit $H/W \ll 1$ of scattering from shallow surface deformations an exact solution becomes possible. For shallow deformations forward scattering dominates, $|\theta| = |\theta_{\boldsymbol{k}} - \theta_{\boldsymbol{k}'}| \ll 1$. This allows for an expansion of $\boldsymbol{\Lambda}_{\boldsymbol{k}'}$ around $\theta_{\boldsymbol{k}}$, which reduces the integral equation (8.17) to a differential equation.

With the notation

$$M_p(\phi) = \int_0^{2\pi} d\theta\, \mathcal{S}(\phi, \phi+\theta)\theta^p, \tag{8.30}$$

the expansion to second order of Eq. (8.21) can be written as

$$M_1(\phi)\frac{d}{d\phi}\lambda(\phi) + \tfrac{1}{2}M_2(\phi)\frac{d^2}{d\phi^2}\lambda(\phi) = -\frac{1}{\mathcal{N}}e^{i\phi}. \tag{8.31}$$

We introduced a complex variable $\lambda = \Lambda_x + i\Lambda_y$ to combine the two components of the vector mean free path. Denoting the radius of curvature of the Fermi surface by $\kappa(\phi) = dS_F/d\phi$, the normalization condition (8.13) becomes

$$\int_0^{2\pi} d\phi\, \frac{\kappa(\phi)}{v(\phi)}\lambda(\phi) = 0. \tag{8.32}$$

Once we have the solution of Eq. (8.31), the conductivity tensor elements follow from

$$\sigma_{xx} \pm \sigma_{yy} = \frac{e^2}{h}\mathrm{Re}\int_0^{2\pi}\frac{d\phi}{2\pi}\, e^{\mp i\phi}\kappa(\phi)\lambda(\phi), \tag{8.33a}$$

$$\sigma_{xy} = \sigma_{yx} = \frac{e^2}{h}\tfrac{1}{2}\mathrm{Im}\int_0^{2\pi}\frac{d\phi}{2\pi}\, e^{i\phi}\kappa(\phi)\lambda(\phi). \tag{8.33b}$$

A further simplification is possible if the average scattering angle vanishes, $M_1(\phi) = 0$. Then the second moment $M_2(\phi)$ of the scattering angle is, within the forward scattering approximation, directly related to the anisotropic relaxation time:

$$\frac{1}{\tau(\phi)} = \tfrac{1}{2}\mathcal{N}v(\phi)M_2(\phi). \tag{8.34}$$

Eq. (8.31) can now be solved in terms of the Fourier transforms

$$\ell_n = \int_0^{2\pi} \frac{d\phi}{2\pi}\, e^{-in\phi} v(\phi)\tau(\phi), \tag{8.35a}$$

$$\kappa_n = \int_0^{2\pi} \frac{d\phi}{2\pi}\, e^{-in\phi} \kappa(\phi), \tag{8.35b}$$

$$\lambda_n = \int_0^{2\pi} \frac{d\phi}{2\pi}\, e^{-in\phi} \lambda(\phi), \tag{8.35c}$$

resulting in

$$\lambda_n = \frac{\ell_{n-1}}{n^2} + \text{constant} \times \delta_{n,0}. \tag{8.36}$$

The normalization constant can be determined from Eq. (8.32).

Inserting the solution into Eq. (8.33) we obtain the conductivity

$$\sigma_{xx} \pm \sigma_{yy} = \frac{e^2}{h}\, \mathrm{Re} \sum_{n=-\infty}^{\infty} \frac{\ell_{n-1}\kappa_{-n\pm1}}{n^2}, \tag{8.37a}$$

$$\sigma_{xy} = \sigma_{yx} = \frac{e^2}{h}\, \tfrac{1}{2}\, \mathrm{Im} \sum_{n=-\infty}^{\infty} \frac{\ell_{n-1}\kappa_{-n-1}}{n^2}. \tag{8.37b}$$

For simplicity we have assumed an inversion symmetric Fermi surface, for which $\kappa_{\pm1} = 0$ so that the normalization constant in Eq. (8.36) does not contribute to the conductivity.

In the case of an isotropic Fermi surface, only the Fourier components $l_0 = v_F\tau$ and $\kappa_0 = k_F$ are nonzero. From Eq. (8.37), we then find $\sigma_{xy} = 0 = \sigma_{yx}$, $\sigma_{xx} = \sigma_{yy} = (e^2/2h)k_F v_F \tau$, in agreement with Eq. (8.25).

Comparing with the Ziman approximation (8.29) for the conductivity in terms of the anisotropic relaxation time, we see that it can be written in the same form (8.37), but without the factor $1/n^2$. It therefore deviates strongly from our forward-scattering limit, except in the case of an isotropic Fermi surface (when only $n = 1$ contributes).

8.4 Results

8.4.1 Isotropic dispersion relation

In the shallow deformation limit the conductivity is given by Eq. (8.28), up to a numerical prefactor of order unity. We have calculated this

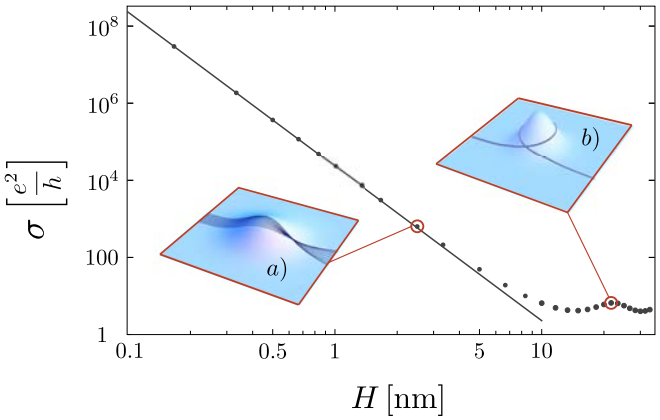

Figure 8.2. Surface conductivity of a topological insulator as a function of the height H of randomly positioned Gaussian deformations (width $W = 10\,\mathrm{nm}$, density $\mathcal{N} = 0.1\,W^{-2}$). We took an isotropic dispersion relation, with in-plane velocities $v_x = v_y = v_F = 5 \cdot 10^5$ m/s, and a smaller out-of-plane velocity $v_z = v_F/3$. The Fermi energy is fixed at $\mathcal{E}_F = 150$ meV. As discussed in Sec. 8.5, these are realistic parameter values for the [111] surface of Bi_2Se_3. Dots represent numerical results whereas the line shows the shallow deformation limit (8.38).

prefactor for Gaussian deformations of the form (8.10), randomly distributed over the surface. We assume that the deformations are shallow, $H/W \ll 1$. For simplicity, we also take the same parameters H and W for each deformation. From Eqs. (8.11), (8.25), and (8.27) we obtain the result

$$\sigma = \frac{16\sqrt{2}}{\pi\sqrt{\pi}} \frac{\mathcal{E}_F}{\hbar v_F \mathcal{N}} \frac{W^3}{(H v_F/v_z)^4} \frac{e^2}{h}. \tag{8.38}$$

The factor v_F/v_z is there to allow for an out-of-plane velocity v_z that is different from the in-plane velocity $v_x = v_y = v_F$. The result (8.38) confirms the scaling behavior (8.28) and gives the numerical prefactor.

To relax the assumption $H/W \ll 1$ of shallow deformations, we solved the geodesic equation (8.8) numerically for the Gaussian case. The corresponding Christoffel symbols were taken from Eq. (8.48) with $v_x = v_y = v_F$. Using the scattering angle $\theta(b)$ that we obtained from the numerics, we calculated the conductivity following from Eqs. (8.24, 8.25).

As shown in Fig. 8.2, the numerical results deviate from the scaling (8.38) only for relatively large ratios $H/W \gtrsim 0.5$. The deviations are

oscillatory, due to electron trajectories that circle around the deformation as depicted in the inset (b) of Fig. 8.2. Inset (a) shows generic trajectories for electrons scattering off a shallow Gaussian deformation. Notice the focussing of trajectories as an analogue of gravitational lensing.

8.4.2 Anisotropic dispersion relation

As an example of an anisotropic dispersion relation, we consider elliptic equi-energy contours $\mathcal{E}_{\boldsymbol{k}} = \hbar(v_x^2 k_x^2 + v_y^2 k_y^2)^{1/2}$ with principal axes x and y. As in the previous subsection, we investigate shallow Gaussian surface deformations. These have zero average scattering angle, $M_1(\phi) = 0$, and second moment

$$M_2(\phi) = \frac{1}{C}(\sin^2\phi + v_{yx}^2 \cos^2\phi)^2. \tag{8.39}$$

The coefficient C is given by

$$C = \frac{16\sqrt{2}}{\pi\sqrt{\pi}} \frac{W^3}{H^4 v_y^4 / v_z^4}. \tag{8.40}$$

From Eq. (8.58) we deduce that Eq. (8.39) actually holds more generally for any circularly symmetric deformation, the only difference being in the expression for C.

Using Eqs. (8.34) and (8.35a) one obtains the Fourier coefficients

$$\ell_{\pm n} = \frac{C}{\mathcal{N}} \left(\frac{1 - v_{yx}}{1 + v_{yx}}\right)^{|n|/2} \frac{(1 + |n| v_{yx} + v_{yx}^2)}{v_{yx}^3} \tag{8.41}$$

for n even, and zero for n odd. The elliptic dispersion relation leads to

$$\kappa(\phi) = \frac{\mathcal{E}_F}{\hbar v_x} \frac{v_{yx}}{(\sin^2\phi + v_{yx}^2 \cos^2\phi)^{3/2}}. \tag{8.42}$$

The Fourier coefficients κ_n are also nonzero only for n even. (Since their expressions are rather lengthy, we do not list them here.)

From Eq. (8.37) we find that the off-diagonal components of the conductivity tensor vanish, while the diagonal components are given by

$$\sigma_{\substack{\{xx\} \\ \{yy\}}} = \frac{e^2}{h} \sum_{n \geq 1} \frac{1}{2n^2} (\ell_{n+1} \pm \ell_{n-1})(\kappa_{n+1} \pm \kappa_{n-1}). \tag{8.43}$$

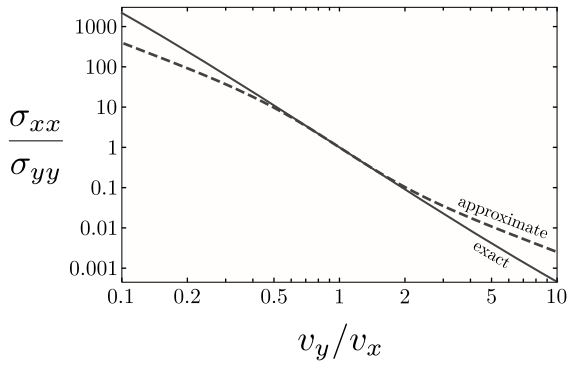

Figure 8.3. The solid line shows the ratio of conductivities σ_{xx}/σ_{yy} as a function of anisotropy v_y/v_x, calculated from Eq. (8.43). The dashed line corresponds to the Ziman approximation.

The series converges rapidly.

The ratio σ_{xx}/σ_{yy} depends only on the anisotropy $v_{yx} = v_y/v_x$. It is plotted in Fig. 8.3. For comparison, we also show the Ziman approximation σ_{Ziman} (obtained from the forward-scattering limit (8.43) without the $1/n^2$ factor). As expected, it deviates substantially upon increasing the anisotropy (notice the logarithmic scale).

8.5 Comparison with potential scattering

8.5.1 Carrier density dependence

The energy independence of the mean free path $\ell = v_F\tau$ is the hallmark of geodesic scattering. It implies the *square root* dependence dependence $\sigma \propto \sqrt{n}$ of the conductivity on the surface electron density n. This follows from Eq. (8.28) with $\mathcal{E}_F = \hbar v_F\sqrt{4\pi n}$ for an isotropic Dirac cone, or more generally from the scaling $\sigma \propto S_F$ for a noncircular Fermi surface (of area $S_F \propto \sqrt{n}$).

As discussed in the context of graphene [3, 14], electrostatic potential scattering typically gives a faster increase of the conductivity with increasing carrier density. Coulomb scattering from charged impurities and resonant scattering from short-range impurities both give a linear increase $\sigma \propto n$ (up to logarithmic factors). Scattering from a potential landscape with a Gaussian correlator gives an even more rapid increase

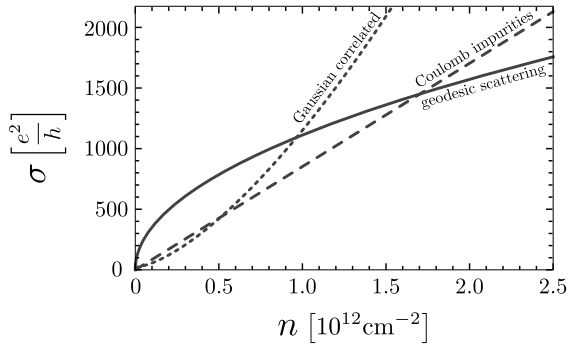

Figure 8.4. Conductivity as a function of carrier density. The influence of three different sources of scattering is shown: surface deformations (solid line), unscreened Coulomb impurities (dashed line) and Gaussian correlated potential fluctuations (dotted line). The parameters used for the plot are given in the text.

$\sigma \propto n^{3/2}$. Geodesic scattering, with $\sigma \propto n^{1/2}$, would therefore form the dominant conduction-limiting scattering mechanism at high carrier densities.

For a quantitative comparison of geodesic and potential scattering, we consider the [111] surface of Bi_2Se_3 with Gaussian deformations given by Eq. (8.38). We take isotropic in-plane velocities $v_x = v_y = v_F = 5 \cdot 10^5\,\mathrm{m/s}$ and a smaller out-of-plane velocity $v_z = v_F/3$ [15, 16]. We adopt the following numerical parameters for the deformations from an experimental image [4]: characteristic width $W = 10$ nm and height $H = 2$ nm, covering 40% of the surface area so $\mathcal{N} = 10^{11}\,\mathrm{cm}^{-2}$. The carrier density dependence of the conductivity for geodesic scattering, following from Eq. (8.38), is plotted in Fig. 8.4 (solid curve).

To compare the geodesic scattering to typical potential scatterers, we also show the corresponding results for scattering from charged impurities (dashed) and Gaussian potential fluctuations (dotted) in Fig. 8.4.

For charged impurities (charge $Q = e$) we considered the unscreened Coulomb potential $U(\boldsymbol{r}) = (Qe/4\pi\epsilon_0\epsilon_r)|\boldsymbol{r}|^{-1}$, as the extreme case of a long-ranged potential. We took $\epsilon_r = 80$ as a typical value for the dielectric constant and kept the other parameter values as before. The

semiclassical conductivity is then given by [3, 17]

$$\sigma = \frac{e^2}{h}\frac{n}{\mathcal{N}_c}\frac{2\pi\hbar^2 v_F^2}{u_0^2}, \quad u_0 = \frac{Qe}{4\epsilon_0\epsilon_r}. \tag{8.44}$$

For Fig. 8.4 we used $\mathcal{N}_c = 2.5 \times 10^{11}$ cm^{-2} as the density of impurities.

For a potential landscape with Gaussian correlator (range ξ, dimensionless strength U_0),

$$\langle U(\boldsymbol{r})U(\boldsymbol{r}')\rangle = \frac{U_0(\hbar v_F)^2}{2\pi\xi^2}\exp\left(-\frac{|\boldsymbol{r}-\boldsymbol{r}'|^2}{2\xi^2}\right), \tag{8.45}$$

the conductivity takes the functional form [18]

$$\sigma = \frac{e^2}{h}\frac{4\pi n\xi^2 e^{4\pi n\xi^2}}{U_0 I_1(4\pi n\xi^2)}. \tag{8.46}$$

(The function I_1 is a Bessel function.) For Fig. 8.4 we took $U_0 = 0.1$ and $\xi = W = 10\,\text{nm}$.

The parameter values used in Fig. 8.4 are only for the purpose of illustration, but the point to make is that geodesic scattering dominates over potential scattering for large carrier densities.

8.5.2 Anisotropy dependence of conductivity

In the case of an anisotropic (elliptical) dispersion relation the conductivity will be direction dependent. This situation arises for example if the surface of Bi_2Se_3 is not in the [111] direction. Geodesic scattering implies a certain universality for the directionality dependence of the conductivity, if we may assume that the surface deformations are shallow ($H/W \ll 1$) and without a preferential orientation (circularly symmetric on average). The ratio σ_{xx}/σ_{yy} is then only a function of v_y/v_x, independent of other parameters (such as electron density or density and height of the deformations). This universal function is plotted in Fig. 8.3 (solid curve).

In Fig. 8.5 we compare this result for geodesic scattering with corresponding results for potential scattering. Three typical impurity potentials are considered, of different range: long-ranged unscreened Coulomb potentials, medium-ranged Gaussian potential fluctuations, and short-ranged potentials. The conductivities are obtained following the general approach of Ref. 19, by first computing the transition rates in Born

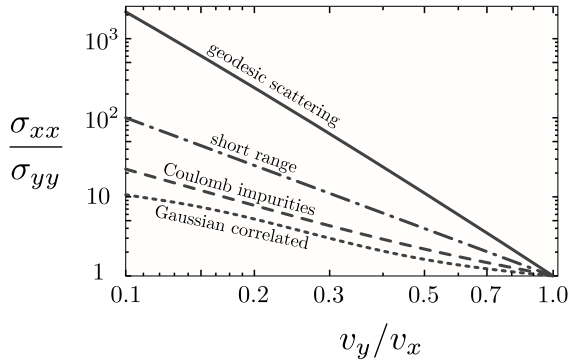

Figure 8.5. Ratios of conductivities along the two main axes of the dispersion relation are shown as a function of anisotropy v_y/v_x. The influence of four different sources of scattering is shown: surface deformations (solid line), unscreened Coulomb impurities (dashed line), Gaussian potential fluctuations (dotted line), and short-ranged potentials (dot-dashed line). The parameters used for the plot are given in the text.

approximation and then solving numerically the linearized Boltzmann equation. We took the same material parameter values as in the previous subsection.

The unscreened Coulomb potential gives a ratio σ_{xx}/σ_{yy} which depends only on v_y/v_x (dashed line). For Gaussian potential fluctuations, the ratio σ_{xx}/σ_{yy} is a function of both v_y/v_x and n. It is plotted as a dotted line in Fig. 8.5 for $n\xi^2 = 1$. (If $\xi = W = 10$ nm this corresponds to the carrier density $n = 10^{12}$ cm^{-2}.) In the same figure we also plot (dot-dashed line) the limit $\xi \to 0$ (at fixed n) of a short-ranged potential.

From the double-logarithmic plot in Fig. 8.5 one can see that there is an approximate power law dependence, $\sigma_{xx}/\sigma_{yy} \propto (v_y/v_x)^{-p}$, over at least one decade. The exponent is $p \approx 3.3$ for geodesic scattering, while $p = 2$ for short-range potential scattering. Scattering from long-ranged Coulomb impurities or from medium-ranged Gaussian potential fluctuations gives $p < 2$.

Anisotropic charge transport in the presence of unscreened Coulomb impurities for an elliptic dispersion relation was also discussed in the context of strained graphene [20]. There it was argued that $\sigma_{xx}/\sigma_{yy} \propto (v_y/v_x)^{-2}$ on the basis of a power-counting argument. Our numerical solution of the Boltzmann equation gives a smaller exponent $p \approx 1.3$ in that case.

To conclude, charge transport dominated by surface deformations has a much stronger anisotropy dependence than that governed by impurity potentials. This highly anisotropic transport behavior is a distinct characteristic of geodesic scattering.

Appendix 8.A Calculation of scattering cross section

8.A.1 Christoffel symbols in rotated basis

In order to calculate the scattering angle in the geometry of Fig. 8.1, it is convenient to rotate the coordinate axis in the $x-y$ plane such that the electron is incident parallel to the x-axis. Under the linear transformation from x, y to $\tilde{x} = x\cos\theta_k + y\sin\theta_k$, $\tilde{y} = -x\sin\theta_k + y\cos\theta_k$, the Christoffel symbol $\Gamma^{\lambda}_{\mu\nu}$ transforms to

$$\tilde{\Gamma}^{\lambda}_{\mu\nu}(\tilde{x},\tilde{y}) = \frac{\partial\tilde{x}^{\lambda}}{\partial x^{\lambda'}}\Gamma^{\lambda'}_{\mu'\nu'}(x,y)\frac{\partial x^{\mu'}}{\partial\tilde{x}^{\mu}}\frac{\partial x^{\nu'}}{\partial\tilde{x}^{\nu}}. \tag{8.47}$$

Using the expressions (8.4), (8.5), (8.7) for metric tensor and Christoffel symbols, we arrive at

$$\tilde{\Gamma}^{x}_{\mu\nu} = D^{-1}\frac{\partial^2\zeta}{\partial\tilde{x}^{\mu}\partial\tilde{x}^{\nu}}\left[v_{xz}^2\frac{\partial\zeta}{\partial\tilde{x}} - (v_{xz}^2 - v_{yz}^2)\sin\theta_k\left(\frac{\partial\zeta}{\partial\tilde{x}}\sin\theta_k + \frac{\partial\zeta}{\partial\tilde{y}}\cos\theta_k\right)\right], \tag{8.48a}$$

$$\tilde{\Gamma}^{y}_{\mu\nu} = D^{-1}\frac{\partial^2\zeta}{\partial\tilde{x}^{\mu}\partial\tilde{x}^{\nu}}\left[v_{yz}^2\frac{\partial\zeta}{\partial\tilde{y}} - (v_{xz}^2 - v_{yz}^2)\sin\theta_k\left(\frac{\partial\zeta}{\partial\tilde{x}}\cos\theta_k - \frac{\partial\zeta}{\partial\tilde{y}}\sin\theta_k\right)\right]. \tag{8.48b}$$

The factor D from Eq. (8.5d), written in terms of the rotated coordinates, reads

$$D = 1 + v_{xz}^2\left(\frac{\partial\zeta}{\partial\tilde{x}}\cos\theta_k - \frac{\partial\zeta}{\partial\tilde{y}}\sin\theta_k\right)^2 + v_{yz}^2\left(\frac{\partial\zeta}{\partial\tilde{x}}\sin\theta_k + \frac{\partial\zeta}{\partial\tilde{y}}\cos\theta_k\right)^2. \tag{8.49}$$

The Christoffel symbols (8.48) appear in the geodesic equation for the rotated coordinates,

$$\frac{d^2\tilde{x}^{\lambda}}{d\tau^2} + \tilde{\Gamma}^{\lambda}_{\mu\nu}\frac{d\tilde{x}^{\mu}}{d\tau}\frac{d\tilde{x}^{\nu}}{d\tau} = 0. \tag{8.50}$$

8.A.2 Geodesic equation for shallow deformation

The geodesic equation (8.50) can be considerably simplified in the shallow deformation limit $H/W \ll 1$. Let us consider a particle incident on a deformation along the $\tilde{x}$-direction from $-\infty$ with impact parameter b and velocity

$$v = v_x v_y (v_y^2\cos^2\theta_k + v_x^2\sin^2\theta_k)^{-1/2}. \tag{8.51}$$

Since the derivative $d\tilde{y}/d\tau$ is smaller than $d\tilde{x}/d\tau$ by a factor $(H/W)^2$, we can drop this derivative from the geodesic equation. The result is

$$\frac{d^2\tilde{x}}{d\tau^2} + \tilde{\Gamma}^x_{xx}\left(\frac{d\tilde{x}}{d\tau}\right)^2 = 0, \tag{8.52a}$$

$$\frac{d^2\tilde{y}}{d\tau^2} + \tilde{\Gamma}^y_{xx}\left(\frac{d\tilde{x}}{d\tau}\right)^2 = 0. \tag{8.52b}$$

Furthermore, since $d\tilde{x}/d\tau = v[1 + \mathcal{O}(H/W)^2]$, we can write $d/d\tau = v\,d/d\tilde{x}$. This leads to

$$\frac{d^2\tilde{y}}{d\tilde{x}^2} = -\tilde{\Gamma}^y_{xx}. \tag{8.53}$$

The scattering angle $\theta \ll 1$ is obtained from $\theta = \lim_{\tilde{x}\to\infty} d\tilde{y}/d\tilde{x}$, hence

$$\theta(\theta_{\boldsymbol{k}}, b) = -\int_{-\infty}^{\infty} \tilde{\Gamma}^y_{xx}\, d\tilde{x}\,\big|_{\tilde{y}\to b}\,. \tag{8.54}$$

Inserting Eq. (8.48b) into Eq. (8.54) and noting that $D = 1 + \mathcal{O}(H/W)^2$, we obtain the scattering angle to leading order in H/W,

$$\theta(\theta_{\boldsymbol{k}}, b) = -\int_{-\infty}^{\infty} d\tilde{x}\,\left[\left(\alpha\frac{\partial\zeta}{\partial\tilde{y}} - \gamma\frac{\partial\zeta}{\partial\tilde{x}}\right)\frac{\partial^2\zeta}{\partial\tilde{x}^2}\right]_{\tilde{y}\to b}. \tag{8.55}$$

We abbreviated

$$\alpha = v_{yz}^2\cos^2\theta_{\boldsymbol{k}} + v_{xz}^2\sin^2\theta_{\boldsymbol{k}}, \tag{8.56a}$$

$$\gamma = (v_{xz}^2 - v_{yz}^2)\sin\theta_{\boldsymbol{k}}\cos\theta_{\boldsymbol{k}}. \tag{8.56b}$$

8.A.3 Circularly symmetric deformation

For a circularly symmetric height profile $\zeta(x, y)$, dependent only on $r = \sqrt{x^2+y^2} = \sqrt{\tilde{x}^2+\tilde{y}^2}$, the term proportional to γ in Eq. (8.55) vanishes (because it is an integral over an odd function of $\tilde{x}$). The expression for the scattering angle thus simplifies further to

$$\theta(\theta_{\boldsymbol{k}}, b) = -\alpha\int_{-\infty}^{\infty} dx\,\left[\frac{\partial\zeta}{\partial y}\,\frac{\partial^2\zeta}{\partial x^2}\right]_{y\to b}. \tag{8.57}$$

For the Gaussian deformation (8.10) we obtain the scattering angle (8.11) given in the main text.

The entire dependence of the scattering angle θ on the angle of incidence $\theta_{\boldsymbol{k}}$ is contained in the prefactor α. This implies that the moments $M_p = \int db\, \theta^p$ of the scattering angle depend on the angle of incidence as

$$M_p(\theta_{\boldsymbol{k}}) = c_p \alpha^p = c_p v_{xz}^p (\sin^2 \theta_{\boldsymbol{k}} + v_{yx}^2 \cos^2 \theta_{\boldsymbol{k}})^p, \tag{8.58}$$

with c_p a coefficient independent of $\theta_{\boldsymbol{k}}$.

Bibliography

[1] X.-L. Qi and S.-C. Zhang, Physics Today **63** (1), 33 (2010).

[2] M. Z. Hasan and C. L. Kane, Rev. Mod. Phys. **82**, 3045 (2010) .

[3] A. H. Castro Neto, F. Guinea, N. M. R. Peres, K. S. Novoselov, and A. K. Geim, Rev. Mod. Phys. **81**, 109 (2009).

[4] J. Chen, H. J. Qin, F. Yang, J. Liu, T. Guan, F. M. Qu, G. H. Zhang, J. R. Shi, X. C. Xie, C. L. Yang, K. H. Wu, Y. Q. Li, and L. Lu, Phys. Rev. Lett. **105**, 176602 (2010).

[5] D.-H. Lee, Phys. Rev. Lett. **103**, 196804 (2009).

[6] M. A. H. Vozmediano, M. I. Katsnelson, and F. Guinea, Physics Reports **496**, 109 (2010).

[7] V. K. Dugaev and P. P. Petrov, Phys. Lett. A **199**, 339 (1995).

[8] J. M. Ziman, *Principles of the Theory of Solids* (Cambridge University Press, Cambridge, 1972).

[9] C. W. Misner, K. S. Thorne, and J. A. Wheeler, *Gravitation* (W. H. Freeman and Company, New York, 1973).

[10] E. Bertschinger, Hamiltonian Dynamics of Particle Motion, MIT lecture notes in General Relativity, Physics Course 8.962 (1999), http://web.mit.edu/edbert/GR/.

[11] E. H. Sondheimer, Proc. R. Soc. Lond. A **268**, 100 (1962).

[12] J. M. Ziman, Adv. Phys. **10**, 1 (1961).

[13] I. Mertig, Rep. Prog. Phys. **62**, 237 (1999) .

[14] E. R. Mucciolo and C. H. Lewenkopf, J. Phys.: Condens. Matter **22**, 273201 (2010).

[15] Y. Xia, D. Qian, D. Hsieh, L. Wray, A. Pal, H. Lin, A. Bansil, D. Grauer, Y. S. Hor, R. J. Cava, and M. Z. Hasan, Nature Phys. **5**, 398 (2009).

[16] H. Zhang, C.-X. Liu, X.-L. Qi, X. Dai, Z. Fang, and S.-C. Zhang, Nature Phys. **5**, 438 (2009).

[17] K. Nomura and A.H. MacDonald, Phys. Rev. Lett. **98**, 076602 (2007).

[18] S. Adam, P. W. Brouwer, and S. Das Sarma, Phys. Rev. B **79**, 201404(R) (2009).

[19] R. S. Sorbello, J. Phys. F **47**, 503 (1974); **47**, 1665 (1974).

[20] V. M. Pereira, A. H. Castro Neto, and N. M. R. Peres, Phys. Rev. B **80**, 045401 (2009).

Samenvatting

Een topologische fase van de materie is bijzonder omdat zij optreedt zonder breking van enige symmetrie. De topologische fase is gekarakteriseerd door een zogenaamde topologische invariant — een geheel getal dat niet gevoelig is voor kleine verstoringen van de Hamiltoniaan. Een gevolg hiervan is dat de topologische fase geleidende oppervlaktetoestanden heeft, die niet gevoelig zijn voor wanorde en andere onvolkomenheden. Een verscheidenheid aan bijzondere transportverschijnselen treedt op tengevolge van de topologie. In dit werk onderzoeken wij het samenspel van topologie en onvolkomenheden, in het bijzonder met het oog op transportverschijnselen.

Het eerste deel van het proefschrift behandelt supergeleidende systemen, waar de topologie voor oppervlaktetoestanden zorgt die beschermd worden door de supergeleidende gap. De één-dimensionale topologische supergeleiders zijn vooral interessant. Zij kunnen gerealiseerd worden in samengestelde structuren van halfgeleiders en supergeleiders en bezitten gebonden Majorana-toestanden aan hun uiteinden — dat zijn deeltjes met energie nul die gelijk zijn aan hun anti-deeltje. Deze Majorana-toestanden zijn veelbelovend voor de realisatie van een topologisch quantumgeheugen.

De algemene transporteigenschappen van supergeleidende systemen en hun afhankelijkheid van symmetrie kan analytisch worden onderzocht met behulp van toevallig gekozen verstrooiingsmatrices. Met het oog hierop onderzoeken wij in hoofdstuk twee de supergeleidende circulaire ensembles van de toevalsmatrixtheorie. In het derde hoofdstuk generaliseren wij deze bekende ensembles door de fasen van verschillende topologie te onderscheiden. Dit stelt ons in staat om de invloed van topologie te bepalen op de supergeleidende transporteigenschappen. In het bijzonder onderzoeken wij of de Majorana-fermionen in de

Andreev-geleiding van NS-juncties tussen een normaal metaal en een supergeleider herkenbaar zijn.

In het vierde hoofdstuk wordt een experiment voorgesteld waarmee een topologische supergeleider onomstotelijk kan worden aangetoond, gebruik makend van een quantumpuntcontact dat aan een supergeleidende draad is bevestigd. De aanwezigheid van een topologische fase wordt aangegeven door de quantisatie van de geleiding in de limiet van een enkel geleidingskanaal. De niet-topologische (triviale) supergeleider, daarentegen, heeft dan geleidingsvermogen nul. Het voordeel van deze proef boven de gebruikelijke tunnelproef is een sterk verminderde gevoeligheid voor spanning en temperatuur.

In het vijfde hoofdstuk wenden we ons tot de zogenaamde nodale supergeleiders, en introduceren we een verstrooiingstheorie voor hun topologische eigenschappen. Hoewel zij geen gap hebben, kan men toch een verscheidenheid aan topologische eigenschappen definiëren, die zoals we zullen zien, een sterk effect hebben op de transporteigenschappen.

In het tweede deel van het proefschrift verschuift onze aandacht van de topologische supergeleiders naar de topologische isolatoren. In de eerste twee hoofdstukken van dit tweede deel behandelen we de localisatie van elektronen in de buurt van een topologische fase-overgang. In twee-dimensionale systemen zonder tijdomkeersymmetrie, zorgt wanorde voor localisatie van de golffuncties — de zogenaamde Andersonlocalisatie. Bij de topologische fase-overgang divergeert de localisatielengte met een universele kritische exponent.

In hoofdstuk zes introduceren we een nieuwe methode om deze delocalisatie te bestuderen in de universaliteitsklasse van het quantum Hall-effect. Deze zogenaamde stroboscopische methode is heel efficiënt voor numerieke berekeningen en maakt het mogelijk om meerdimensionale systemen te bestuderen in één ruimtelijke dimensie. In hoofdstuk zeven breiden we onze methode uit naar de universaliteitsklasse van het quantum spin-Hall-effect (een twee-dimensionaal systeem met tijdomkeersymmetrie). Het fasediagram verschilt van dat van het quantum Hall-effect, omdat de fase-overgang via een metallische fase optreedt. In beide universaliteitsklassen berekenen we de kritische exponent.

In het laatste hoofdstuk van het proefschrift gaan we over naar de drie-dimensionale topologische isolatoren, die gekenmerkt zijn door een

topologisch beschermd geleidend oppervlak. Omdat de elektronen het oppervlak moeten volgen, bewegen zij als het ware in een gekromde ruimte. Dan treedt zogenaamde geodesische verstrooiing op, die leidt tot een nieuwe bijdrage aan de oppervlakteweerstand ten gevolge van oppervlakteruwheid.

Summary

Topological phases of matter are exceptional because they do not arise due to a symmetry breaking mechanism. Instead they are characterized by topological invariants – integer numbers that are insensitive to small perturbations of the Hamiltonian. As a consequence they support conducting surface states that are protected against disorder and other imperfections. Furthermore, a variety of unusual transport properties arise due to the presence of topology. In this work the interplay between topology and sample imperfections is investigated with a focus on transport phenomena.

The first part of the thesis treats superconducting systems, where topology leads to boundary states that are protected by a superconducting gap. Among the topological superconductors, one-dimensional systems are of particular interest. They can be realized in semiconductor - superconductor heterostructures, and support Majorana bound states at their ends – zero energy particles that are their own anti-particles. These Majorana states are regarded as promising candidates for the realization of a topological quantum memory.

The generic transport properties of superconducting systems and their dependence on symmetries can be studied analytically using random scattering matrices. To this end, the superconducting circular ensembles of random-matrix theory are studied in chapter two. In the third chapter we generalize these known ensembles by distinguishing between phases of different topology. This enables us to determine the influence of topology on the superconducting transport properties. In particular the signatures of Majorana fermions in the Andreev conductance of disordered normal-superconductor (NS) junctions are analyzed.

The fourth chapter proposes a setup for the unambiguous detection of topological superconductivity: a quantum point contact attached to

a superconducting wire. The signature of the topological phase is a quantized conductance in the single-channel limit. In contrast, the conductance is forced to be zero for a trivial superconductor. The advantage of this setup over the usual tunnel contact setup is a strongly reduced sensitivity to finite voltage or temperature.

In the fifth chapter we move over to nodal superconductors, introducing a scattering formulation for their topology. Although they are gapless, a variety of lower dimensional topological invariants can be defined that, as we show, have strong impact on the transport properties of these systems.

In the second half of the thesis the focus shifts from topological superconductors to topological insulators. The first two chapters of this part are concerned with the localization properties of electrons close to topological phase transitions. In two-dimensional systems without time reversal symmetry, disorder forces the electronic wave functions to localize – a phenomenon called Anderson localization. At the topological phase transition the localization length of the wave function diverges with a universal critical exponent.

In chapter six we introduce a new approach to investigate this delocalization behavior in the quantum Hall universality class, using a stroboscopic model. This method is computationally efficient and makes it possible to study higher-dimensional systems in one spatial dimension. In chapter seven we extend our description to the quantum spin Hall universality class (two-dimensional systems with time-reversal symmetry). Its phase diagram is different from that of the quantum Hall effect, because the phase transition happens via a metallic phase. For both universality classes we calculate the critical exponent numerically.

In the final chapter of the thesis we go over to three-dimensional topological insulators, which are characterized by a topologically protected metallic surface. Since electrons moving on this surface are constrained to follow its geometry, they effectively live in a curved space and are thus subject to geodesic scattering. This leads to a novel contribution to the resistance of the surface, caused by surface roughness.

List of Publications

- *Spin current generation and detection by a double quantum dot structure*, J. P. Dahlhaus, S. Maier, and A. Komnik, Phys. Rev. B **81**, 075110 (2010).

- *Random-matrix theory of thermal conduction in superconducting quantum dots*, J. P. Dahlhaus, B. Béri, and C. W. J. Beenakker, Phys. Rev. B **82**, 014536 (2010) [Chapter 2].

- *Geodesic scattering by surface deformations of a topological insulator*, J. P. Dahlhaus, C.-Y. Hou, A. R. Akhmerov, and C. W. J. Beenakker, Phys. Rev. B **82**, 085312 (2010) [Chapter 8].

- *Quantized conductance at the Majorana phase transition in a disordered superconducting wire*, A. R. Akhmerov, J. P. Dahlhaus, F. Hassler, M. Wimmer, and C. W. J. Beenakker, Phys. Rev. Lett. **106**, 057001 (2011).

- *Random-matrix theory of Andreev reflection from a topological superconductor*, C. W. J. Beenakker, J. P. Dahlhaus, M. Wimmer, and A. R. Akhmerov, Phys. Rev. B **83**, 085413 (2011) [Chapter 3].

- *Quantum point contact as a probe of a topological superconductor*, M. Wimmer, A. R. Akhmerov, J. P. Dahlhaus, and C. W. J. Beenakker, New J. Phys. **13**, 053016 (2011) [Chapter 4].

- *Quantum Hall effect in a one-dimensional dynamical system*, J. P. Dahlhaus, J. M. Edge, J. Tworzydło, and C. W. J. Beenakker, Phys. Rev. B **84**, 115133 (2011) [Chapter 6].

- *Metal–topological-insulator transition in the quantum kicked rotator with $\mathbb{Z}_2$ symmetry*, E. P. L. van Nieuwenburg, J. M. Edge, J. P. Dahlhaus,

J. Tworzydło, and C. W. J. Beenakker, Phys. Rev. B **85**, 165131 (2012) [Chapter 7].

- *Andreev reflection from a topological superconductor with chiral symmetry*, M. Diez, J. P. Dahlhaus, M. Wimmer, and C. W. J. Beenakker, Phys. Rev. B **86**, 094501 (2012).

- *Zero-voltage conductance peak from weak antilocalization in a Majorana nanowire*, D. I. Pikulin, J. P. Dahlhaus, M. Wimmer, H. Schomerus, and C. W. J. Beenakker, submitted to New J. Phys.

- *Scattering theory of topological invariants in nodal superconductors*, J. P. Dahlhaus, M. Gibertini, and C. W. J. Beenakker, submitted to Phys. Rev. B [Chapter 5].

Curriculum Vitæ

I was born in Essen, Germany on the 31st of August 1982. In my first years my family moved several times before we settled in Neckargemünd in 1990, where I received my primary and the first part of my secondary school education. After finishing my school education 2002 in close-by Heidelberg, I studied Mathematics at the FernUniversität Hagen for one year while I did my alternative civilian service at a boarding school for disabled children.

In 2003 I started to study physics at the Ruprecht-Karls Universität Heidelberg. During the first years I was also enrolled in Mathematics, achieving an intermediate diploma in 2005. Shortly after I was granted a scholarship of the Studienstiftung des Deutschen Volkes. With financial support of the German Academic Exchange Service (DAAD) I obtained a Bachelor of Science (Degree with Honors) in physics at the University of Melbourne, Australia in 2007, performing research on *Non-linear laser-induced dynamics and high harmonic generation in electronic systems* under the supervision of Prof. Dr. Keith Nugent. With a thesis on *Interaction effects in the charge transfer statistics of double quantum dot nanostructures* in the group of Prof. Dr. Andreas Komnik I finished my diploma studies in Heidelberg in 2009. After graduation I joined the group of Prof. Dr. Carlo Beenakker at the Universiteit Leiden for my PhD studies, employed by the Foundation for Fundamental Research on Matter (FOM). Part of the research I performed during the last three years is presented in this thesis.

During my studies in Leiden, Heidelberg, and Melbourne I taught several classes on physics, mathematics, and computer science and supervised lab work. As a PhD student I attended a variety of summer schools, workshops, and conferences and presented my work in the Netherlands, Germany, France, Italy, and Japan.

Stellingen

behorende bij het proefschrift

Random-matrix theory and stroboscopic models of topological insulators and superconductors

1. The p-th cumulant of the N-mode conductance of a chaotic Andreev billiard is independent of the topological invariant for $p < N$.
   Chapter 3

2. Half-integer conductance quantization is a smoking-gun signature of Majorana zero-energy modes.
   Chapter 4

3. The quantum Hall phase transition can be studied in one spatial dimension.
   Chapter 6

4. Electrons on the surface of a topological insulator provide a condensed-matter application of both special and general relativity.
   Chapter 8

5. The determinant of the reflection matrix of a superconductor is a topological invariant.
   A. R. Akhmerov, J. P. Dahlhaus, F. Hassler, M. Wimmer, and C. W. J. Beenakker, Phys. Rev. Lett. **106**, 057001 (2011)

6. The expression $I = (2e/\hbar)dE/d\phi$ for the phase-dependent supercurrent $I(\phi)$ carried by a Majorana state of energy E, used in most papers on the topic, is wrong by a factor of two.
   C. W. J. Beenakker, D. I. Pikulin, T. Hyart, and J. P. Dahlhaus, arXiv:1210.5412

7. Because weak (anti-)localization is not destroyed by a magnetic field in the presence of Andreev reflection, it cannot be categorically ruled out as an explanation for the zero-bias conductance peak attributed to Majorana fermions.
   D. I. Pikulin, J. P. Dahlhaus, M. Wimmer, H. Schomerus, and C. W. J. Beenakker, arXiv:1206.6687

8. Nanowires that are narrower than the spin-orbit coupling length can support more than a single zero-energy mode at each end.
   M. Diez, J. P. Dahlhaus, M. Wimmer, and C. W. J. Beenakker, Phys. Rev. B **86**, 094501 (2012)

9. Piano improvisation is like the day-to-day decision making process of a manager – more intuitive than rational, built on experience.

Jan Patrick Dahlhaus
Leiden, November 21, 2012